2012-01-01

Hafnia-Based Nanostructured Thermal Barrier Coatings For Next Generation Gas Turbine Technology

Mohammed Noor-A-Alam
University of Texas at El Paso, nooraalam11@gmail.com

HAFNIA-BASED NANOSTRUCTURED THERMAL BARRIER COATINGS FOR NEXT GENERATION GAS TURBINE TECHNOLOGY

MOHAMMED NOOR-A-ALAM

Energy Science and Engineering Track

Environmental Science and Engineering PhD Program

Department of Mechanical Engineering

APPROVED:

Chintalapalle Ramana, Ph.D., Chair

Ahsan R. Choudhuri, Ph.D., Co-Chair

Norman Love Jr., Ph.D.

Jose Espiritu Nolasco, Ph.D.

Benjamin C. Flores, Ph.D.
Dean of the Graduate School

Dedication

To My Daughter, Averi Noor

HAFNIA-BASED NANOSTRUCTURED THERMAL BARRIER COATINGS FOR NEXT GENERATION GAS TURBINE TECHNOLGY

by

MOHAMMED NOOR-A-ALAM, M.Sc. Engg.

DISSERTATION

Presented to the Faculty of the Graduate School of

The University of Texas at El Paso

in Partial Fulfillment

of the Requirements

for the Degree of

DOCTOR OF PHILOSOPHY

Energy Science and Engineering Track

Environmental Science and Engineering PhD Program

Department of Mechanical Engineering

THE UNIVERSITY OF TEXAS AT EL PASO

December 2012

Acknowledgements

I would like show my deepest gratitude to my academic advisors Dr. C. V. Ramana and Dr. A. R. Choudhuri for providing me the opportunity to work in this project. I would like to acknowledge Dr. Norman Love Jr and Dr. Jose Espiritu Nolasco for being members in my dissertation committee. I would also like to acknowledge U.S. Department of Energy for providing the funding for this research.

Abstract

Extensive efforts have been directed in the last several decades towards improving thermodynamic efficiency of industrial gas turbines for power generation plants. The central theme of the efforts is to increase the turbine operating temperature and, thus, allowing higher efficiency. Thermal barrier coatings (TBC) constitute an advanced technology to protect the metallic surface from high temperature exposure for long time operation. The TBCs protect the gas turbine components from high temperature and allows further increase in engine operating temperature which subsequently increases the efficiency of the gas turbine power plant. However, the current TBC materials are capable of allowing the surface temperature tolerance to ~1200 ^{0}C. The present work was performed to investigate the novel hafnia based TBCs to ensure the higher surface temperature tolerance for long time operation in advanced gas turbine technology. Attention has been paid towards developing a fundamental, deeper understanding of the growth behavior, microstructure, surface-interface structure and stability, thermo-chemical and thermo-mechanical properties and durability of hafnia based TBCs. Yttria stabilized hafnia (YSH) and materials engineered from variable contents of hafnia (HfO_2) and zirconia (ZrO_2) stabilized by yttria (YSHZ) were investigated. The YSH and YSHZ coatings were produced by sputter-deposition onto various substrates. The deposition was made by varying the growth temperature from room-temperature (RT) to 500 ^{0}C. The crystal structure, surface morphology, thermal stability, thermal conductivity and mechanical properties of the grown coatings were evaluated as a function of the coatings' composition and growth temperature. The crystal structure analysis performed by X-ray diffraction (XRD) indicates the stabilization of hafnia-cubic phase in all the coatings. The morphology of the coatings is characterized by the columnar growth coupled with a dense structure as revealed by the scanning electron microscopy (SEM).

Thermal stability evaluation performed using high temperature XRD coupled with SEM indicates the stability of these coatings to 1300 ^{0}C. Thermal measurements using photo-acoustic technique and time-domain thermo-reflectance (TDTR) method indicate an effective reduction in thermal conductivity of YSH coatings compared to pure hafnia and yttria stabilized zirconia (YSZ). Mechanical properties studied using XRD indicate a very high level of compressive residual stress within the coating. The durability test using a laboratory scale combustor rig demonstrates enhanced stability of the coating in real hot gas environment. YSH coatings were also grown by electron beam physical vapor deposition and tested to compare with coatings grown by magnetron sputtering.

Table of Contents

Acknowledgements v
Abstract vi
Table of Contents viii
List of Tables xi
List of Figures xii

Chapter 1: Introduction 1
1.1 Introduction 1
1.2 Components of TBCs 4
1.3 Characteristics of successful TBCs 5

Chapter 2: Literature Review 7
2.1 Current TBC material 7
2.2 Hafnia based TBC 8
2.3 Low thermal conductivity 8
2.4 Nanostructured TBCs 10
2.5 Evolution of TBCs 11

Chapter 3: Motivation and Research Objectives 18
3.1 Motivation and background 18
3.2 Objectives 20

Chapter 4: Experimental Methodology 22
4.1 Materials 22
4.2 Fabrication methods 22
4.2.1 Magnetron sputtering 22
4.2.2 Electron beam physical vapor deposition (EB-PVD) 25
4.3 Target preparation 28
4.4 Coatings' deposition procedure 30
4.5 Deposition of bond coat 33
4.6 Characterization 34
4.6.1 Thicknes 35
4.6.2 Crystal structure and phase analysis - X-ray diffraction (XRD) 35

4.6.3 Surface morphology and interface analysis 37
4.6.4 The composition and chemical state 38
4.7.5 Thermal conductivity 38
4.6.6: Mechanical properties 42
4.6.7: Durability test 46
4.6.8: Furnace heating and thermal cycling 47
4.6.9 Thermal oxidation: 49

Chapter 5: Result and Discussion 50
5.1 Crystallography 50
5.2 Lattice parameter 55
5.3 Surface morphology 58
5.4 Grain size 63
5.5 Composition 64
5.6 Thermal conductivity 67
5.7 Thermal and chemical stability 72
5.8 Mechanical properties 75
5.9 Residual stress 79
5.10 Hot gas exposure 81
5.11Thermal oxidation 85
5.12 Interface of bond coat and topcoat 87
5.13 Crystallography of coatings grown by EBPVD 89
5.14 Morphology of coatings grown by EBPVD 90

Chapter 6: Summary and Conclusions 94

References 95

Vita 102

List of Tables

Table 4.1: Composition of the target materials..... 29

Table 4.2: Operating conditions for TBC deposition using EBPVD..... 32

Table 5.1: Details of hot gas exposure experiments……..82

List of Figures

Figure 1.1: Constituent layers of TBC on a turbine blade 5

Figure 2.1: Comparison between TBCs with high thermal conductivity and low thermal conductivity..... 9

Figure 4.1: Schematic of sputtering deposition 24

Figure 4.2: Schematic of EB deposition. 25

Figure 4.3: Schematic diagram showing (a) straight, (b) 90° electromagnetic deflected electron beam, and (c) EB-PVD chamber showing six EB gunsand three continuous ingot (A-C) feeding system 27

Figure 4.4: YSH Target..... 28

Figure 4.5: Sequential steps for the fabrication of YSHZ targets..... 30

Figure 4.6: Magnetron sputtering setup 31

Figure 4.7: The EBPVD setup for coating deposition 33

Figure 4.8: Bond coated substrates and the topcoat grown by EBPVD on the bond coat..... 34

Figure 4.9: Bruker D8 Advance X-ray diffractometer..... 35

Figure 4.10: Hitachi S-4800 Scanning Electron Microscope with EDS system..... 37

Figure 4.11: Schematic diagram of the photo-acoustic apparatus 39

Figure 4.12: Schematic diagram of three consecutive layers: Si substrate, YSH film, and reflecting Al over layer for the thermal conductivity measurements. 40

Figure 4.13: Schematic illustration of load-displacement data..... 43

Figure 4.14: The plot showing the relation between inter-planner spacing and $\sin^2\psi$ 45

Figure 4.15: The experimental setup for the hot gas exposure test. (a) sample holder (b) the combustor rig and (c) the sample exposed to the hot gas 47

Figure 4.16: High temperature CM furnace..... 48

Figure 5.1: The XRD patterns of YSH coatings on SS-403 grown at various substrate temperatures..... 51

Figure 5.2: The XRD patterns of YSH coatings on Inconel-738 grown at various substrate temperatures..... 52

Figure 5.3: The effect of substrates on the crystal structure of YSH coatings grown at same substrate temperature, 500 ^{0}C. 53

Figure 5.4: XRD curves of YSHZ coatings on alumina substrates. The observed peaks can be indexed to cubic hafnia as indicated 54

Figure 5.5: XRD curves of YSHZ coatings on SS-403 substrates. The observed peaks can be indexed to cubic hafnia as indicated 55

Figure 5.6: The variation of lattice parameter with Ts 57

Figure 5.7: The variation of lattice parameter with amount of ZrO_2 in YSHZ coatings 57

Figure 5.8: SEM images of YSH coatings on Inconel-738 (figure 5.8a) and SS-403 (figure 5.8b) substrates. A slight increase in grain size and densification with increasing growth temperature can be noted 59

Figure 5.9: Surface morphology of YSH coatings grown on SS-403 and Inconel-738 with bond coat..... 60

Figure 5.10: Surface morphology of YSHZ coatings grown at 500 °C on SS-403..... 61

Figure 5.11: Surface morphology of YSHZ coatings grown at 27 °C on SS-403 62

Figure 5.12: Surface morphology of YSHZ coatings when grown as thick coatings (~3µm) at

500 °C 62

Figure 5.13: Typical columnar growth of YSHZ coatings 63

Figure 5.14: The variation of average grain size of YSH coatings with growth temperature 64

Figure 15: EDS spectrum of YSH coatings grown at 500 ^{0}C. The X-ray peaks due to Y, Hf and O atoms and their respective positions are as indicated for the EDS curve 65

Figure 5.16: EDS spectrum of representative YSHZ coatings grown at 500 ^{0}C 65

Figure 5.17: XPS data showing the atomic concentration as a function of sputtering time 66

Figure 5.18: Elemental mapping of a representative YSHZ coating showing the uniform distribution of the four elements consisting the YSHZ coating..... 67

Figure 5.19: Phase shift with respect to modulation frequency for YSH grown at RT (a), 300 ^{0}C (b) and 500 ^{0}C (c) 70

Figure 5.20: Variation of thermal conductivity of YSH coatings with growth temperature 71

Figure 5.21: Thermal conductivity of YSHZ coatings as function of composition 72

Figure 5.22: High-temperature XRD curves of YSH coatings showing the phase stability at 1300 ^{0}C..... 73

Figure 5.23: High-temperature XRD curves of representative YSHZ (HfO_2 : ZrO_2 = 4:1) coatings showing the phase stability at 1300 ^{0}C..... 73

Figure 5.24: EDS curves of YSH coatings before and after thermal treatment at 1300 ^{0}C..... 74

Figure 5.25: EDS curves of representative YSHZ coatings before and after thermal treatment at 1300 ^{0}C……..74

Figure 2.26: Mechanical properties of YSH and YSHZ coatings measured using nano-indentation ……75

Figure 5.27: Stress versus displacement plot for nano-indentation on YSH coating 77

Figure 5.28: Optical images of YSH and YSHZ coatings after nano-indentation ……78

Figure 5.29 Mechanical properties of YSH coatings before and after exposure to 1300 ^{0}C ……78

Figure 5.30: d-spacing as a function of $Sin^2\psi$ for YSH sample grown on Inconel-738……80

Figure 5.31: Residual stresses calculated for YSH and YSHZ coatings……...81

Figure 5.32: XRD patterns of YSH coating before and after exposure to hot gases ……83

Figure 5.33: SEM images of YSH sample after exposure to hot gases…….84

Figure 5.34: Residual stress in YSH coatings before and after exposure to hot gases……..85

Figure 5.35: The weight increase against the exposure time a) weight increase per unit area against exposure time and b) total weight increase against exposure time……87

Figure 5.36: Cross-sectional images of YSH coatings on bond coat (NiCoCrAlY) obtained by SEM……...88

Figure 5.37: Cross-sectional images of YSH coating on alumina substrate obtained by TEM ……89

Figure 5.38: XRD pattern of YSH and YSHZ coatings grown by EBPVD system …….90

Figure 5.39: Surface morphology of YSH coatings grown by EBPVD……91

Figure 5.40: Surface morphology of YSHZ-1 and YSHZ-4 coatings grown by EBPVD……92

Figure 5.41: Surface morphology of YSH coatings grown by EBPVD after annealing at 900 ^{0}C for 15 hrs……93

Figure 5.42: Cross-sectional SEM images of YSHZ samples grown on Si substrate by EB deposition……...94

Chapter 1: Introduction

1.1 Introduction

Extensive efforts have been directed in the last several decades towards improving the thermodynamic efficiency of the industrial gas turbines for power generation systems. Increasing the operating temperature, which is specifically characterized by the inlet gas temperature, has been the primary driving factor to further improving the efficiency. A significant improvement in power and fuel economy can be achieved by a 100 ^{0}C increase in inlet gas temperature. (1) For instance, an increase by 55 ^{0}C in inlet temperature increases the simple cycle efficiency up to 4% and provides 8-13% additional power output. (2) Similarly, an increase by 110 ^{0}C in temperature was expected to increase the thrust from 40,000 lb to over 50,000 lb in jumbo-jet gas turbines. (3) The increase in inlet temperature must be accomplished without any structural failure due to oxidation, thermal fatigue, creep, melting, phase change or any other mechanical damage. This demands maintaining the surface temperature at low enough to preserve the material properties at endurable level. (1) Although the cooling system using compressed air might be an option the loss of thrust and additional fuel cost for cooling scheme don't consent it to be technologically realistic. (1)

Two different approaches have been deliberated to meet the objective of increasing temperature without compromising the machine performance. Designing new super alloys is the first while introducing new materials for thermal barrier coating (TBC) application in turbines is the later. Various super alloys have been developed over the time and were tried for one

generation to the next generation turbine systems. Each generation of super alloys was able to increase the operating temperature by 80-85 ^{0}C from the previous one. (1; 2; 4) However, analysis indicates that this improvement is expensive and not economical. On the other hand, the first generation of TBCs was capable of conserving a thermal insulation of 165 to 170 ^{0}C. (1; 4) It has been reported that 100 -150 ^{0}C insulation provided by TBC is comparable to that attainable by three consecutive generations of super alloys. (1) Some TBCs were expected to improve the service life of first stage blades to the 3X times more of its original life span (without TBCs). (5) Thermal barrier coatings (TBCs) are, therefore, being utilized as an advanced technology to protect the metallic surface from high temperature exposure for extended duration.

Thermal barrier coating is usually made of ceramic material and applied as a very thin layer over the metallic surface which helps the structural material/system sustain extremely high temperature for prolonged time and, thus, allows very high operating temperature. (1; 2; 4; 6) TBCs are extensively used in gas turbines and aero-engine parts. As TBCs protect the gas turbine components from high temperature exposure, this allows further increase in engine temperature which subsequently increases the efficiency of the gas turbine power plant.

The present work is focused towards designing and development of novel TBCs with high temperature tolerance. The objective is to elevate the temperature as high as possible to maximize the efficiency since the efficiency of the gas turbine predominantly depends on the operating temperature. (1) The development of novel TBCs which can withstand higher temperatures than the current standard can minimize the fuel consumption by maximizing the gas turbine efficiency, which will subsequently help protect the environment through the

reduction of carbon emission. (2) Additionally, different fuel compositions ranging from natural gas to broad range of syngas with high hydrogen contents are being tried for next-generation gas turbine power plants. (2) Therefore, the TBCs for next-generation gas turbine system should have the reliability and durability in diverse chemical, thermal and mechanical environment.

The TBC production in the industry is made by one of the two most popular methods namely air plasma-spraying (APS) and electron beam-physical vapor deposition (EBPVD). (1; 5; 6) Both the quality and functional performance of TBCs in real turbine systems are very sensitive to the method of fabrication and conditions employed for coatings' fabrication. TBCs fabrication by APS lowers processing costs and provides better heat insulating quality to the coating depending on the material used for the coating. On the other hand, EBPVD provides better spallation resistance, less air cooling hole blockage and smoother surface. (4) A typical splattered structure with molten or semi molten droplets is produced when the coating is grown by APS whereas, coating grows in a well-defined columnar structure by the EBPVD deposition. The pores, cracks and inter-splat boundaries offer the APS coating a significantly lower thermal conductivity. (7) Although the EBPVD coatings provide slightly higher thermal conductivity compared to APS coatings, the individual columns impart high strain tolerance and protect the coating from the development of high tensile stresses (8) The failure mechanism of APS coatings is attributed to the formation and connecting up of the cracks just above the interfaces between bond coat and TBC due to the oxidative thermal cycling. On the other hand, EBPVD coatings fail through the development of cracks within the thermally grown oxide layer when a critical thickness-stress combination ascends. (7)

The work presented in this thesis was directed towards investigating the novel hafnia based nanostructured TBCs to ensure the minimum 1300 ^{0}C surface temperature tolerance for long time operation. The research was focused on fabrication and deeper understanding of the growth behavior, microstructure, surface and interface stability, thermo-chemical and thermo-mechanical properties and durability of hafnia based TBCs. Yttria stabilized hafnia (YSH) and materials engineered from variable contents of hafnia (HfO_2) and zirconia(ZrO_2) stabilized by yttria (YSHZ) were investigated. The goal of the research work was to find out alternate, ideal TBCs in order to meet the unique structural, thermo-chemical and thermo-mechanical performance required by advanced gas turbine engines. The relevant background information and fundamentals TBCs are briefly discussed below.

1.2 Components of TBCs

Thermal barrier coatings basically consist of three constituent layers on top of the substrate material. The multilayer stack of TBCs on a turbine blade is schematically presented in Figure 1.1. The bottom and top layers are the bond coat and top coat, respectively. (1; 6) The thermally grown oxide called TGO (usually Al_2O_3) comprises the middle layer in between these two layers. (6) The function of bond coat is to make bonding between the substrates and top coat. (1; 6) The bond coat consists of several elements some of which produce refractory thermally grown oxide (TGO). These oxides are grown when the coating is exposed to high temperature operation. The most vulnerable part of these three layer TBC system is the thermally grown oxide which initiate the failure of TBCs, however, it protects the oxygen diffusion to the substrate. (6) The top layer is the ceramic coating which is exposed to the high temperature

environment and responsible to the functionality of thermal barrier or thermal protection layer. (1; 2; 6; 9) The TBC system consisting of these typical bond coat and top coat is commonly referred to “duplex TBCs”. (10)

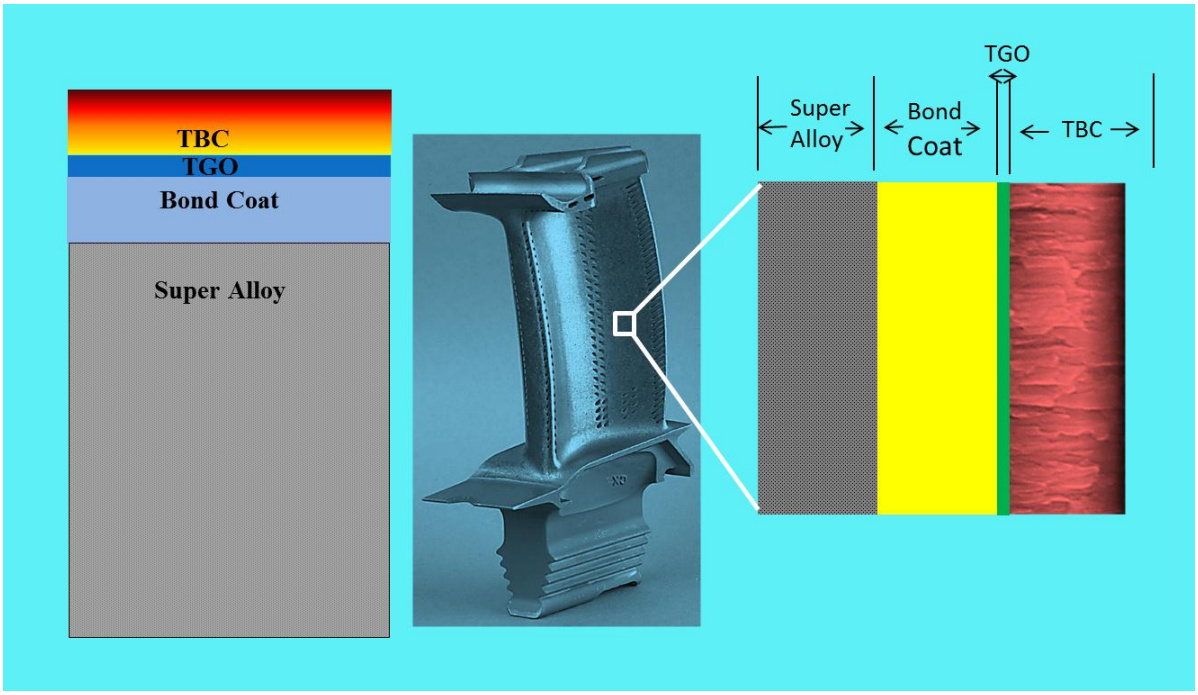

Figure.1.1: Constituent layers of TBC on a turbine blade.

1.3 Characteristics of Successful TBCs

The successful TBCs are expected to possess the following desired properties: (6)

- Ability to withstand the thermal expansion stresses associated with heating and cooling
- Large strain without failure which is conferred by large amount of porosity in microstructure
- The material must not undergo phase transformations on cycling between room temperature and higher temperatures

- Ability to withstand repeated thermal cycling
- Ability to withstand prolonged high temperatures in an oxidizing atmosphere.
- Material has to be thermodynamically compatible with the oxides formed by oxidation of the bond-coat

Chapter 2: Literature Review

2.1 Current TBC Material

Yttria stabilized zirconia (YSZ) is the current material of choice for high temperature TBC applications. Widespread efforts have been directed towards the development of appropriate TBCs materials for gas turbine systems. (6; 9; 11-21) So far the most successful and industrial choice of TBC material is 6-8 wt.% yttria stabilized zirconia (YSZ). (9; 11) Zirconia is one of the few refractory oxides that can be deposited as thick film or coating using the well-known plasma spraying technique. (11) YSZ is used in its metastable tetragonal structure. (9;11-12) Yttria has been considered as the suitable stabilizer because yttria incorporation in optimum composition imparts lower thermal conductivity, which is independent of temperature within the range of turbine operating temperature. (11; 13; 22) The lower thermal conductivity of YSZ is mainly due to the presence of small spacing between point defects. (11) The high concentration of point defects is generated by the substitution of Zr^{+4} ions by Y^{+3} ions in the fluorite structure. (11) One oxygen vacancy is created by the replacement of one Zr^{+4} ion by two Y^{+3} ions. The large concentration of defects changes the vibration modes from pure phonons in undoped, monoclinic zirconia when zirconia is doped with yttria. (11) The change of vibration mode to a variety of other modes leading to lower thermal conductivity occurs without changing crystal structure. (11) This is the fundamental reason for YSZ being established as the current TBC standard in gas turbine industry.

2.2 Hafnia Based TBCs

It is clear from above brief review and analysis that the current choice of material for TBC applications is YSZ. However, the maximum temperature tolerance of YSZ is up to 1200 ^{0}C for long time operation. (11) YSZ undergoes phase transformation at temperature higher than 1200 ^{0}C. This phase transformation is associated with the volume change leading to the initiation of cracks on the surface and interface between TBC and substrate. (11) The ultimate result is the failure of the TBC system. Thus the application of YSZ is limited to the temperature 1200 ^{0}C. (14; 15) Therefore, design and development of new and better TBCs is desired for emerging and future advanced gas turbine technology. Manufacturing new materials or engineering the coatings with novel chemistries must be taken into account to develop TBCs with unique structural, thermal, thermo-chemical, and mechanical properties. Motivated by these research needs in the topical areas of TBCs for turbine applications in power generation systems, the current research has been focused to explore better TBCs with temperature tolerance higher than 1200 ^{0}C in order to increase the efficiency of gas turbine systems. The novel hafnia based TBCs considered in this research have the potential to meet the requirement to be used in next generation gas turbine materials. This statement is mainly based on three important characteristics of hafnia: i) suitable crystal structure and phase transformation behavior ii) higher melting point (2900 ^{0}C) and iii) lower thermal conductivity (1.5 W/m.K). (9; 11; 15)

2.3 Thermal Conductivity

Thermal conductivity of TBC materials is an important characteristic, which plays a key

role in deciding the functional performance of the material for thermal protection. Because of the low thermal conductivity, same amount of temperature drop in turbine blades can be attained with the lower thickness of the TBC material compared to the traditional TBC of comparatively higher thermal conductivity. As shown in Figure 2.1, lower thermal conductivity helps reduce the thickness of the thermal barrier coating for the same cold terminal temperature T_{back}. Subsequently, lower thickness reduces the total mass added to the turbine blades. Since the turbine blades are rotating components, lower mass is always favorable in consideration of energy consumption. On the other hand, lower thermal conductivity allows increasing operating temperature maintaining the same substrate back temperature which consequently increases the overall thermodynamic efficiency. (23) In addition, higher thickness triggers the delamination of TBC as turbine blades experience very high centrifugal forces.

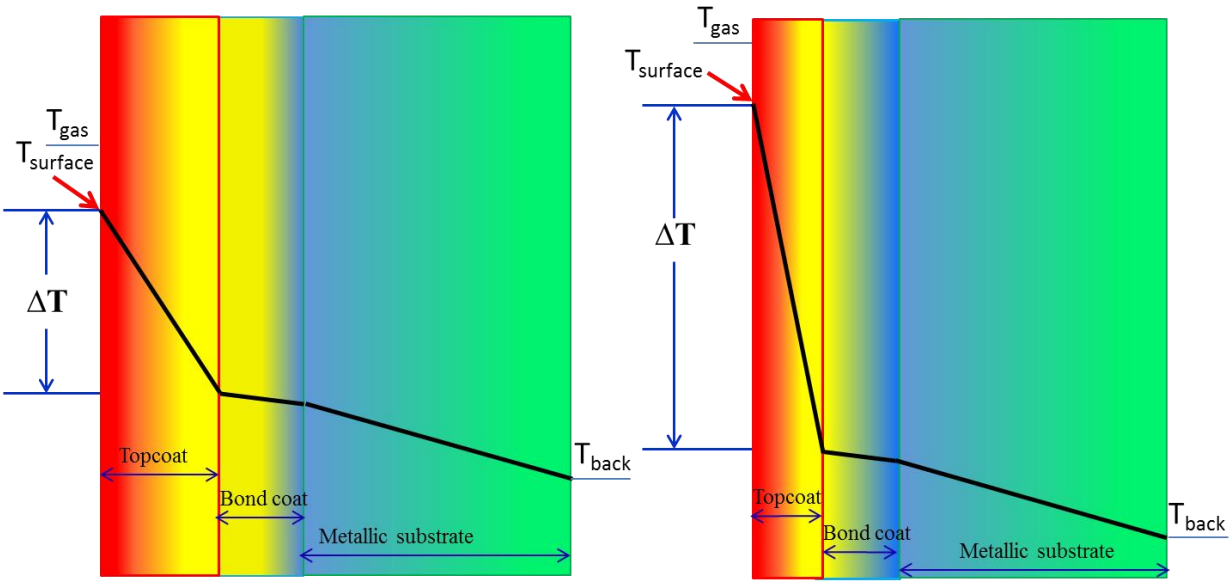

Figure 2.1: Comparison between TBCs with high thermal conductivity and low thermal conductivity (23)

2.4 Nanostructured TBCs

Nanostructured materials for TBC application have been receiving a great attention due to their improved performance compared to the conventional material of same composition. (19-20; 24-26) Because of the large volume fraction of internal interfaces, many important properties of nanostructured materials were found to be different from their conventional counterpart. (24) The most important physical and mechanical properties such as mechanical strength, indentation crack resistance, adhesion strength, spallation resistance, abrasive wear resistance and sliding wear resistance were found to be superior in nanostructured Al_2O_3-TiO_2 compared to the conventional bulk of the same material. (19-20; 24-26) It has been demonstrated that nanostructured partially stabilized zirconia coating exhibits higher bond strength. (21; 25; 27-30). Amorphous materials are expected to have significantly lower thermal conductivity at room temperature than similar crystalline materials; however, the difference is not significant at temperatures more than the Debye temperature. (11) Furthermore, glassy materials tend to crystallize after certain duration of service. (11) As the nanocrystalline materials exhibit grain boundary scattering as an extrinsic phonon-scattering phenomenon, they are expected to lower the thermal conductivity. Still it needs intrinsic evidence of these performances at elevated temperatures. A study of nano-crystalline stabilized zirconia ceramics by Raghavan et al. reported that there was no significant effect of grain size on thermal conductivity. (16) However, Soyez et al. reported that there was some extent of grain size effect on thermal conductivity for the grains of size below 30 nm. (16; 31) However, the effect of nanocrystalline structure on thermal conductivity is less than that of Y content and oxygen vacancies in YSZ. The problem with the nanocrystalline material is that the material starts to coarsen at long time operation. (11)

Therefore, nanoporous materials that can resist coarsening of the porosity are of great interest for TBC materials. Nanostructured hafnia based TBCs are also associated with the reduction in weight of the TBCs which is a crucial factor for designing gas turbine rotating components.

2.5 Evolution of TBCs

Thermal barrier coating materials were considered for research for many years. Efforts were focused towards the development and manufacture of TBCs. The earlier research on TBC materials have resulted in improving the quality of TBCs gradually. However, the appropriate TBC materials for next generation gas turbines power systems are yet to be designed. Most of these previous works were focused on the TBCs made of zirconia. (6; 11-12; 18-21; 23; 28-30) Three important characteristics, that made ZrO_2-based TBCs as the most successful TBCs are: i) one of the few refractory oxides, ii) can be deposited as thick coatings using well known plasma spray and EBPVD methods, and iii) low thermal conductivity and high mechanical stability. The current state of art TBCs is based on 7-8 wt% Y_2O_3 stabilized zirconia. (6; 9; 11-12; 18-21; 23; 28-30) Yttria is selected as stabilizer because of its great influence on thermal conductivity up to a certain concentration (11). Investigation on the effect of chemical structure on thermal conductivity revealed that high point defect is associated when Zr^{+4} is replaced by Y^{+3} in a fluorite structure (11). This provides some small spacing between the point defects resulting low and temperature independent thermal conductivity of YSZ. It has been reported that the replacement of every Zr^{+4} ion by two Y^{+3} ions results one oxygen vacancy and the average distance between oxygen vacancies is ~1 nm and between Y^{+3} ions is ~0.5 nm (11). At temperature above 1200 ^{0}C, ZrO_2 undergoes phase transformation from the t‘-tetragonal to

tetragonal and cubic (t + c) and then to monoclinic (m) structure. (9; 11; 14) This phase transformation is associated with a volume change which creates cracks and spallation within the coatings. The ultimate result is the delamination of the coating. (12; 14) This failure of YSZ demands the development of new TBCs that can withstand more than 1200 ^{0}C so that the turbine can operate at higher temperature resulting higher efficiency.

Various types of materials are currently under consideration by research community to improve the performance of TBCs. These materials are basically ceramic oxides and can be categorized as oxides with (i) fluorite structure, (ii) pyrochlore structure oxides, and (iii) others. (11; 24; 32-35) Fluorite-structured materials got the vast attention, candidate materials include HfO_2, CeO_2, and ThO_2. (11) Doped CeO_2 exhibits comparable thermal conductivity but it is not a practical choice as CeO_2 shows high volatility. (11) Reduction in thermal conductivity was reported when Zr^{+4} ions were replaced by Hf^{+4} ions. (11; 36) YSZ was co-doped with a mixture of one trivalent ion larger than Y^{+3} and another trivalent ion smaller than Y^{+3}. (11; 15) This co-doping was able to preserve the metastable zirconia structure and this new composition showed more improvement in performance. (11) Since these works were focused on porous material, the effect of porosity on thermal conductivity needs deeper understanding. Most importantly, the co-system of hafnia and zirconia must be considered for detailed investigation to be considered for advanced turbines.

Thermal conductivity, which is an important characteristic that decide the functional performance of TBCs, has been the subject of numerous investigations. Various available materials for thermal applications were explored by carefully considering thermal conductivity

values. Thermal conductivity ranging from ~1.1 W/mK to ~1.7 W/mK at temperatures between 700 ^{0}C and 1200 ^{0}C was reported for zirconates of Gd, Eu, Sm, Nd, and La. (33; 37-39) Other complex oxides, $Y_3Al_xFe_{5-x}O_{12}$, $LaPO_4$ and $LaMgAl_{11}O_{19}$, were also considered for TBCs but none of them showed performances as good as YSZ. (11; 37)

Zirconates with pyrochlore ($A_2^{+3}B_2^{+4}O_7$) structure were also considered viable candidates because of their lower thermal conductivity than YSZ. Many pyrochlores are also refractory and thermally stable well above 1500 ^{0}C. (11) Pyrochlore structure is similar to that of fluorite structure. The pyrochlore unit cell can be considered to consist of eight fluorite unit cells with, on average, one oxygen vacancy in each fluorite unit cell. However, the pyrochlore is unstable and forms disordered fluorite material $(ZrO_2)_2$-Y_2O_3. The stable pyrochlore structure can be obtained by replacing Y^{+3} ion with larger ions such as La^{3+} or Gd^{+3} or smaller ion such as Ti^{+4} or Mo^{+4} which can sustain up to at least 1500 ^{0}C. (11). Zirconates of Gd, Eu, Sm, Nd, and La showed the thermal conductivity ranging from ~1.1 W/mK to ~1.7 W/mK at temperatures between 700 ^{0}C and 1200 ^{0}C (11). It was evident that the zirconates have the lowest thermal conductivity among stable pyrochlores. In spite of lower thermal conductivity, the plumbate pyrochlores are not viable candidates because of their instability due to decomposition and environmental incompatibility (11). Co-doping of pyrochlores has been expected to further reduce conductivity and thermal expansion coefficients. Some success in reducing thermal conductivity was achieved by 30% doping of Nd, Eu, or Gd with $La_2Zr_2O_7$. (11) Gd doping reduced the thermal conductivity from ~1.55 W/mK to ~0.9 W/mK. (11) However, wide range of $(ZrO2)_2$-Gd_2O_3 compositions did not show significant variation in thermal conductivity, especially at high temperature. (11)

Other type of oxide ceramics oxides were also proposed to effectively lower thermal conductivity. These materials include garnets ($Y_3Al_xFe_{5-x}O_{12}$), monazite ($LaPO_4$) and magnetoplumbite lanthanum hexaaluminate ($LaMgAl_{11}O_{19}$). The perovskites, ABO_3, are the group of crystal structures that are stable to very high temperatures and can accommodate a wide variety of different ions in solid solution, including ions with large atomic mass. (11) However, none of these shows lower conductivity than the pyrochlore zirconates. (11)

A large mismatch in thermal expansion coefficient between the metallic substrate and the coating reduces the bonding strength (24). On the other hand, it is always desirable to have a low thermal expansion coefficient of the hot coating surface in order to reduce the thermal stress and sensitivity to thermal shock. (24) The possible solution of these opposing phenomena is to use a multilayer system (24). In this type of system, the traditional zirconia is combined with another low cost refractory material. A traditional example of these types of oxide systems is $Al_2O_3.SiO_2.MgO$. For instance, cordierite ($2MgO{\cdot}2Al_2O_3{\cdot}5SiO_2$) has a very low CTE ($1.67x10^{-6}$ K^{-1} (40) but the cordierite composition forms amorphous structure after plasma spraying. Two phase transformation occurs by subsequent heating at 830 ^{0}C and 1000 ^{0}C (24). The volume change associated with the phase change leads to cracking. 6 wt% TiO_2 is used in order to solve this problem through depositing the crystalline cordierite (24). Another problem associated is that yttria diffuses into the cordierite which leads to the destabilization of zirconia with a subsequent phase transformation from tetragonal to monoclinic phase. (24) Forsterite ($2MgO{\cdot}SiO_2$) shows a high coefficient of thermal expansion $11x10^{-6}$ K^{-1} (40) which demonstrates a good match with the substrate. It also exhibits very good resistance to thermal shock with a thickness of several hundred microns. The crystallinity of forsterite after spraying is

also higher than other oxides which can avoid the volume change associated with the transformation from amorphous to crystalline phase.

Hafnia based materials are technologically imperative for many applications, specifically in nuclear industry. However, the history of hafnia based thermal barrier coating is not very long. The limitation of zirconia based TBCs for operating at higher temperature opens the door for investigating the TBCs which can withstand at higher temperature. This is the motivation for our research on hafnia based TBC for high temperature applications. (41) The crystal chemistry of hafnia is very similar to zirconia. Having the similar crystal structure to zirconia, hafnia exhibits the phase transformation at the temperature 700 ^{0}C higher (1700 ^{0}C) than that of zirconia. (41). This superior property acclaims the applicability of hafnia at very high temperature as a high temperature transformation toughened ceramic. However, the mechanical properties including the fracture toughness of hafnia based TBCs depend on the processing techniques and processing conditions. In addition to temperature and thermal conductivity, the fracture toughness of hafnia is lower than the counterpart zirconia which suggests further investigation and development of hafnia based TBCs for utilization in turbine technology. (41)

The origin of the failure in most of the duplex TBC systems lies in the mismatch in thermal expansion of ceramic top coat and metallic bond coat. In order to solve this problem the concept of functionally gradient material (FGM) was introduced in TBC system. (42) The FGM TBC system consists of multi-layered coatings which is sprayed one layer over another. The composition of the layers varies in the direction of increasing thickness. The composition ranges from 100% metal deposited proximately on the substrate to 100% ceramic topcoat. Although

several techniques have been tried to fabricate the FGM TBC system, maintaining the desired composition in the thickness direction is not very easy. Plasma spraying, powder metallurgy and in situ synthesis are common techniques that were explored to fabricate FGM TBC system. Kim et al applied the detonation gun (d-gun) spray technique to produce FGM TBC. (42) It was reported that because of the higher kinetic energy of the powder particles, d-gun spraying produce the coatings which are higher in adhesive and cohesive strength compared to traditional thermal sprayed TBCs. (42) These authors also proposed a new approach called 'shot control method' to fabricate superior FGM TBCs. It has been reported that the shot control method was able to produce the FGM TBC with desired compositional gradient of metals and ceramics in the desired thickness direction. They reported that the ceramic and the metals mixed in the FGM system were able to maintain their individual properties without significant suffering from severe oxidation and phase transformation. Because of the mixed composition this type of TBC system was able to withstand more severe thermal shock compare to their traditional counter part of thermal spray coatings. (42)

Because of the thorough similarity to zirconia both in structure and chemistry hafnia is being considered as the most promising replacement of the zirconia based TBCs. (41) The use of hafnia and zirconia together as a mixed composition is also another option. The mixing of hafnia and zirconia is so uniform that it is hard to identify their individual existence using conventional x-ray diffraction. Continuous solution of hafnia and zirconia was confirmed and reported in literature with well description of the binary system. (43) Sakka et al. reported that the self and inter-diffusion coefficient values of hafnia and zirconia are also similar. (44) The similar electronic configuration ($4f^{14}5d^{2}6s^{2}$ for hafnium and $4d^{2}5s^{2}$ for zirconium), atomic radii

(0.1442nm for Hf and 0.1454nm for Zr), ionic radii (0.084nm for Hf^{+4} and 0.083nm for Zr^{+4}) and similar electronegativity values (1.23 for Hf and 1.22 for Zr) are the origin of the uniform mixed composition of hafnia and zirconia systems (41). This uniformity is the reason of investigating the mixed composition of hafnia and zirconia system as the TBC top coat.

The development of hafnia-based TBC was initiated in order to achieve the higher temperature tolerance and the chemical stability at temperatures higher than the current state of art TBCs. The most promising composition of hafnia based TBC was found as 7.5 mass% Y_2O_3–HfO_2 (7.5YSH) grown by EB-PVD technique. (9)

Therefore, the design and development of new and better TBCs system is required for advanced gas turbine technology. Discovery and engineering of new materials with novel chemistries must be taken into investigation for optimum structural, thermo-chemical and thermo-mechanical properties. In this circumstance, the proposed work is intended to design and engineer new TBC materials that ensure the reliable surface temperature of at least 1300 ^{0}C. This work investigated the nanostructured HfO_2-based coatings, namely, Y_2O_3-stabilized HfO_2 (YSH) and Y_2O_3-stabilized ZrO_2-HfO_2 (YSHZ), for next generation TBC applications.

.

Chapter 3: Motivation and Research Objectives

3.1 Motivation and Background

Climate change is one of the burning issues for last several years. The increase of global temperature shows a strong correlation with the CO_2 concentration in atmosphere as was reported by many researchers. (45) According to the data compiled by the National Oceanic and Atmospheric Administration (NOAA), global surface temperature is raised by 1.3 ^{0}F over the last 100 years. (46) The rate of warming over the last 50 years (0.24 ^{0}F per decade) is almost double the rate of warming over the last 100 years (0.13 ^{0}F per decade). If the temperature increases at the current rate, global temperatures will increase by 3 – 7 ^{0}F by 2100 which will impose adverse effect on our ecosystems and economies. (45-46)

It is our responsibility to save our planet and make is safer place for the future generations. Unfortunately, no other option is available to save our globe without reducing the carbon emission and, thus, making it green. With such motivation, some countries across the globe have recently signed mitigation pledges in the Copenhagen Summit in December 2009 and set the emission reduction goals. (47) Japan, European Union, United States, Brazil & Russia set specific emission reduction goals. (47) China and India agreed to reduce the CO_2 intensity (emission reductions per unit of output as measured by GDP). Furthermore, 30 billion dollars were promised by developed countries to help developing countries achieve their emission mitigation goals for the time frame of 2010-2012.

Most important point of concern and challenging question is that "what could be the mean to reach the goal of mitigation." Since the technology of other energy sources e.g., renewable energies are still in nascent stages and there arises some social issue like food crisis due to the production of bio-fuel technological development of using the conventional fossil fuel could be the prudent policy for greenhouse gas mitigation. If fossil fuel utilization in transportation is replaced by electricity, it will reduce a greater portion of CO_2 emission. However, this will demand a huge production of electricity which requires burning of a lot of fossil fuel like coal, oil and natural gas. In order to reduce this increased use of fossil fuel, the efficiency of power plants has to be increased to a greater extent. According to the laws of thermodynamics, increasing the temperature in the thermodynamic cycle used in power plant will increase the overall efficiency of energy conversion. This will reduce the use of fossil fuel which will subsequently mitigate climate change through reducing the emission of greenhouse gases to a significant extent. The increase of temperature in power plant is technologically feasible by burning the natural gas or syngas in proper proportion of fuel and oxidizer in combustion section. But the issue is that available materials and options that can be employed in the gas turbines to sustain at required higher temperature are very limited. The maximum temperature currently used in gas turbine is 1200 ^{0}C. This temperature can be used for safe operation when the turbine blades are coated with ceramic thermal barrier coating. The most successful thermal barrier coating so far is yttria stabilized zirconia (YSZ), which is stable up to 1200 ^{0}C at its metastable tetragonal structure. In these circumstances, near term target is to increase the temperature to $\geq$ 1300 ^{0}C for extended operation. So the discovery or engineering of the TBC materials that can be used with reliability at temperatures $\geq$ 1300 ^{0}C is the greatest

challenge to meet the challenging goal of the syngas/hydrogen turbine technology. All of these factors constitute the impetus for the research on TBCs for next generation gas turbines.

The goal of this research is to engineer coatings with unique structural, thermal, thermo-chemical, and mechanical properties for advanced gas turbine technologies. Recently, improved temperature tolerance up to 1400 ^{0}C has been reported for yttria stabilized hafnia (9). It has been shown that the HfO_2 and ZrO_2 co-system can result in significant reductions in thermal conductivity. (15) Zr^{+4} replacement with Hf^{+4} also showed a reduction of thermal conductivity. (48) But the detailed understanding of the mechanism and the relation between structure and performance are still absent. However, while these observations are promising, very little is known specifically about the HfO_2-based thermal barrier coatings. Recently, it has been shown that nanostructured coatings of Al_2O_3-TiO_2 showed superior mechanical properties, including indentation crack resistance, adhesion strength, spallation resistance, abrasive wear resistance, and sliding wear resistance. (19; 20) Nanostructured YSZ showed improved properties, such as increased bond strength, better thermal resistance, and reduced thermal conductivity compared to their coarse-grained coatings. (21; 28-30) Motivated by these facts and challenges, the present research is focused to develop and engineer the nanostructured hafnia based thermal barrier coatings for next generation gas turbines using wide variety of syn-gas compositions.

3.2 Objectives

Development of nanostructured hafnia based TBCs for the next generation gas turbine components is the main goal of this work. The yttria stabilized hafnia (YSH) and various

compositions of hafnia and zirconia namely YSHZ are main target materials to be used for deposition. The experimental effort is mainly directed to clear understanding of nanostructured YSH and YSHZ for high temperature tolerance, durability in diverse environment and reliability for using in advanced turbine technology. The specific objectives are:

Objective1: To Fabricate YSH and YSHZ

Objective 2: To Evaluate the Properties and Microstructure of Fabricated TBCs

Objective 3: To Determine the Coating Durability and Performance Evaluation

Chapter 4: Experimental Methodology

4.1 Materials

Yttria stabilized hafnia (YSH) target purchased from Plasmaterials Inc. was used to fabricate the coatings. The composition of yttria in YSH was maintained at 7.5%. Pure hafnia, zirconia and yttria powders were used to fabricate the targets with various compositions of hafnia and zirconia. The traditional MCrAlY material was used as bond coat where M represents a metal. The composition of the Ni-aluminide based alloy (NiCoCrAlY) used for the bond coat was 21.54 mass% Co, 16.91 mass% Cr, 12.4 mass% Al, 0.66 mass% Y and balance Ni. Four different materials i) Ni based super alloy, Inconel-738 (1.2 cm x 1.2 cm x 3 mm) ii) 403-stainless steel (2.5 cm diameter and 3 mm thickness) iii) alumina (2.5 cm x 2.5 cm x 2 mm) and iv) Si (2.5cm x 2.5cm x 2mm) were used as substrates.

4.2 Fabrication Methods

Magnetron Sputtering and Electron Beam Deposition based Physical Vapor Deposition (PVD) methods were employed to fabricate nanostructured TBCs.

4.2.1 Magnetron Sputtering

Sputtering is one of the Physical Vapor Deposition (PVD) processes used for depositing thin films, thick films, and coatings. (49-52) An ionized high energy gas molecule is used to

eject atoms from a specified solid target through the bombardment on the surface of the target. (49) For efficient momentum transfer, the atomic weight of the sputtering gas should be close to the atomic weight of the target material to be deposited. (49) Argon (Ar) is usually used as the sputtering gas. (49) A high voltage (about kV) is applied in high vacuum (usually about 10^{-4} Pa) in order to create high-energy plasma. (49; 53) This plasma emits a colorful halo of light known as "glow discharge" which consists of electrons and ions. (54) The material used for the coating is placed as the cathode and known as target. (49) When a high voltage is applied in vacuum free electrons are ejected from the cathode with high energy. When these high energy electrons strike the inert argon gas it knockouts another electron from argon producing Ar^+ ion. When the positively charged Ar^+ ion further interact with free moving electrons they get extra energy from high energy electrons and become neutral argon atom with extra energy. They emit photons to release the extra energy and plasma is produced. The energized plasma ions (Ar^+) move toward the cathode and strike the target composed of the coating material. The force of high kinetic energy gases causes atoms to eject from the target material and they condense on the substrate resulting strong bonding with the substrate. The schematic diagram of the sputtering process is shown in Figure 4.1. The atoms sputtered from the target material move upward toward the substrate with a distribution of energy, typically up to tens of eV. (49; 53-54)

In magnetron sputtering, a strong magnetic field is applied so that the electrons are trapped close to the surface of target cathode. Due to the strong electric and magnetic fields, the electrons follow a helical path around the magnetic lines. (49) This results in more collisions with the neutral gaseous molecules producing more ionized gases. (49) The gas density may increase up to 10^{13} ion/cm^3. (53) As a consequence, the deposition rate increases significantly.

(53) Since the sputtered atoms are neutral, they are not affected by the magnetic trap. Furthermore, since a lot of extra argon ions are produced, the plasma can sustain even at very low gas pressure. (49)

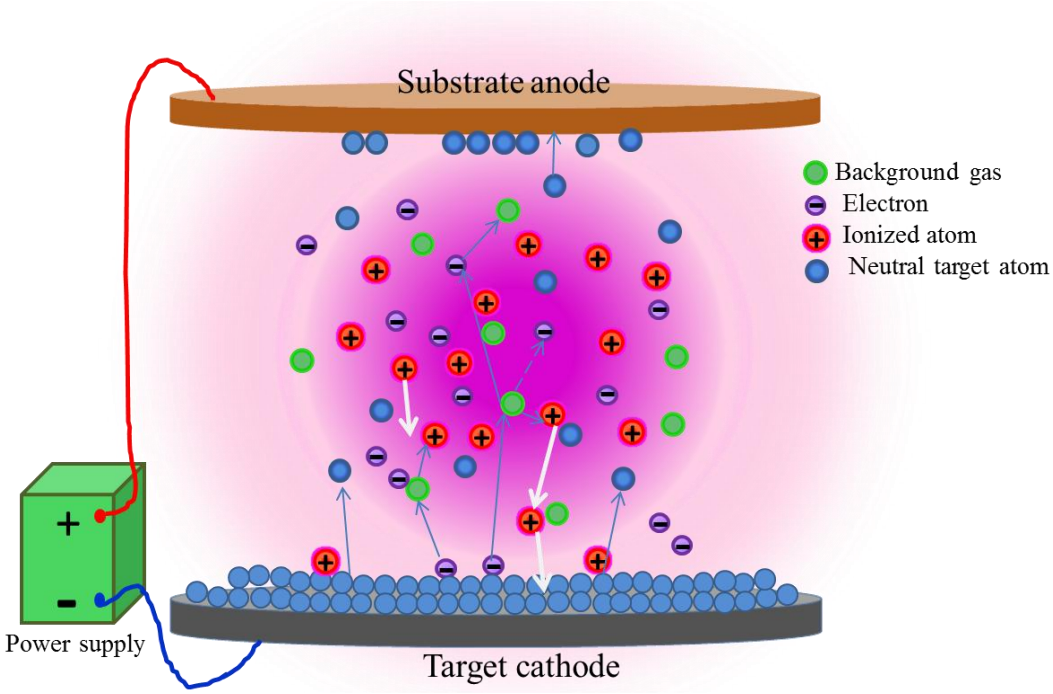

Figure 4.1: Schematic of sputtering deposition (49; 53)

In simple DC sputtering system, positive charges accumulate on the target surface and block the electron generation. It requires 10^{12} V to continue the sputtering. Such a high voltage can easily damage the target by creating electric arc. (49; 53) Ultimately, the produced coating will be destroyed. In order to solve this problem, an alternative voltage current in radio frequency (RF) 13.5MHz is used and the method is called RF Magnetron Sputtering. (53) Due to the alternative nature, the positive charges stay in the plasma and the sputtering can continue in high voltage without interruption. (49; 53) Since the sputtering happens in a high-energy

environment, it creates a very strong bonding at the coating-substrate interface at the atomic level. It creates the most uniform, dense, adhesive, and cost-effective films and coatings.

4.2.2 Electron Beam Physical Vapor Deposition (EB-PVD)

In Electron Beam Physical Vapor Deposition, a target anode is bombarded with an electron beam. The electron beam is generated from a charged tungsten filament under high vacuum. (55) Materials to be evaporated are used in the form of ingot. Electron beam can be produced using different techniques such as thermionic emission, field electron emission or the anodic arc method. The electron beam is accelerated to a high kinetic energy and directed towards the target (ingot). The atoms/molecules from the material to be deposited transform into gaseous phase by the high power impact of electrons. The gaseous flux then condenses in the solid form on the surface of the substrate to be coated. A schematic of EB deposition is shown in Figure 4.2

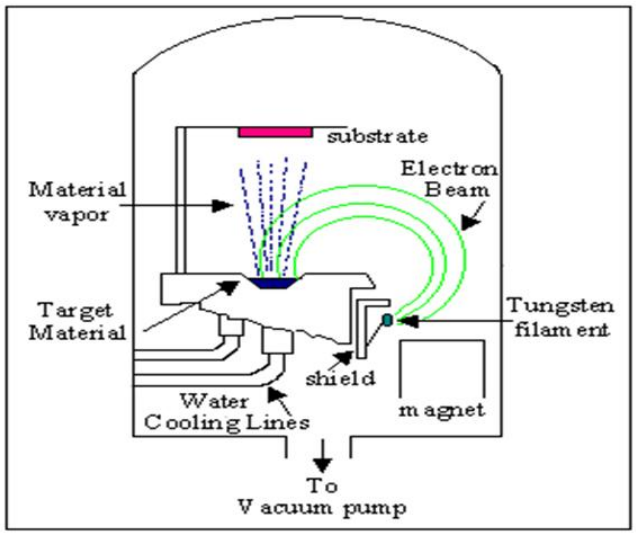

Figure 4.2: Schematic of EB deposition (56)

The accelerating voltage is required between 20 kV – 25 kV. At this high voltage the beam current is a few mA. Most of the kinetic energy of accelerated electrons (about 85%) is converted into thermal energy as the electron beam bombards the surface of the target. As a result, the surface temperature of the target ingot increases and the material starts melting to form liquid melt. The liquid ingot material evaporates under vacuum and deposits on the surface to be coated. The deposition chamber is evacuated to a pressure of 10^{-4} torr. The evaporation rate in a standard size EB set up can be in the order of 10^{-2} gm/cm^2.sec. (55) A part of incident electron energy is lost in the excitation of X-rays and secondary emission. The ingots are enclosed in a small crucible made of copper which is cooled by water circulation. The constant level of molten liquid pool on the surface of the ingot is maintained by the vertical movement of the ingot. More than one ingot feeder can be used based on the type and quality of the material to be deposited. Since more than one electron gun can be used in one chamber, each having a power from tens to hundreds of kW, EB-PVD is a method of high deposition rate. The deposition rate ranges from 0.1 μm/min to 100 μm/min at relatively low substrate temperatures and with very high material utilization efficiency. The EB gun can be accelerated in various directions ranging from straight self-acceleration to electromagnetic deflection in angle of 180° or 270° as shown in Figures 4.3(a) and 4.3(b). The copper crucible for target material can be either pocket type or continuous ingot feeding through a copper-cooled crucible (Figure 4.3c as marked A, B, and C). The continuous feeding is used for the larger quantity evaporation. (57)

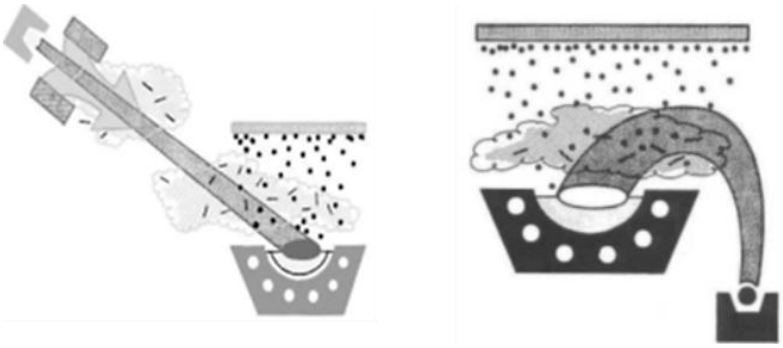

a) b)

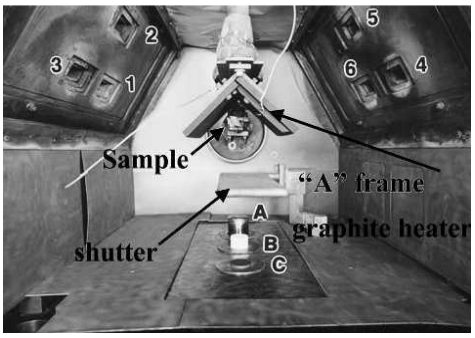

c)

Figure 4.3: Schematic diagram showing (a) straight, (b) 90° electromagnetic deflected electron beam, and (c) EB-PVD chamber showing six EB guns (1-6), three continuous ingots (A-C) feeding system (57)

The following are the advantages of EBPVD:

-Wide flexibility of deposition rate ranging from 1 nm per minute to as high as few micrometers per minute

-The high material utilization efficiency relative to other methods

-Better control on structure and morphology of film

-Due to the high deposition rate, this process has been widely used in industrial applications

However, some of the limitations of EBPVD are:

-It is a line-of-sight deposition process

-This process cannot be used to coat the inner surface of complex geometries

-The filament degradation in the electron gun results in a non-uniform evaporation rate

4.3 Target Preparation

Yttria stabilized hafnia (YSH) target (5.0 cm diameter and 0.3 cm thickness) was used to fabricate the YSH based thermal barrier coatings. YSH target is shown in Figure 4.4.

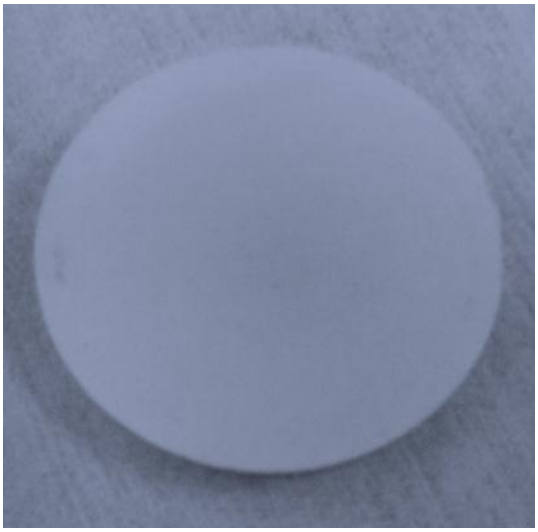

Figure 4.4: YSH target

YSHZ targets of mixed compositions were made with mixed proportions of HfO_2 and ZrO_2 stabilized by Y_2O_3. The composition of the target material was varied by varying the ratio of HfO_2 and ZrO_2 while keeping the Y_2O_3 stabilizer content constant at 7.5 mol%. The ratio of HfO_2 and ZrO_2 was varied in the proportions of 4:1, 2:1, 1:1, 1:2 and 1:4. The composition was then stabilized with yttria at 7.5 mole% of the total amount of material including yttria. The composition is summarized in Table 4.1.

Table 4.1: Composition of the target materials

Target	**Molar ratio of HfO_2 to ZrO_2**	**Amount of Y_2O_3**
YSH	1:0	7.5%
YSHZ-1	4:1	7.5%
YSHZ-2	2:1	7.5%
YSHZ-3	1:2	7.5%
YSHZ-4	1:4	7.5%
YSHZ-5	1:1	7.5%

Stoichiometric amounts of HfO_2, ZrO_2 and Y_2O_3 powders were mixed thoroughly along with small amount of poly vinyl alcohol (PVA) binder. The mixture was then subjected to very high pressure compression to make a 5 cm pellet in a die at a pressure of 24000 lbs for 30 minutes followed by sintering at 1050 ^{0}C for 24 hrs. The target of 5 cm diameter and 0.3 cm thickness thus obtained was fixed to a 5 cm Cu backing plate at the bottom of the pellet using an epoxy glue to get the stable target ready to be used for TBC deposition. Additionally, pellets of 0.78 cm diameter were also prepared following the same procedure. These small diameter pellets were prepared in order to investigate the properties of bulk materials with the same composition as that in dense coatings. The sequential steps for the target fabrication are shown in Figure 4.5.

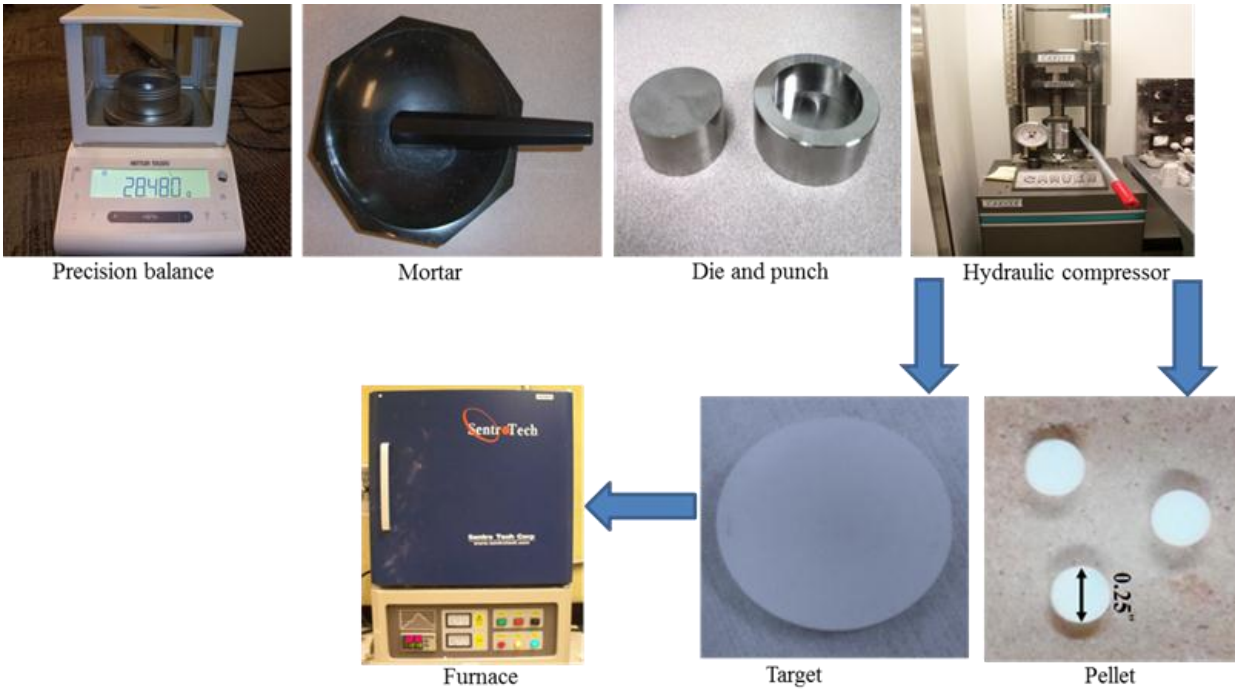

Figure 4.5: Sequential steps for the fabrication of YSHZ targets

4.4 Coatings' Deposition Procedure

Two physical vapor deposition methods namely sputtering and electron beam physical vapor deposition (EBPVD) were employed in this research to fabricate the coatings. The experimental setup for sputtering is shown in Figure 4.6. The YSH/YSHZ target was placed on a 5 cm sputter gun, which was correspondingly placed at a distance of 8 cm from the substrate. A high vacuum was produced in order to create the plasma. When the level of $3x10^{-6}$ torr was achieved, a sputtering power of 30W was initially applied to the target while introducing high purity argon (Ar) into the chamber causing plasma ignition. Once ignited, the power was increased to 100 W to deposit the coatings. The flow of the Ar was controlled using MKS mass flow meter. Before each deposition, the YSH-target was pre-sputtered for 10 minutes using Ar

with the shutter above the gun closed. A variety of operating parameters were used to optimize the deposition conditions. Starting from room temperature, various substrate temperatures up to 500 ^{0}C were maintained for all substrates to optimize the operating temperature for well and uniform growth of TBC. The substrates were heated by halogen lamps and the desired temperature was controlled by Athena X25 controller. Various deposition durations were maintained to grow the TBC with different thicknesses. Various gas (Ar) velocity were used to optimize the plasma flow for forming uniform thin film on substrates. The whole deposition was carried out at a constant vacuum level of 4.10×10^{-3} torr.

Figure 4.6: Magnetron sputtering setup

In EBPVD system, the evaporating material was used in the form of ingots. A graphite crucible filled with the evaporating materials (YSH or YSHZ) was placed in EB gun system. The gun is designed in such a way that there are four crucibles which can be moved mechanically to change the materials for evaporation. The substrates to be coated were placed at a distance of 20

cm above the evaporating materials placed in the crucible. The chamber was then evacuated to a level of 10^{-6} torr. After getting the desired vacuum, the current was increased slowly up to 280 mA using 8.16 kV. Before each deposition, the pre-evaporation was carried out for 10 minutes keeping shutter closed above the gun and then the deposition was carried out at 10^{-5} torr. The operating conditions are summarized in Table 4.2. After every deposition, the samples were subjected to a heat treatment at 600 ^{0}C for 6 hrs. in order to enhance the proper crystal growth. The EBPVD setup for coating deposition is shown in Figure 4.7.

Table 4.2: Operating conditions for TBC deposition using EBPVD

Evaporation materials	**Experimental Parameters**				
	Substrate material	**Vacuum level (torr)**	**Deposition pressure (torr)**	**Current (mA)**	**Substrate temp (^{0}C)**
7.5 YSH	Inconel-738 SS-403	10^{-6}	10^{-5}	100	27
YSHZ-1	Inconel-738 SS-403	10^{-6}	10^{-5}	100	27
YSHZ-4	Inconel-738 SS-403	10^{-6}	10^{-5}	100	27

Figure 4.7: The EBPVD setup for coating deposition

4.5 Deposition of Bond Coat

The bond coat of Nickel aluminide alloy (NiCoCrAlY) was grown on substrates using plasma pray. A 100 µm thick layer of bond coat was deposited on two types of substrates SS-403 and Inconel-738. A heat treatment was performed at 600 ^{0}C for 6 hrs just after the deposition in order to allow the substrates to react with the bond coat properly. Some of the bond coated substrates and the top coat grown by EBPVD on the bond coat are shown in Figure 4.8.

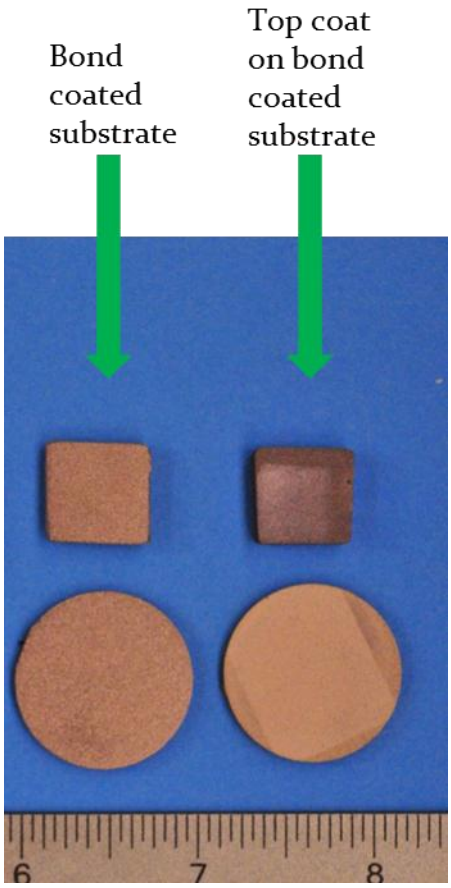

Figure 4.8**:** Bond coated substrates and the topcoat grown by EBPVD on the bond coat

4.6 Characterization

Literature review and analysis indicates that the nano-crystalline coating can be grown in either cubic or monoclinic structure based on the operating conditions, specially, the temperature and oxygen pressure. The ordered nanostructured YSH and YSHZ were developed by optimizing the operating conditions and a comparative study was performed through characterization by using different analytical methods.

4.6.1: Thickness

The thickness was measured from the crosssectional images obtained by using Scanning Electron Microscopy (SEM). The thickness was also confirmed by measuring with Rutherford Backscattering (RBS). In RBS technique, the measurement was performed using a 3.0-MV tandem electrostatic accelerator. A helium beam with an energy of 2000 KeV in an incident angle $\alpha = 7°$, the exit angle $\beta = 15°$, a scattering angle $\theta = 150°$ and a detector resolution of 20 KeV was used to perform the measurement. The data was fitted using the software SIMNRA and the composition and thickness were estimated using the data.

4.6.2: Crystal Structure and Phase Analysis - X-ray Diffraction (XRD)

Structural characterization of the fabricated TBCs was performed by using X-ray diffraction (XRD). Bruker D8 Advance x-ray diffractometer as shown in Figure 4.9 was employed for the crystal structure and phase analysis of the coatings.

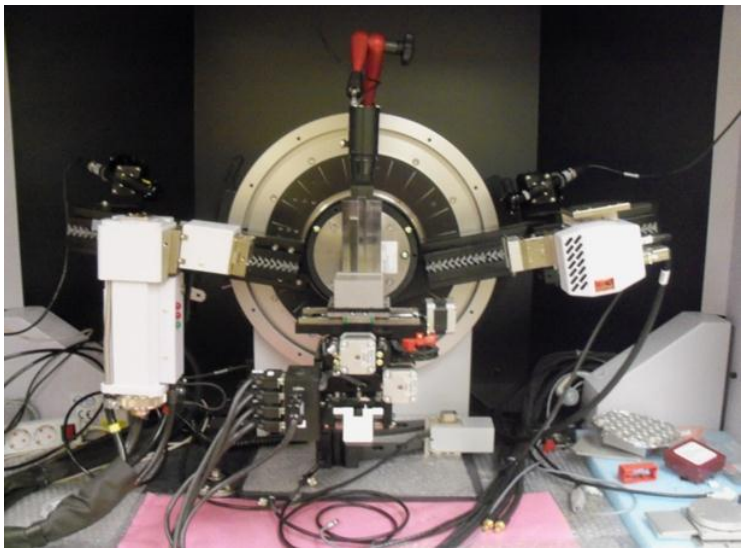

Figure 4.9: Bruker D8 Advance x-ray diffractometer

All the measurements were made ex-situ as a function of the coatings' fabrication conditions. XRD patterns were recorded using CuKα radiation (λ=1.54056 Å) at RT. The coherently diffracting domain size (d_{hkl}) was calculated from the integral width of the diffraction lines using the well-known Scherrer's equation after background subtraction and correction for instrumental broadening.

The Scherrer equation is: (58)

$$d_{hkl} = 0.9\lambda/\beta\cos\theta \quad (1)$$

where d_{hkl} is the grain-size, λ is the wavelength of the X-rays employed, β is the width of a peak at half of its intensity, and θ is the angle of the peak. Bragg's law was used to calculate the inter-planar spacing, $d_{(hkl)}$, from $2\Theta_{(hkl)}$. Lattice parameters were calculated using the formula:

$$2d\sin\Theta = n\lambda \quad (2)$$

and

$$d = a/\sqrt{(h^2+k^2+l^2)} \quad (3)$$

where d is the inter-planer distance, Θ is the diffraction angle, λ is the wavelength of the X-rays used, a is the lattice parameter, and h, k and l are plane indices. Thermal stability at high temperature was investigated by using the high-temperature XRD analysis in the XRD machine employing hot-stage, where the sample is mounted on a ceramic bed. The temperature was ramped at 10°/min and kept at the desired temperature for 30 min. The programmed XRD scans were collected right after reaching the temperature, after 15 min, and finally at 30 min duration before proceeding to the next temperature. Approximately 15 min was required to finish a full scan at a scan speed of 5°/min. The temperature was increased in steps of 100 ^{0}C until the temperature of 1300 ^{0}C is reached.

4.6.3: Surface Morphology and Interface Analysis

Optical Microscopy (OM), Scanning Electron Microscopy (SEM) and Transmission Electron microscopy (TEM) were used to study the surface and interface morphology. Surface and interface structural analysis was performed using a Hitachi S-4800 SEM as shown in Figure 4.10. Secondary electron imaging was performed to probe the surface morphology and grain distribution characteristics. The grain orientation, size-analysis and statistical analysis was performed using the software provided with the SEM. The cross-sectional images were obtained using SEM to analyze the substrate-coating interface and the growth behavior the coatings. The cross-sectional images were also obtained by TEM to investigate the oxidation behavior and thermally grown oxide in the interface between the coating and substrate.

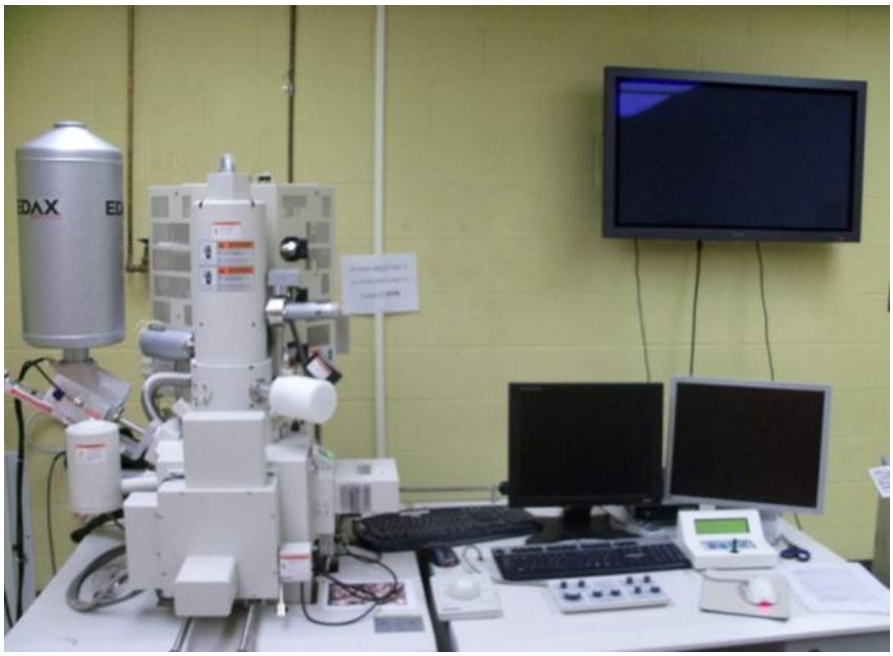

Figure 4.10: Hitachi S-4800 Scanning Electron Microscope with EDS system

4.6.4: The Composition and Chemical State

The composition of the elements in the coating has a significant effect on the performance of the TBCs. The properties like thermal conductivity and chemical resistance are greatly influenced by the elemental composition of the coating. Energy dispersive x-ray spectroscopy (EDX) coupled with the scanning electron microscopy and X-ray photoelectron spectroscopy (XPS) were used to analyze the composition of the TBCs. In EDX system, the elemental composition was investigated by analyzing the generated X-rays from the samples by using an incident electron beam of 20 keV. As the energy of the X-ray is characteristic of the element from which it is emitted EDX detector can detect various elements consisting the coating. The elemental mapping was carried out on the surface of the samples using the same EDX detector to analyze the distribution of different elements all over the sample. The interaction between i)Y^{+3} and Hf^{+4} in YSH, ii) Y^{+3}, Hf^{+4} and Zr^{+4} in YSHZ was analyzed to get the deeper understanding about the effect of oxidation state on the thermal conductivity. The oxidation state was evaluated using XRD, TEM and XPS which provided insightful mechanisms of various interactions that can influence the TBCs performance. Elemental mapping developed by using the secondary electron scanning was investigated to understand the distribution of the components present in the coating.

4. 6. 5: Thermal Conductivity

Two different methods i) photo-acoustic (PA) and ii) time-domain thermo-reflectance (TDTR) were used to measure the thermal conductivity.

In photo-acoustic method, a laser beam operating at a wavelength of 0.8 mm was used as the heating source. The laser is periodically irradiated on the sample surface. The substrate material and the additional surrounding medium layer are considered to be thermally thick compared to the YSH coating. The laser beam is concentrated using a mirror and directed to the YSH sample, which is mounted at the bottom of the PA cell. The condenser microphone senses the PA signal and transfers it to the lock-in amplifier, which is used to measure the amplitude and phase of the acoustic signal. A least square fitting procedure is used to determine unknown thermal conductivity and thermal contact resistance. The phase shift of the PA signal at each experimental frequency is calculated using the trial value of unknown properties**.** The schematic diagram of the photo-acoustic apparatus is shown in Figure 4.11.

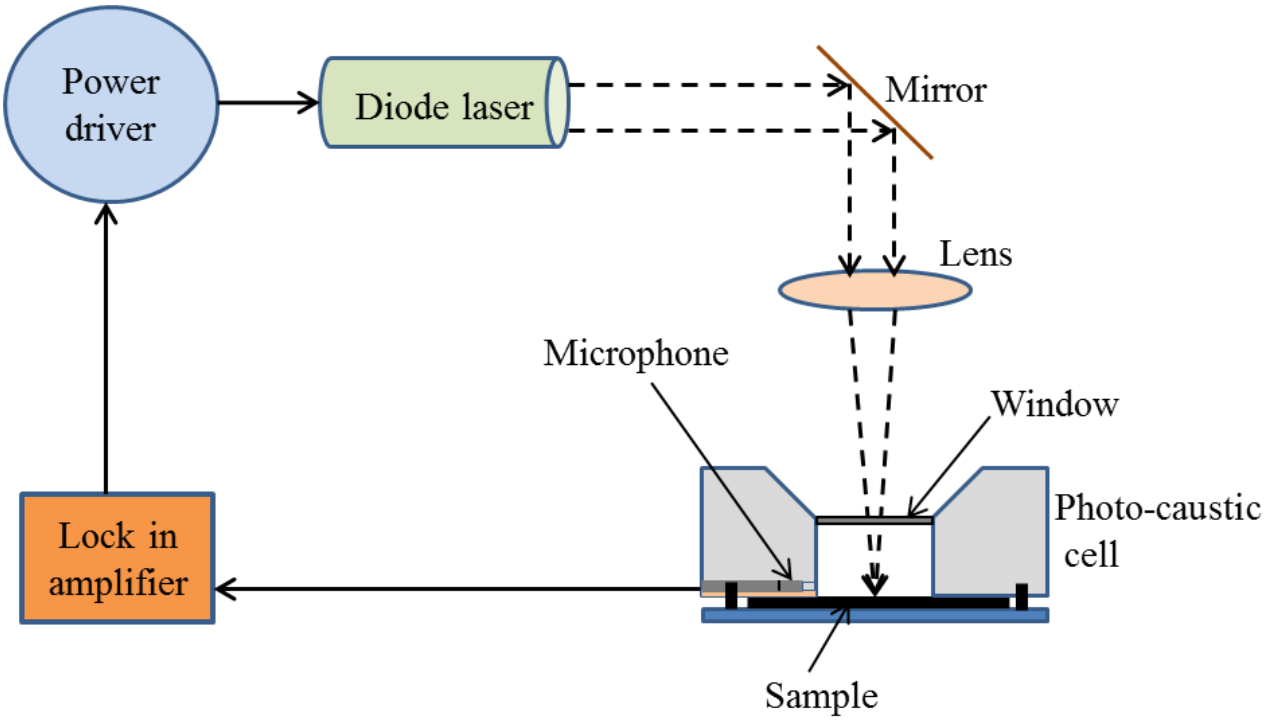

Figure 4.11: Schematic diagram of the photo-acoustic apparatus

In TDTR method, thermal conductivity was measured using a two color time-domain thermo-reflectance (TDTR).

The YSH samples were coated with thick layer of Al using sputtering deposition to produce a high reflectivity surface. Thickness of the Al layer was maintained in the range of ~80−100 nm. Thus the entire sample consists of three consecutive layer Si substrate, YSH coating, and reflecting Al over layer as schematically shown in Figure 4.12.

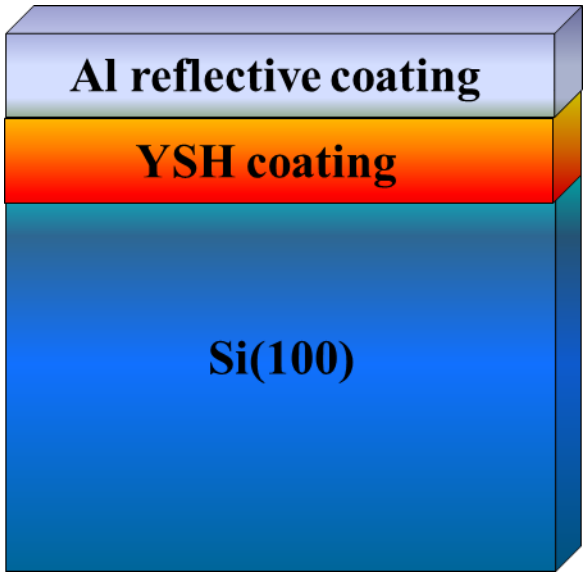

Figure 4.12: Schematic diagram of three consecutive layers: Si substrate, YSH coating, and reflecting Al over layer for the thermal conductivity measurements.

A vacuum chamber with a base pressure of $<1 \times 10^{-7}$ Pa was created to deposit the high purity reflecting Al film using magnetron sputtering. A sputtering target of 5 cm in diameter and >99.99% pure Al was used with a power density of ~50 W in a 0.2 Pa Ar background. The deposition was carried out at room temperature keeping the samples insulated from ground during Al deposition. Thermal conductivity of a pure, nanocrystalline, monoclininc HfO_2 sample

of comparable grain size was also studied following the same TDTR method in order to compare to the thermal conductivity of nanocrystalline YSH.

A frequency domain model was used to analyze the data for the estimation of thermal conductivities. The ratio of the in-phase and out-of phase lock-in amplifier signals is calculated as a function of time. (59)

$$-\frac{V_{in}}{V_{out}} = \frac{\sum_{-m}^{m}\left(\Delta T\left(m/\tau + f\right) + \Delta T\left(m/\tau - f\right)\right)\exp\left(i2\pi mt/\tau\right)}{i\sum_{-m}^{m}\left(\Delta T\left(m/\tau + f\right) - \Delta T\left(m/\tau - f\right)\right)\exp\left(i2\pi mt/\tau\right)} \tag{4}$$

where,

m = integer denoting summation over pump pulses

τ = time between unmodulated laser pulses (12.5 ns)

f= modulation frequency (9.8 MHz)

t = time delay between pump and probe pulses

The function ΔT is calculated with the Feldman matrix algorithm as described by D. G. Cahill (59) using the expression,

$$\Delta T = 2\pi A \int_{\infty}^{\infty} G(k) e^{-(\pi k w)^2} k dk \tag{5}$$

where,

A = absorbed laser fluence

w = spot radii of the focused pump and probe beams (assuming equal Gaussian profiles) and

k = an inverse space variable

For layered structures, the function G (k) is calculated with the Feldman matrix algorithm (59)

Electron−phonon coupling, which allows the Al film to reach a uniform temperature, is not equilibrated by the time less than 100ps. Furthermore, this regime is also disturbed by the picosecond acoustics. Therefore, data for pump advance times earlier than t = 100 ps were not taken into account. If the sample thickness is comparable to the thermal penetration depth, the TDTR experiment becomes sensitive to the nature of the substrate. Since the sample thicknesses was comparable to the thermal penetration depth of the experiment $(D/2\pi f)1/2 \approx 100$ nm a five-layers system was used. Here D is the thermal diffusivity of the sample layer and F is the TDTR modulation frequency.

4.6.6: Mechanical Properties

Nanoindentation technique was used to evaluate the mechanical properties. Hardness (H), modulus of elasticity (Es), reduced modulus of elasticity (Er), stiffness (s) and strain rate sensitivity were estimated using appropriate mathematical expressions for YSH and YSHZ coatings. A diamond tip sharp nanoindenter was forced into the sample while both the force and indentation depth were recorded continuously. The diamond tip whose geometry and mechanical properties are known was pressed into the sample. The load placed on the indenter tip was increased as the tip was penetrating more into the sample until it reached the defined maximum depth of 85 nm. At the maximum depth the load was hold constant for set time and then removed. The area of the indentation in the sample was measured using the known geometry of the indentation tip. Atomic force microscopy was utilized to image the indentation area on the sample surface. A record of these values was plotted to create a load-displacement curve and the

mechanical properties were calculated using the corresponding relations as described by Oliver and Pharr. (60) A schematic illustration of load-displacement plot is shown in Figure 4.13.

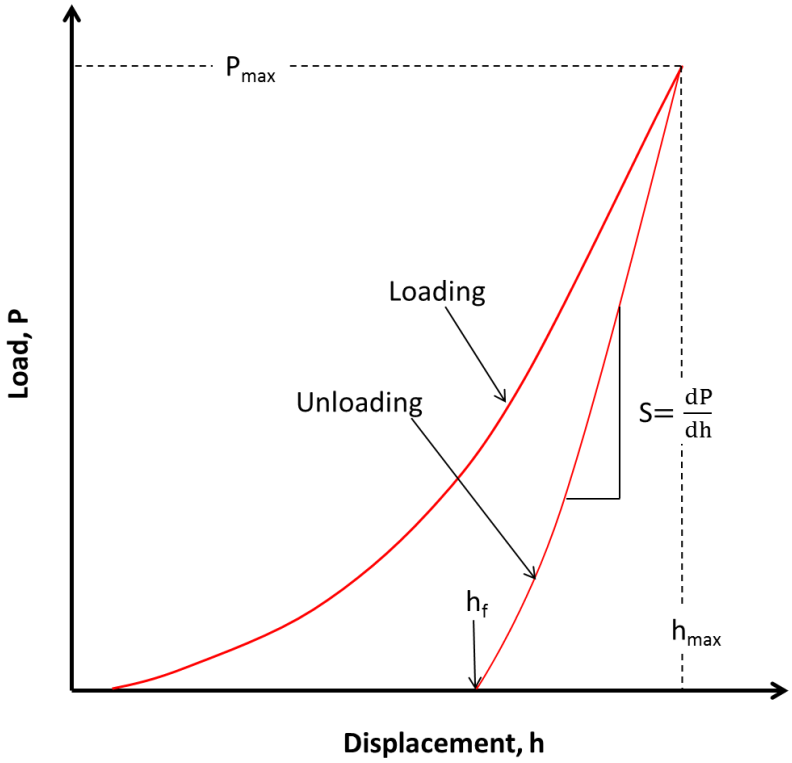

Figure 4.13: Schematic illustration of load-displacement data

Hardness, H is defined as the maximum load, P_{max} divided by the residual indentation area A_r,

$$H = \frac{P_{max}}{A_r} \tag{6}$$

The slope of the curve, dP / dh, upon unloading indicates the value of stiffness S. The reduced modulus of elasticity E_r is estimated using the value of stiffness as

$$E_r = \frac{1}{\beta}\frac{\sqrt{\pi}}{2}\frac{S}{\sqrt{A(h_c)}} \tag{7}$$

where,

$A(h_c)$ = area of the indentation at the contact depth h_c

h_c =the depth of the residual indentation prior to elastic recovery of its shape

β =geometrical constant on the order of unity

The modulus of elasticity E_s is related to the reduced modulus of elasticity E_r as

$$\frac{1}{E_r} = \frac{(1-\vartheta_i^2)}{E_i} + \frac{(1-\vartheta_s^2)}{E_s} \tag{8}$$

where, the subscript i indicates a property of the indenter material and ν is Poisson's ratio. For a diamond indentor tip, E_i is 1140 GPa and ν_i is 0.07. Poisson's ratio varies between 0 and 0.5 and is typically around 0.3.

The strain-rate sensitivity of the flow stress m is defined as

$$m = \frac{\partial \ln \sigma}{\partial \ln \dot{\varepsilon}} \tag{9}$$

where,

σ= flow stress

$\dot{\varepsilon}$ = strain rate produced under the indenter

m is determined as

$$d\ln H = m d\ln \dot{\varepsilon}_p + n d\ln h_p \tag{10}$$

where, p indicates that these values are to be determined from the plastic components only

Residual stress analysis was performed using XRD method. The $\sin^2\psi$ technique was followed to calculate the residual stress (61-62). The variation of d-spacing was measured using the diffraction of Cu-K_α radiation by (133) planes. X-ray diffraction was carried out at various tilting angle. A linear relation is obtained between the inter-planner spacing and $\sin^2\psi$ values. A representative plot for $(d-d_0)/d_0$ is shown in Figure 4.14 which shows the d-spacing as a linear function of $Sin^2\psi$. Then the residual stress has been calculated using the following well-known expression. (61-62)

$$\frac{d_{\Phi\Psi}-d_0}{d_0} = \frac{1+\nu}{E}\sigma_\Phi \sin^2\Psi - \frac{\nu}{E}\sigma_{11} + \sigma_{22} \qquad (11)$$

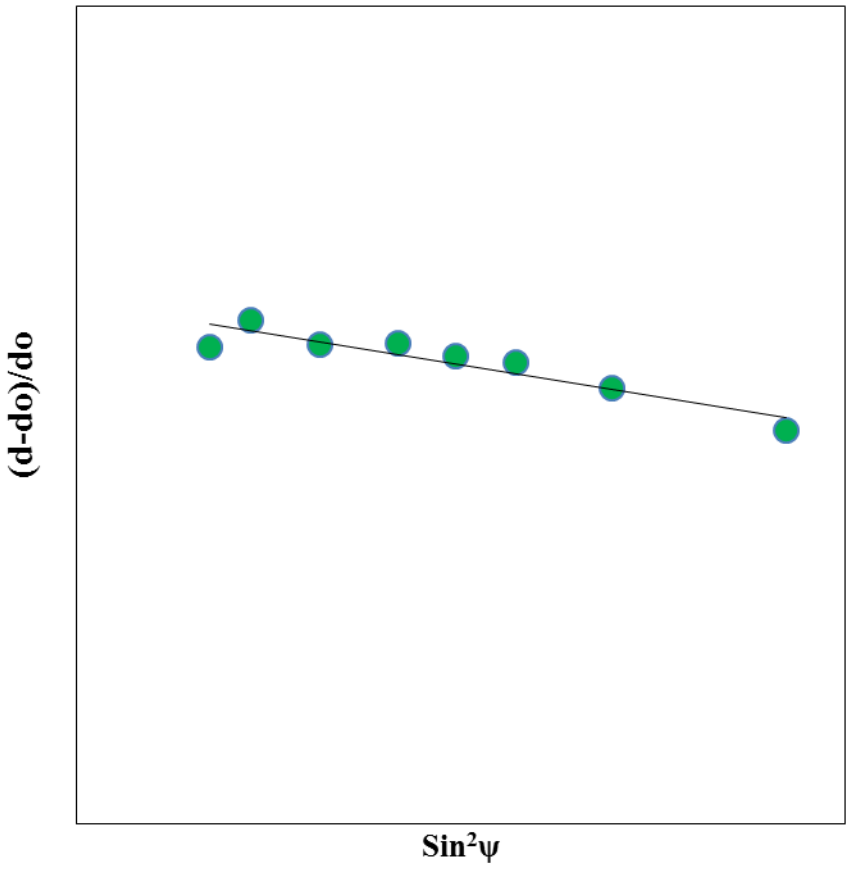

Figure 4.14: The plot showing the relation between inter-planner spacing and $Sin^2\psi$

4.6.7: Durability Test

The performance of the fabricated coating in real gas turbine environment was evaluated by exposing the coating to hot gases in a combustor. A swirl stabilized laboratory scale combustor rig was used to perform the experiments. The YSH and YSHZ samples were exposed to the hot gas produced by the combustion of methane (supplied by Air Gas Inc). The composition of the hot gases was anticipated as CO, CO_2, N_2, O_2 and unburned hydrocarbons. The gas flow rate was maintained at 20 L/min with continuous flow of air. The air fuel ratio was maintained in an optimum value in order to keep the flame stabilized without any interruption from flashback or blowout. The average flow rate of air was 198 L/min. The angle used for the hot gas impingement was 90^0. The sample was inserted from the top of the combustor rig using a laboratory made sample holder as shown in Figure 4.15. The sample holder was made of stainless steel so that it can withstand the hostile environment inside the combustion chamber. The sample holder was designed in such a way that the impingement angle can be changed. Samples of different sizes can be accommodated by adjusting the threaded rod coupler. R-type thermocouple was used to measure the temperature near samples inside the combustion chamber. The samples were exposed to hot gas for 16 hrs. at 1100 ^{0}C. After every specific interval, the samples were taken out and examined for crystallography, surface morphology, chemical composition and residual stress. Finally, all of these properties of the exposed samples were compared to those of the as grown sample to evaluate the performance of the coatings in the real got gas environment.

(a)

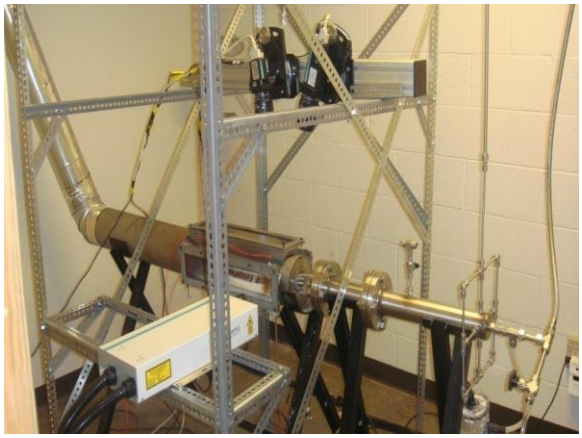

(b)

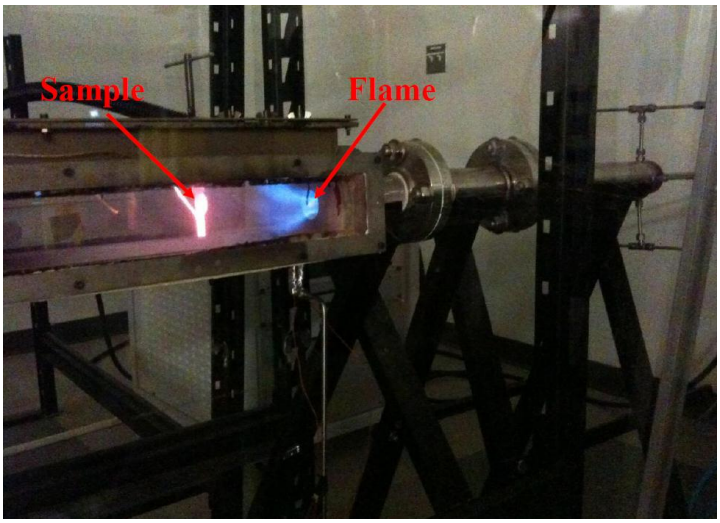

(c)

Figure 4.15: The experimental setup for the hot gas exposure test. (a) sample holder (b) the combustor rig and (c) the sample exposed to the hot gas

4.6.8: Furnace Heating and Thermal Cycling

YSH and YSHZ samples were exposed to high temperature using atmospheric furnace. The temperature is varied from 600 ^{0}C to 1500 ^{0}C. The samples were exposed to high

temperature for 12 hrs at a specific temperature and 100 ^{0}C was taken as the increasing step of temperature. After every step of temperature increment, the samples were taken out and investigated for crystallography and microstructure. The thermal cycling experiment was performed on the pellets prepared using various compositions of hafnia and zirconia keeping the yttria content constant at 7.5%. Five different compositions of hafnia and zirconia ranging 4:1, 2:1, 1:1, 1:2 and 1:4 were used for the thermal cycling experiment. A full 1 hour cycle was used taking 10 minutes for ramping the temperature to 1300 ^{0}C, keeping 40 minutes at that temperature and 10 minutes for cooling to the room temperature. Total 100 cycles duration was used for the first experiment and then continued to higher number of cycles. Microstructure was investigated after each and every thermal cycling experiment. The same procedure was followed for the YSH and YSHZ coatings grown on alumina substrates. A CM furnace was used to expose the samples to high temperature as shown in Figure 4.16.

Figure 4.16: High temperature CM furnace

4.6.9 Thermal Oxidation:

Thermal oxidation measurements were made on the coatings using the atmospheric furnace heating. Samples were exposed to 900 ^{0}C for long time using the atmospheric furnace. Samples were heated in several steps. Weight gain of the samples was measured before and after every step of thermal treatment and as function of time of thermal oxidation. In the beginning of the heating process, samples were heated for five hours, weight was measured and the amount of weight increase due to oxidation was estimated. After continuing the oxidation process for couple of steps the exposure time was increased to twenty hours and then thirty hours at same temperature.

Chapter 5: Results and Discussion

5.1 Crystallography

The XRD patterns of YSH coatings grown on SS-403 and Inconel-738 are shown as a function of growth temperature (T_s) in Figures 5.1 and 5.2 respectively. The XRD curves of YSH coatings exhibit the peaks corresponding to cubic structure of HfO_2. It is evident that the effect of growth temperature is not very significant on the phase except with an increase in the average grain size. From Figure 5.1, the peak at ~30.28° corresponds to the diffraction from (111) planes. This peak is rather broad for coatings grown at T_s=RT indicating the presence of nano-crystalline particles embedded in an amorphous matrix. It can be noted from the XRD patterns (Figure 5.1) that the (1 1 1) peak becomes sharper with increasing growth temperature. A decrease in the full-width at half-maximum (FWHM) associated with an intensity increase of the peak can be noted in the XRD data (Figure 5.1). This observation clearly indicates that the crystallinity increases with increasing growth temperature. This is also indicative of an increase in the average crystallite-size and preferred orientation of the film along (111). Monoclinic and tetragonal phases consist of several shorter Hf-O bond lengths (2.0–2.1 Å) compared to cubic HfO_2 (2.37 Å). (63) As a consequence, the strain energy because of the size mismatch becomes significant in monoclinic and tetragonal phases. On the other hand, the distortion is quite less in cubic phase with the oversized Y^{+3} doping, which makes cubic HfO_2 stable even at low temperature. Furthermore, the structural relaxation plays another role in the stabilization of cubic phase of HfO_2 by Y_2O_3 dopant. (63) The results are in good agreement with those reported by Lee et al. (63)

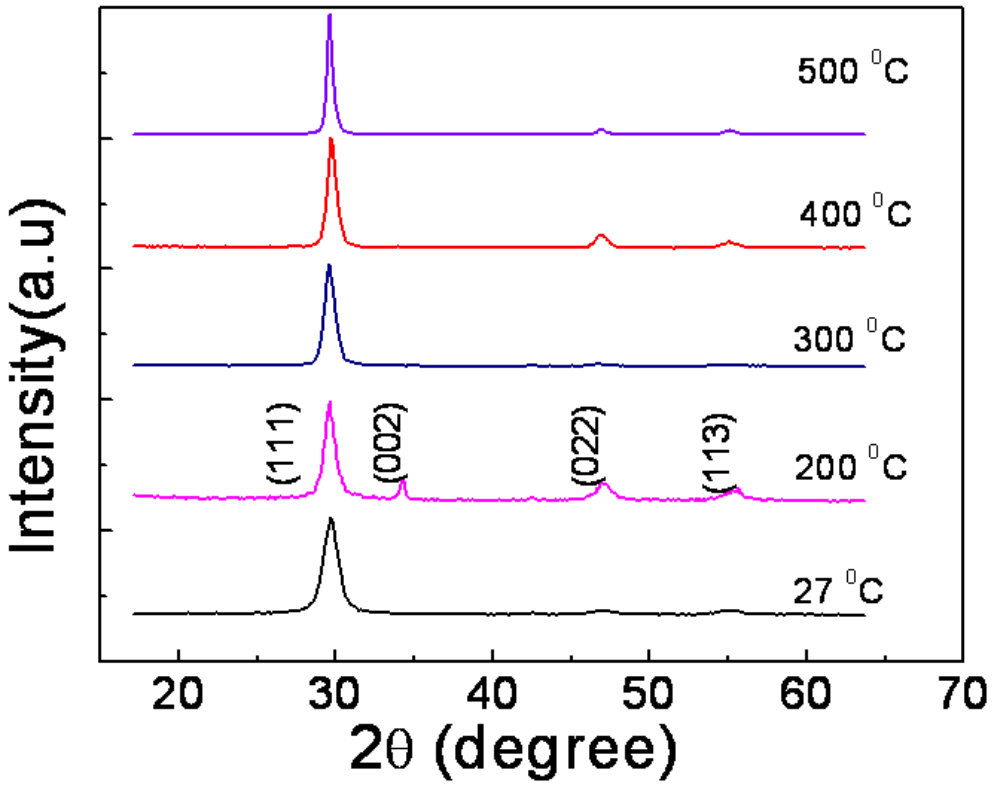

Figure 5.1: The XRD patterns of YSH coatings on SS-403 grown at various substrate temperatures.

It is evident from Figure 5.2 that the width of the peak corresponding to (111) planes decreases with the increasing temperature (to 400 ^{0}C) when YSH coatings are grown on Inconel-738. As mentioned above, the decrease in peak width is associated with the increase in crystallite size and the extent of crystallization. However, the peaks are rather broad for the sample grown at 500 ^{0}C compared to other growth temperatures. This might be because of the fact that Inconel-738 super alloy consists of several elements which possesses different thermal expansion coefficient compared to one another. At 500 ^{0}C, all these elements get enough thermal energy for lattice expansion but slightly in different magnitude. Therefore, when YSH is deposited on the super alloy at higher temperature, the peak width increases because of the wide range of the inter planner spacing while maintaining the cubic crystal structure.

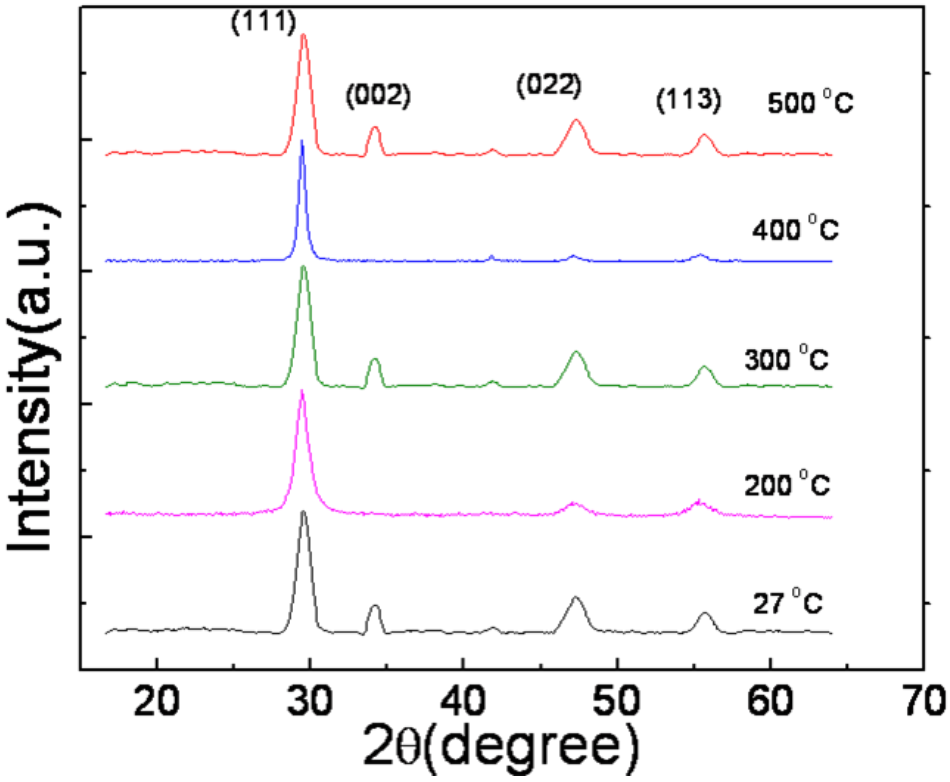

Figure 5.2: The XRD patterns of YSH coatings on Inconel-738 grown at various substrate temperatures.

Figure 5.3 shows the effect of substrate materials on the crystal structure of YSH coatings grown at same substrate temperature, 500 ^{0}C. It is evident (Figure 5.3) that the substrate materials don't show very significant effect on crystal structure of YSH coatings. YSH crystallizes in cubic structure on all of these four substrates; however, crystallization is uniform and well developed when grown on single crystal materials like Si, alumina and SS-403. Although TBCs are not directly grown on substrate these results indicate that the composition of bond coat should not have any significant effect on the microstructure of YSH coatings.

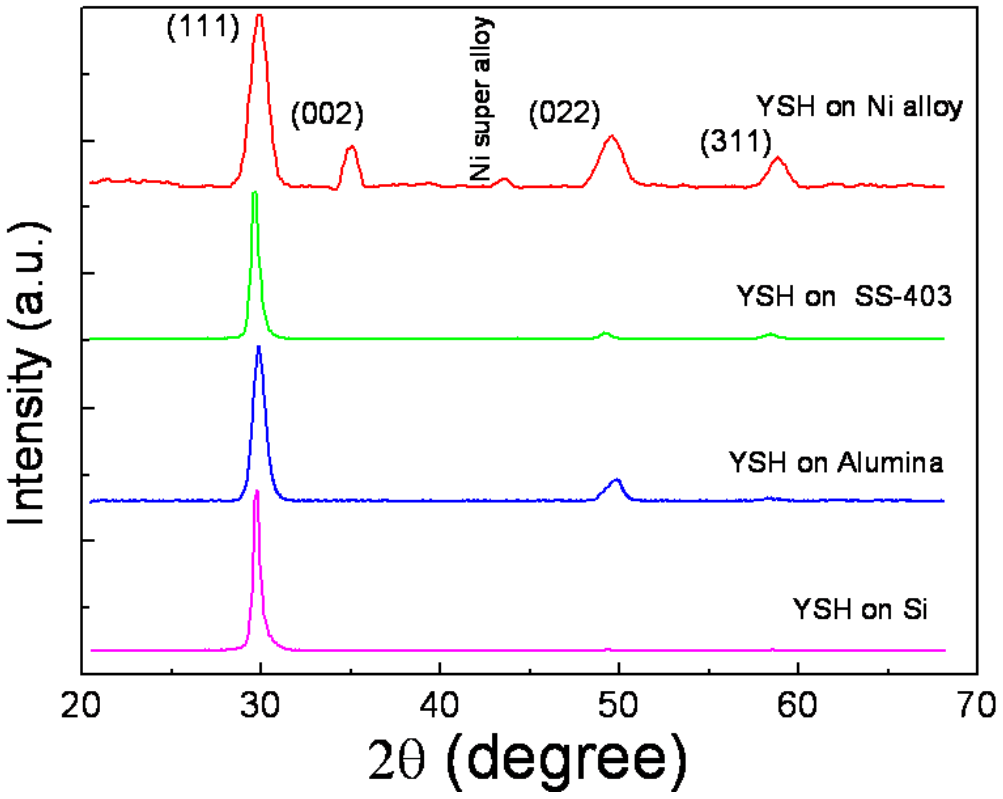

Figure 5.3: The effect of substrates on the crystal structure of YSH coatings grown at same substrate temperature, 500 ^{0}C.

The XRD patterns of the YSHZ coatings grown on alumina and stainless steel substrates are shown in Figures 5.4 and 5.5 respectively. It is evident from the XRD curves that the coatings are crystallized in the cubic structure of HfO_2. All of the compositions of hafnia and zirconia coatings on all the substrates showed the similar crystal structure (Figure 5.4 and 5.5). The effect of temperature is not significant although some peak sharpening can be seen with increasing temperature. Another important feature that can be noted in XRD data is that the patterns of YSHZ coatings are very similar to the cubic structure of YSH coatings as shown in Figures 5.1 and 5.2. This observation indicates that the stabilization of cubic hafnia phase is mainly due to the presence of yttria stabilizer. The phase stabilization is independent of the ratio of HfO_2 and ZrO_2 and the type of substrates.

It has already been established that ZrO_2 can be stabilized in cubic phase by selectively doping with Y_2O_3, CeO_2 and MgO. (41) Since Y_2O_3 exhibits cubic-centered Tl_2O_3-type structure it is possible that yttria can stabilize the hafnia in cubic structure. (64; 65; 66; 67; 68; 43). Therefore, cubic-phase stabilization in Y_2O_3–HfO_2–ZrO_2 coatings is a result of oxygen vacancy creation similar to the case of ZrO_2. The Y^{+3} ions having radii (0.96 Å) larger than that of Hf^{+4}/Zr^{+4} imparts lattice distortion and enforce the elongation of bond with oxygen in close propinquity. (63) Therefore, the stabilization of YSHZ is similar to that in YSH as described above. As seen in the XRD data (Figures 5.4 and 5.5), the cubic structure of YSHZ coatings is retained down to room temperature like YSH.

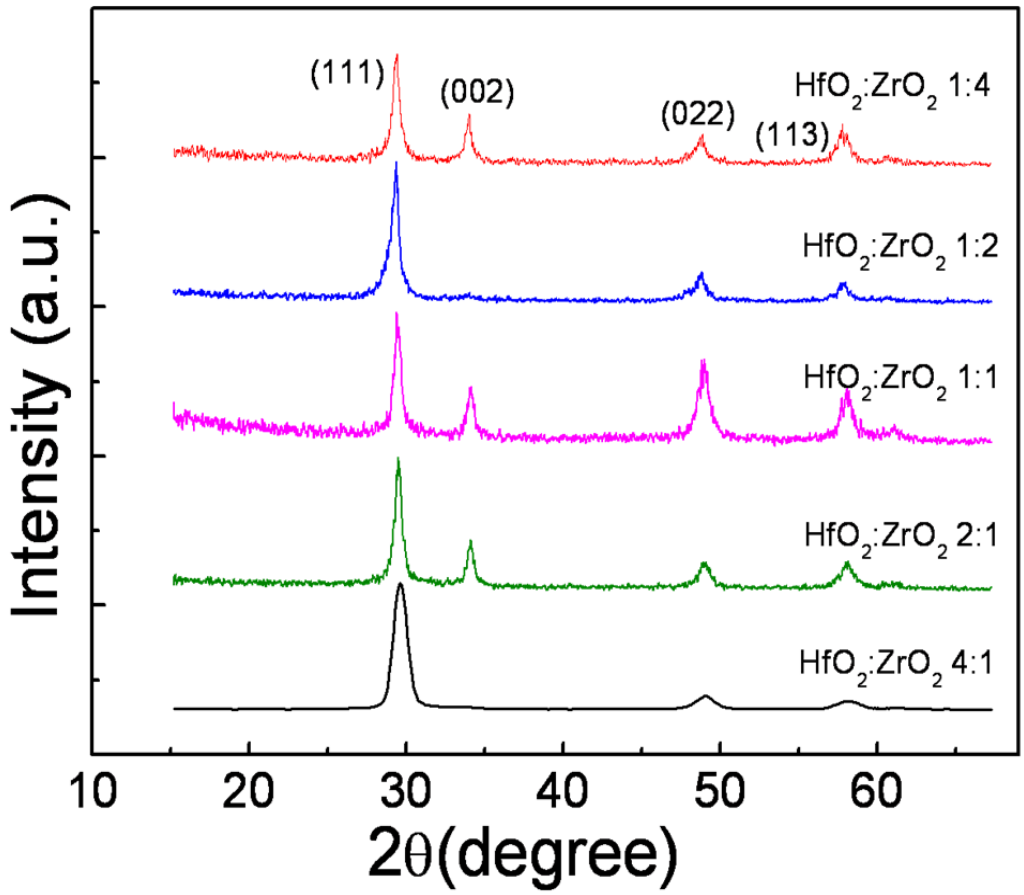

Figure 5.4: XRD curves of YSHZ coatings on alumina substrates. The observed peaks can be indexed to cubic hafnia as indicated

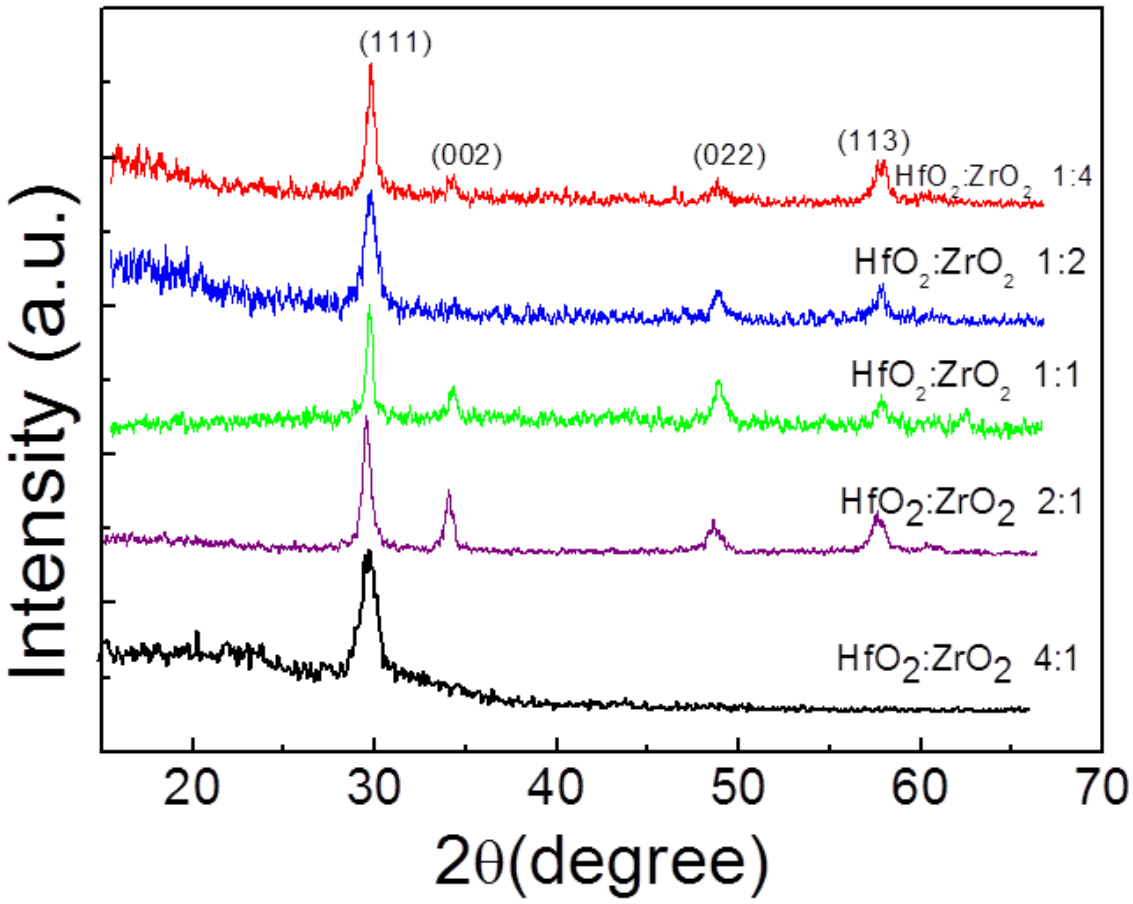

Figure 5.5: XRD curves of YSHZ coatings on SS-403 substrates. The observed peaks can be indexed to cubic hafnia as indicated

5.2 Lattice Parameter

The lattice parameter of the YSH coatings calculated from XRD data was found to be ~0.52 nm, which is close to the reported value of cubic hafnia. (69) The lattice parameters exhibit a decreasing trend from 5.25 to 5.20 (±0.001) Å with T_s (room temperature to 500 ^{0}C). Figure 5.6 shows the variation of lattice parameter with T_s. We attribute this decrease in lattice parameter to the changes in lattice-strain and crystallite size in nanocrystalline YSH films with

increasing T_s. The lattice constant obtained for YSH coatings is larger as compared to that of pure HfO_2 (5.09Å). (63) This lattice expansion in YSH compared to pure HfO_2 is caused by the addition of 7.5% Y_2O_3 and can be understood as follows. The ionic radii of Y^{+3} (0.96 Å) is larger than that of Hf^{+4} which introduces lattice distortion and enforce the elongation of bond with oxygen in close proximity. However, there is an increasing trend of the lattice constant with increasing ZrO_2 in YSHZ coatings. The lattice constant variation with ZrO_2 content of the YSZH coatings grown on SS-403 is shown in Figure 5.7. Enhancement in the lattice parameter with a progressive increase in the ZrO_2 concentration is due to the interactions of Zr^{+4} and Hf^{+4} ions. While the charge and radius of the zirconium and hafnium ions are more or less similar, the lattice parameter of cubic Y_2O_3–ZrO_2–HfO_2 coatings seems to be influenced by the ZrO_2 addition since the ionic radius of Zr^{+4} is slightly higher than that of Hf^{+4} (48). The physical mechanisms involved in the lattice parameter variation of Y_2O_3–ZrO_2–HfO_2 coatings can be understood as follows. The lattice parameter enhancement, in general, in Y_2O_3–HfO_2–ZrO_2 coatings compared to pure HfO_2 is caused by the addition of 7.5% Y_2O_3 and associated lattice distortion and elongation of bonds. (63) The lattice distortion increases when the number of Zr^{+4} ions is more than the Hf^{+4} ions in the matrix leading to overall lattice expansion to accommodate the Y^{+3}, Zr^{+4} and Hf^{+4} ions.

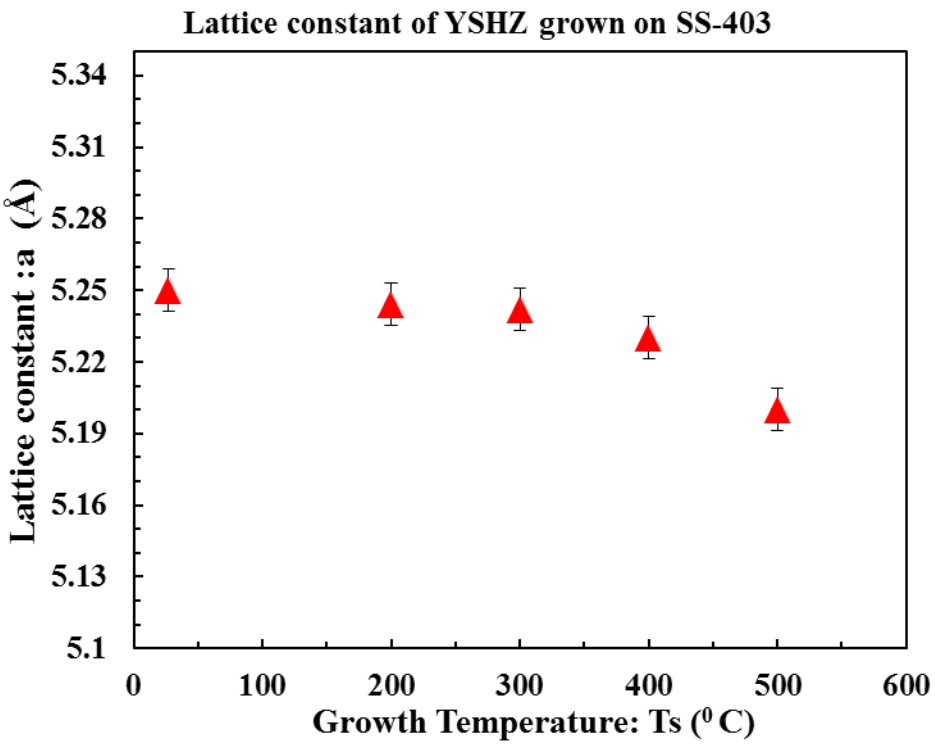

Figure 5.6: The variation of lattice parameter with Ts

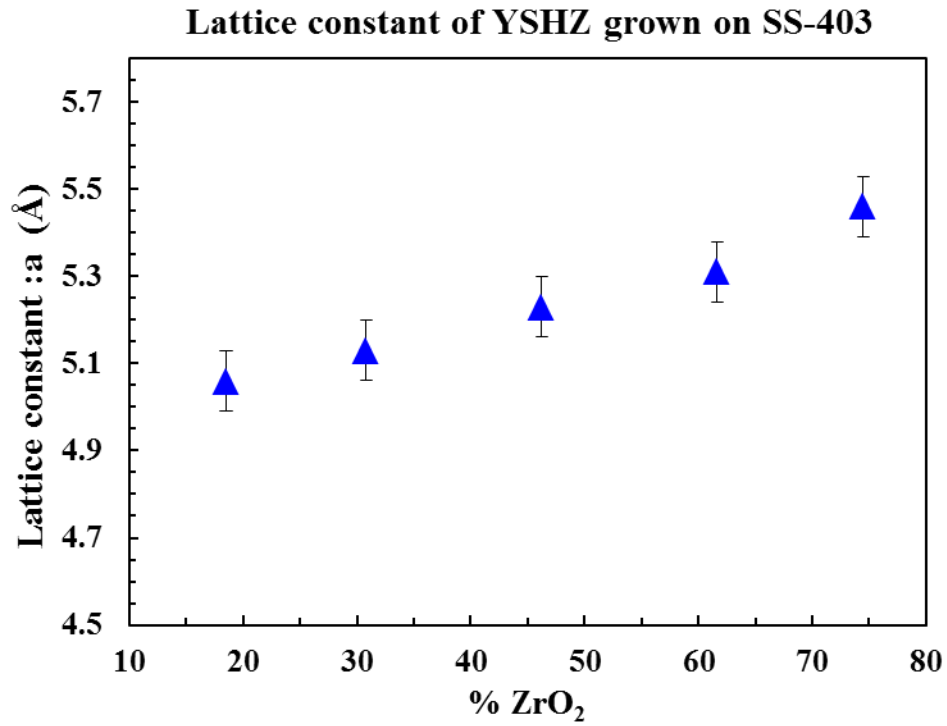

Figure 5.7: The variation of lattice parameter with amount of ZrO_2 in YSHZ coatings

5.3 Surface Morphology

The SEM images indicating the surface morphology of the YSH coatings are shown in Figure 5.8 as a function of growth temperature. The morphology of the coatings is characterized by thin, elongated triangular network of grains connected together to form the dense surface structure. Based on the XRD and SEM data, it seems that a temperature of 300 ^{0}C is the critical temperature to promote ordered, oriented growth of YSH coatings. At this temperature, the grains are fully grown and uniformly distributed across the sample surfaces. Triangular shaped grains, which are oriented in a specific morphology as seen in the SEM micrographs, provides the characteristic dense structure of the YSH coatings. For thick YSH coatings, Matsumoto et al. have reported that the morphology is characterized by the presence of triangular shaped grains on the surface (9; 70). In the present case, it seems that the signature of that characteristic is present although the coating thickness and size are significantly lower. Thus, the crystal structure and well defined grain size with increasing temperature can be attributed to the effect of temperature, which increases the mobility of the surface species to account for the observed results shown in Figures 5.1, 5.2 and 5.8. When the samples are grown as thick coating, the grains tend to grow in large size after complete crystallization. The grains are still triangular shape with tiny pores all around the sample which is similar to that reported by Matsumoto et al. (9) The morphology of thick samples grown on SS-403 and inconel-738 with bond coat with and without bond coat are shown in Figure 5.9. It is evident (Figure 5.9) that the bond coat does not have any significant effect on the size, shape and orientation of the grains.

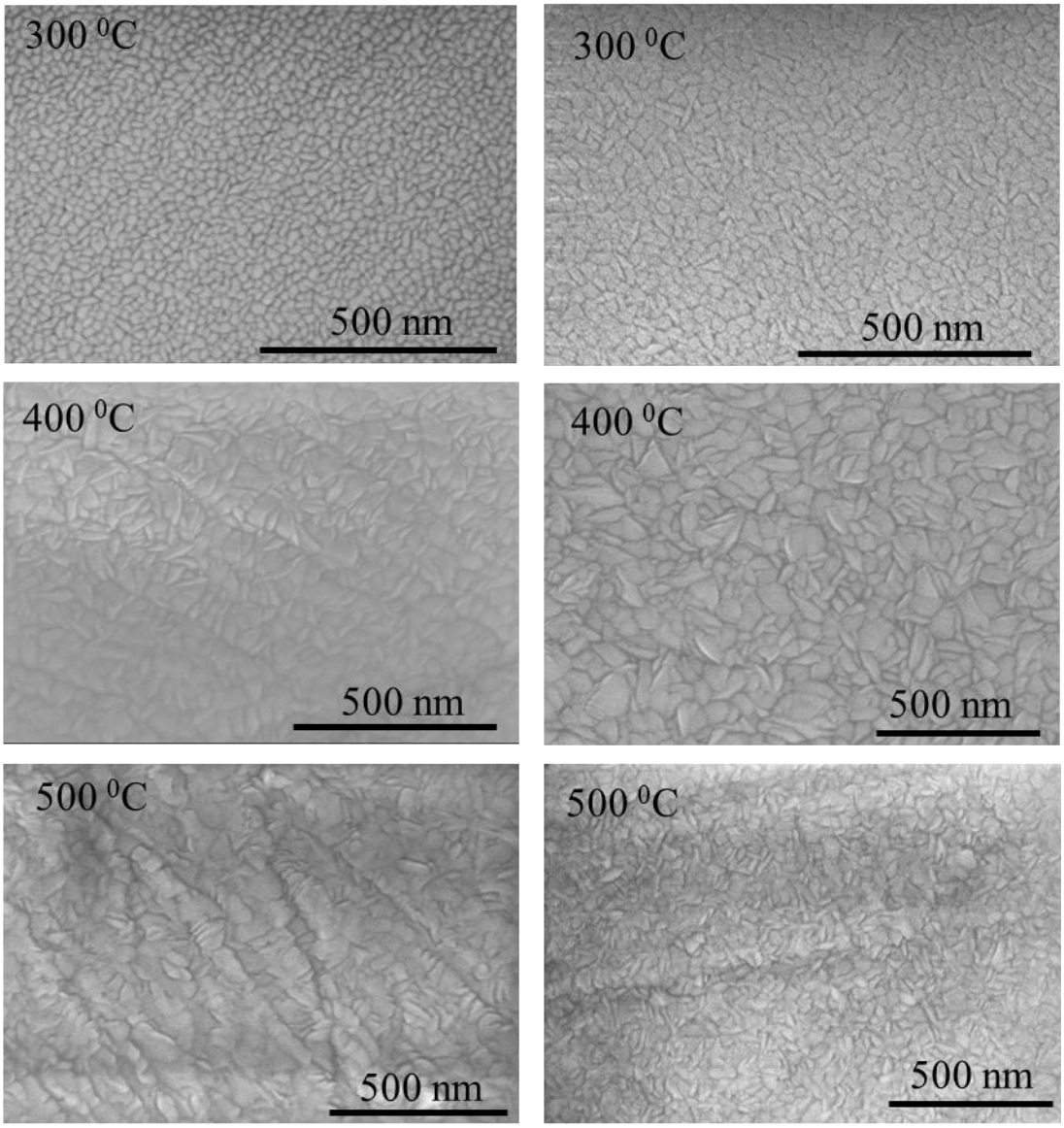

a) **b)**

Figure 5.8.: SEM images of YSH coatings on Inconel-738 (figure 5.8a) and SS-403 (figure 5.8b) substrates. A slight increase in grain size and densification with increasing growth temperature can be noted.

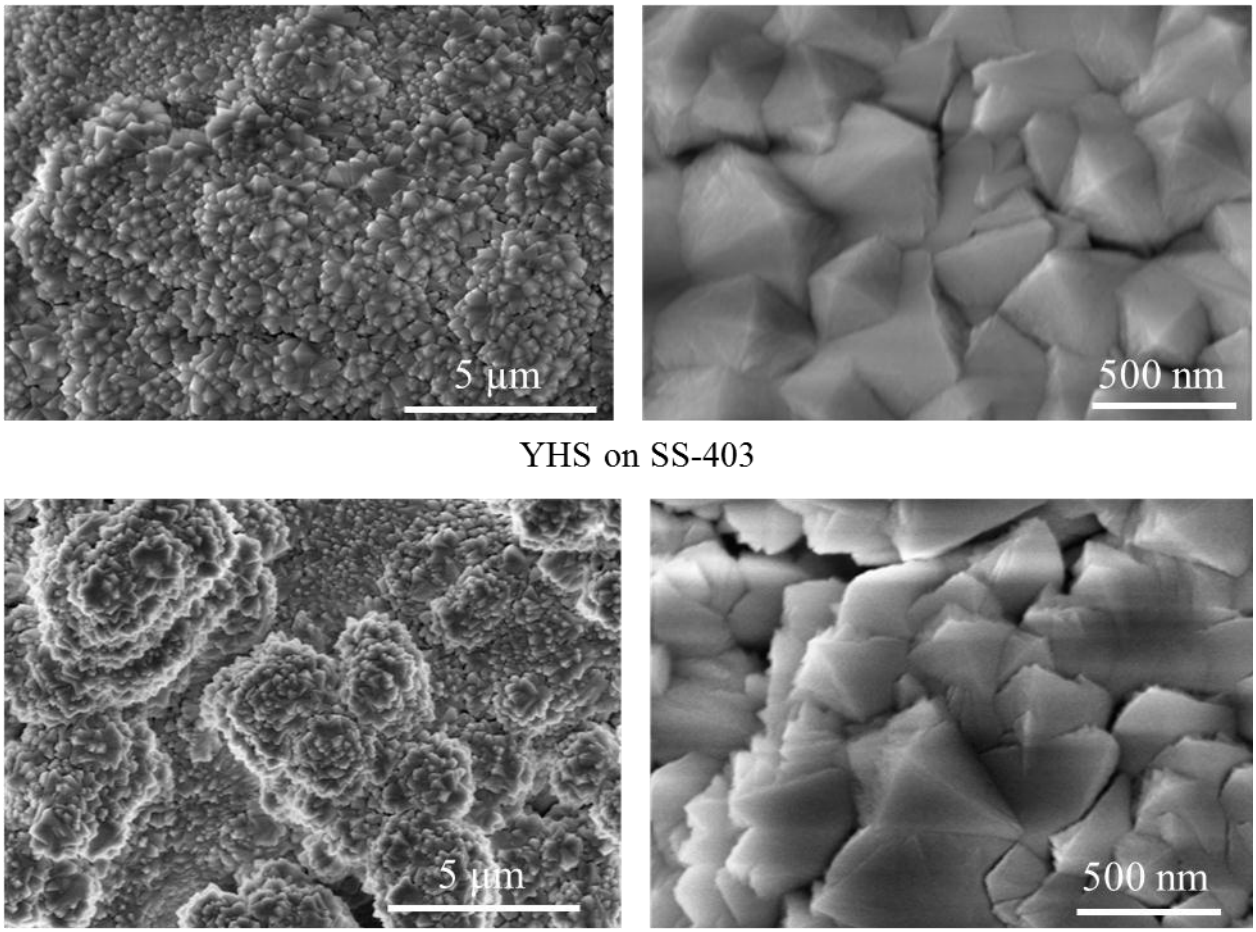

Figure 5.9: Surface morphology of YSH coatings grown on SS-403 and Inconel-738 with bond coat

The surface morphology of the representative YSZH coatings are shown in Figure 5.10, 5.11 and 5.12. High magnification SEM images show the morphology consisting of very well and densely oriented grains in all of the YSHZ coatings grown on SS-403 at 500 ^{0}C (Figure 5.10). However, YSHZ coatings grown at room temperature exhibit the grains, which are smaller in size and not very clear even at high magnifications (Figure 5.11). The morphology looks like a dense cauliflower structure when grown on Inconel-738 (Figure 5.11). It is evident that the ZrO_2 addition induces changes in the morphology of the coatings. Based on the results obtained and

results reported for EB-PVD grown coatings, it appears that thin, elongated triangular shape morphology is the characteristic of the yttria–stabilized hafnia. However, as it is seen in XRD, the deviation of such morphology with progressive addition of zirconia is believed to be due to the distortion as a result of Zr^{+4} ions replacing the Hf^{+4} ions. (71) However when YSHZ is grown as thick coating (as shown in Figure 5.12) the grains tend to grow bigger and arrange in triangular shape and well developed crystallites similar to YSH coatings as shown in Figure 5.9. Therefore, it is evident that the influence of ZrO_2 addition on the surface morphology of YSHZ coatings is not significant when the coating is thick enough (~3 μm) to achieve the complete crystallization.

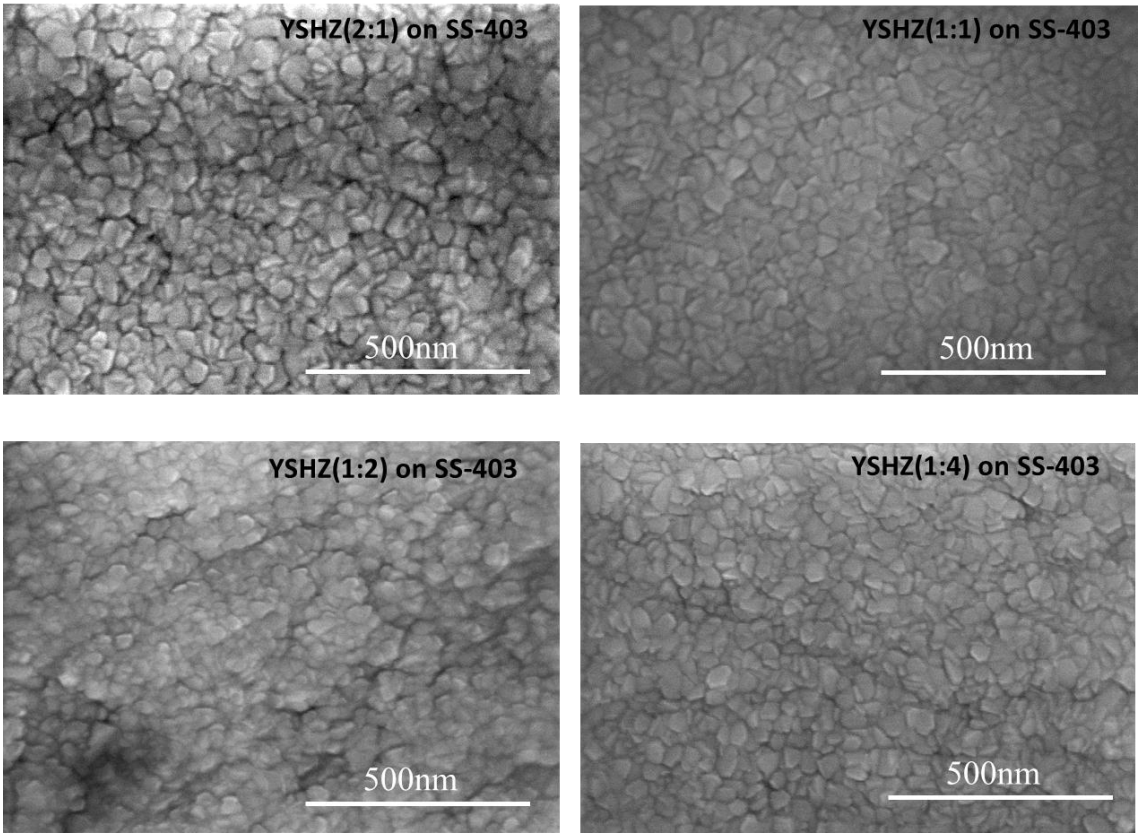

Figure 5.10: Surface morphology of YSHZ coatings grown at 500 ^{0}C on SS-403

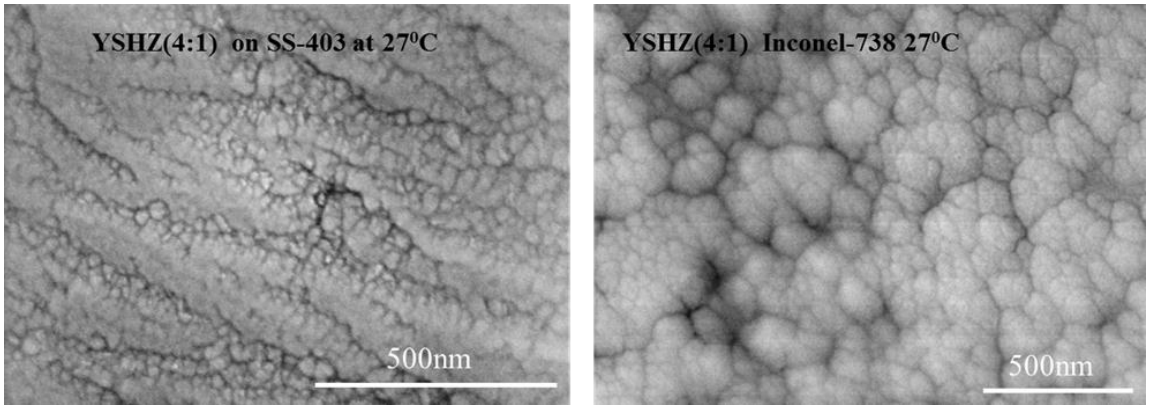

Figure 5.11: Surface morphology of YSHZ coatings grown at 27 ^{0}C

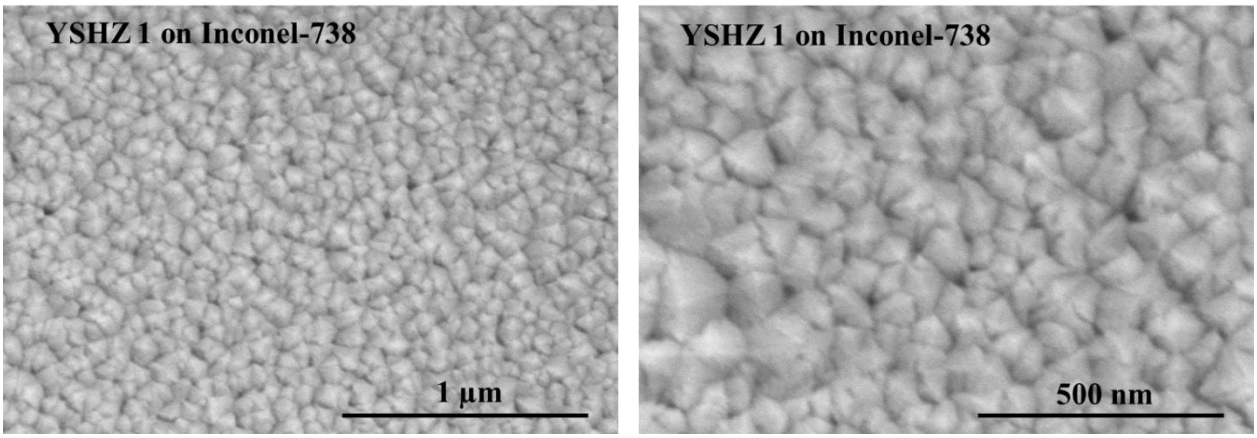

Figure 5.12**:** Surface morphology of YSHZ coatings when grown as thick coatings (~3µm) at 500 ^{0}C

Most remarkable feature noted in this work is the columnar growth of the coatings which is favorable for higher mechanical strength. All the YSHZ and YSH coatings exhibit the columnar structure that is typically observed in these ceramic coatings. A representative of the YSZH coatings interface structure exhibiting the columnar growth is shown in Figure 5.13.

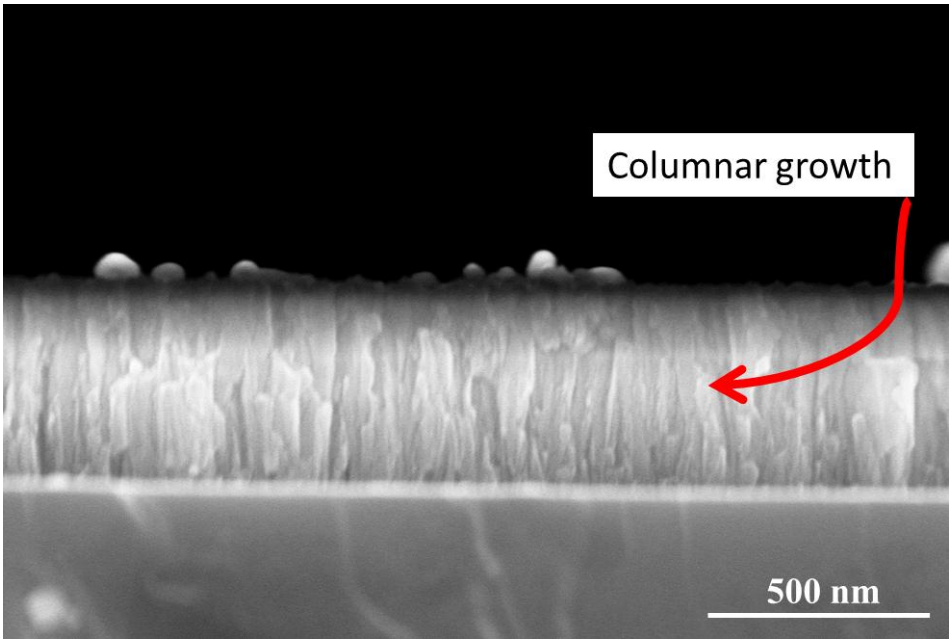

Figure 5.13: Typical columnar growth of YSHZ coatings

5.4 Grain Size

The average grain size variation, determined from XRD data and SEM imaging analysis, with growth temperature is shown in Figure 5.14. It is evident that the grain size increases with increasing growth temperature which can be explained as follows. If temperature is low such that the period of the atomic jump process of adatoms on the substrate surface is very large, the condensed species may stay stuck to the regions where they are landing thus leading to an amorphous material formation in the coatings. The adatoms mobility on the surface increases with increasing temperature, an important thermodynamic parameter in ceramic materials (72; 73). Thus, the crystal structure and well defined grain size with increasing temperature can be attributed to the effect of temperature, which increases the mobility of the surface species. The average crystallite size calculated is in the range from 6 to 20 nm for the crystalline, cubic YSH films grown at the temperature range from RT to 400 ^{0}C.

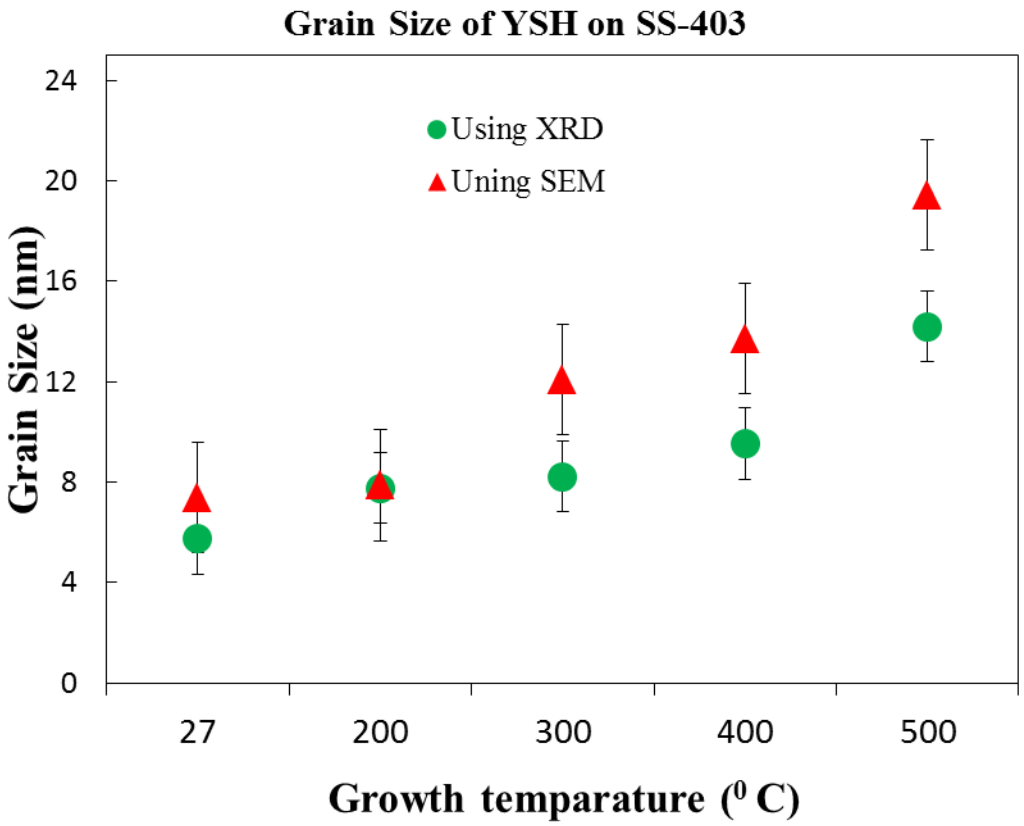

Figure 5.14: The variation of average grain size of YSH coatings with growth temperature

5.5 Composition

It is important to verify that the composition of the coatings is retained similar to the target and compositional stability as a function of growth temperature. The EDS spectrum of the YSH and YSHZ coatings are shown in Figures 5.15 and 5.16, respectively. The EDS curve indicates the X-rays emitted from various elements. The peaks corresponding to Y, Hf, and O atoms present in the sample are as labeled (Figures 5.15 and 5.16). The respective energy positions and the specific X-ray lines from various elements are also indicated in those figures. Intensity of the peaks corresponds to the composition of each element as labeled in Figures 5.15

and 5.16. The absence of any other peaks except from Y, Hf, and O indicates the YSH and YSHZ coatings without any elemental impurities incorporated during chemical processing and/or post-fabrication handling. It was found from the EDS analysis that the same composition of the target used for the deposition retains in the coating when grown using magnetron sputtering indicating the effective transfer of the stoichiometry during deposition of the coating.

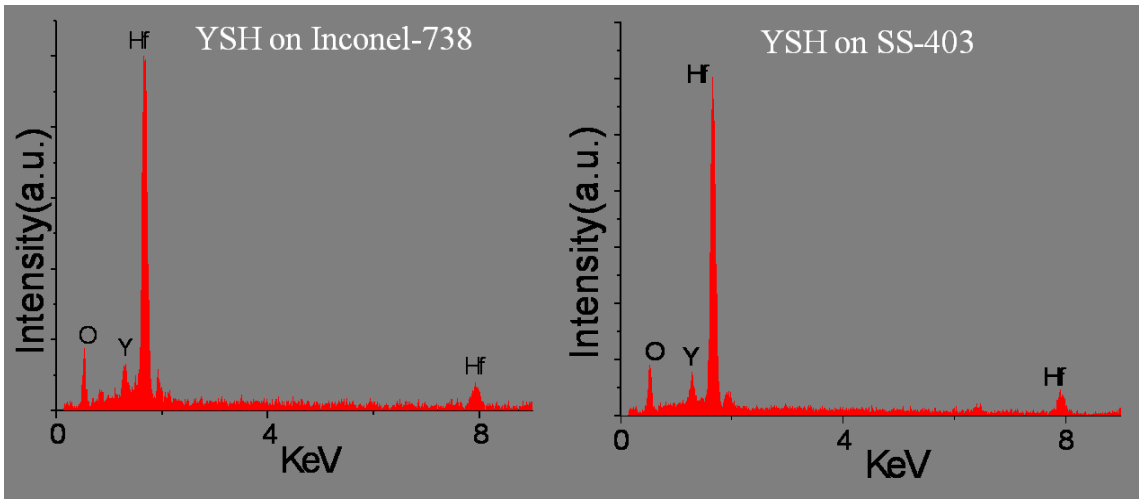

Figure 5.15: EDS spectrum of YSH coatings grown at 500 ^{0}C. The X-ray peaks due to Y, Hf and O atoms and their respective positions are as indicated for the EDS curve.

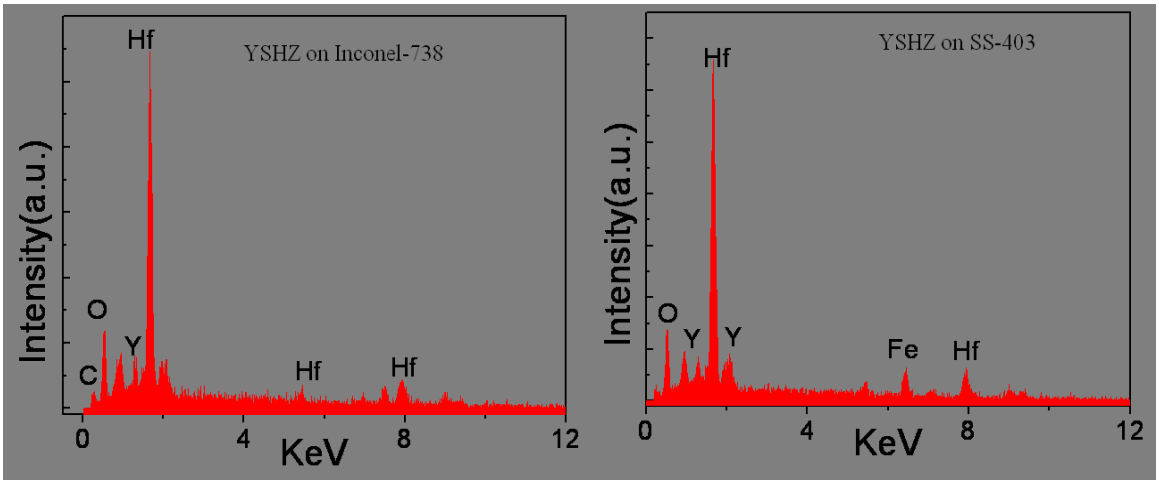

Figure 5.16: EDS spectrum of representative YSHZ coatings grown at 500 ^{0}C.

The composition was also confirmed using XPS analysis. As it is evident from figure 5.17, the atomic concentration of Hf, O and Y is constant for a wide range of sputtering time indicating the uniform composition all over the sample. This was clearly visible in the elemental mapping done by EDS analysis as shown in Figure 5.18.

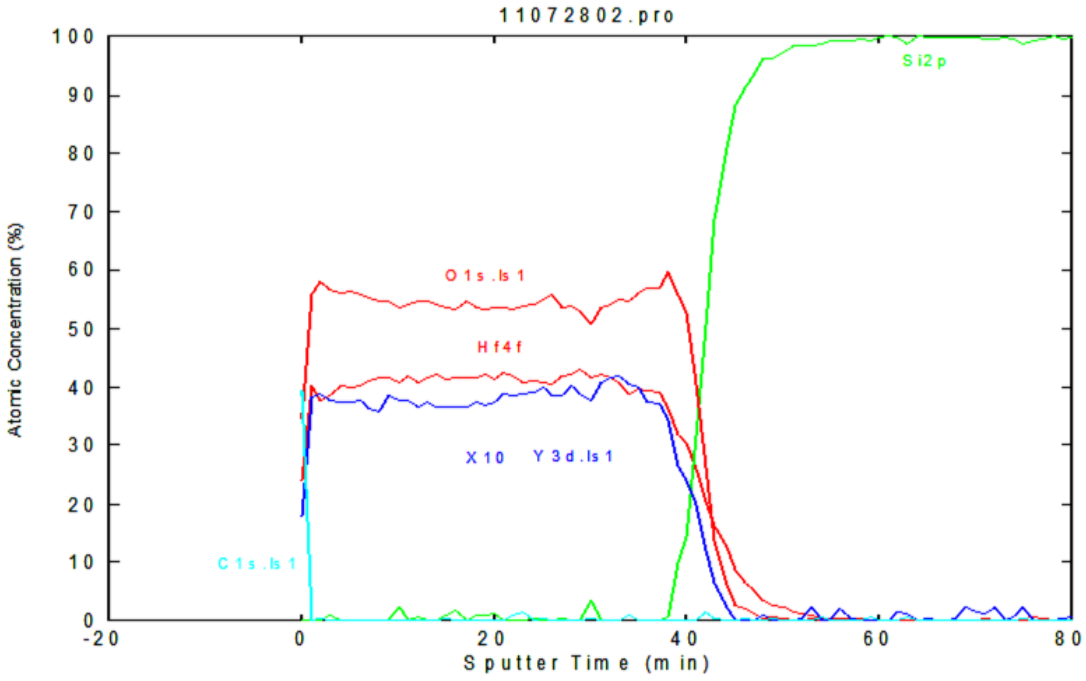

Figure 5.17: XPS data showing the atomic concentration as a function of sputtering time

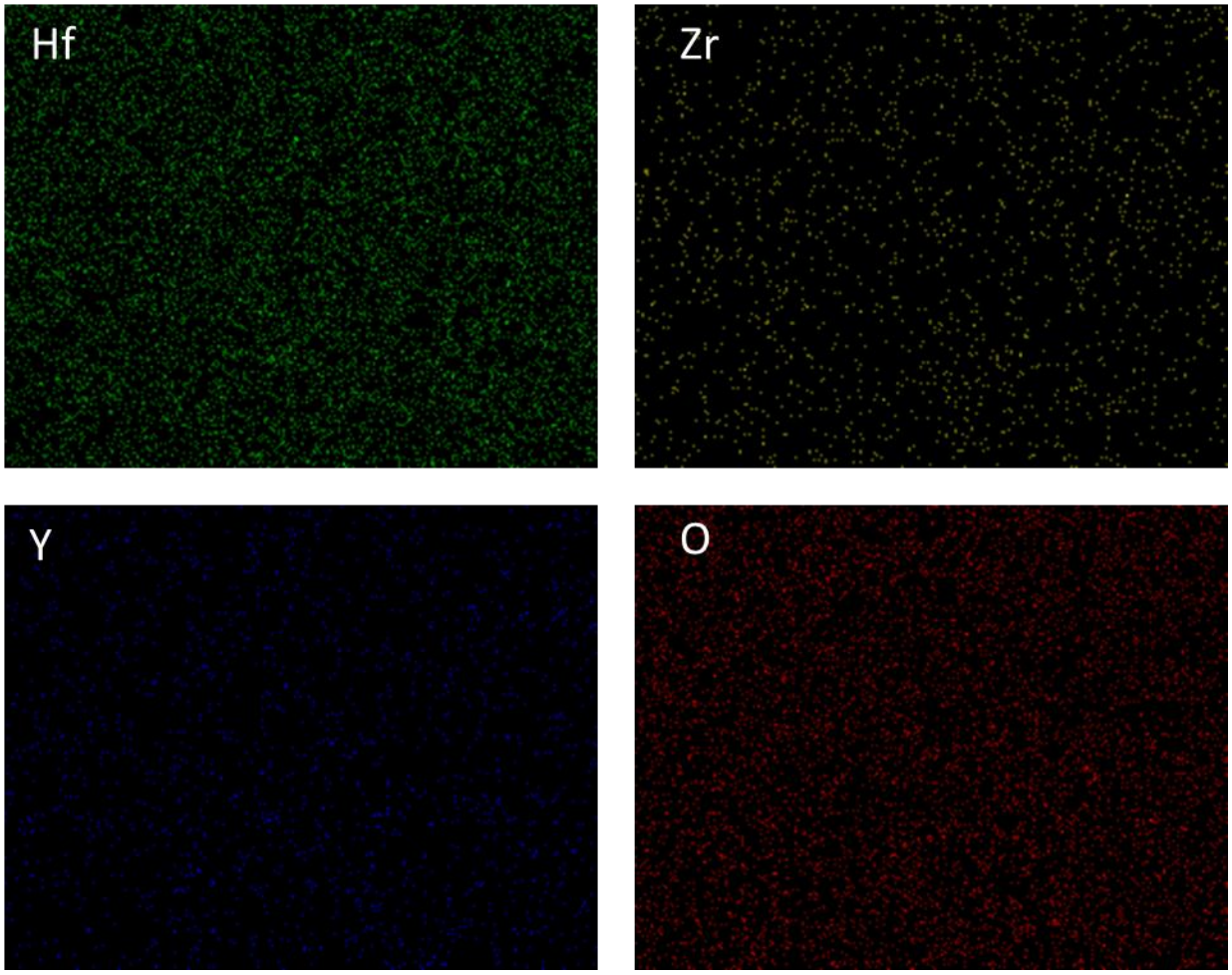

Figure 5.18: Elemental mapping of a representative YSHZ coating showing the uniform distribution of the four elements consisting the YSHZ coating

5.6 Thermal Conductivity

According to the thermal diffusion model (Rosencwaig–Gersho theory), (74) for an optically opaque sample, the expression for PA signal is:

$$\delta P = \frac{\gamma P_0 I_0 (\alpha_g \alpha_s)^{\frac{1}{2}}}{2\pi l_g T_0 k_g f \sinh(l_s \sigma_s)} \exp\left[j\left(\omega t - \frac{\pi}{2}\right)\right] \quad (12)$$

where γ is the air specific heat ratio, P_0, the ambient pressure, T_0, the ambient temperature, I_0, the absorbed light intensity and $\omega = 2\pi f$, where f is the modulation frequency and l_i, k_i and α_s are the length, thermal conductivity and the thermal diffusivity respectively. Here the subscript i (= s, g) denotes sample (s) and gas (g) medium. $\sigma_i = (1 + j)a_i$ is the complex thermal diffusion coefficient of the material where $a_i = (\omega/2\alpha_s)^{1/2}$. If the sample is thermally thick then Eq. (1) reduces to,

$$\delta P \approx \frac{\gamma P_0 I_0 (\alpha_g \alpha_s)^{\frac{1}{2}} \exp -l_s \left(\frac{\pi f}{\alpha_s}\right)^{\frac{1}{2}} / f}{\pi l_g T_0 k_s} X \exp\left[j\left(\omega t - \frac{\pi}{2} - l_s \alpha_s\right)\right] \quad (13)$$

where l_s is the thickness of the sample. From Eq. (13), amplitude varies as:

$$\left(\frac{1}{f}\right) \exp\left[l_s \left(\frac{\pi f}{\alpha_s}\right)^{\frac{1}{2}}\right] \quad (14)$$

the phase varies as

$$-l_s \left(\frac{\pi f}{\alpha_s}\right)^{\frac{1}{2}} \quad (15)$$

Hence, the thermal diffusivity can be measured either from amplitude data or from phase data. The phase shift as a function of the modulation frequency for the YSH coatings is shown in figure 5.19. The thermal conductivity of YSH coatings are found within the range from 0.89 ± 0.03 to 1.3 ± 0.04 W/m-K. Figure 5.20 shows the variation of thermal conductivity with respect to the temperature used for the growth of the YSH coatings. The two important observations that can be derived from thermal conductivity measurements of YSH coatings are as follows. The thermal conductivity of YSH coatings, in general, is lower than that of pure hafnia or bulk YSH is the first. The thermal conductivity slightly increases with increasing growth temperature is the later. The later behavior can be attributed to the increasing grain size with increasing growth

temperature. Thermal diffusion through lattice vibrations in a solid can be affected by: (a) phonon–phonon interactions, (b) imperfections, and (c) grain boundary scattering. The effective grain boundary decreases with increasing grain size leading to a decrease in phonon scattering and, hence, resulting in the observed increase in thermal conductivity. Effective reduction in the thermal conductivity of the YSH coatings grown at RT can be attributed to an amorphous structure, where there exist only smaller particles occasionally. The thermal conductivity increase with increasing grain size has been reported for YSZ. (31; 36) On the other hand, the observed thermal conductivity decrease in yttria stabilized hafnia can be attributed to the addition of yttria to hafnia. Furthermore, thermal conductivity of YSH is much lower than that of pure hafnia. The reason for YSH materials exhibiting lower thermal conductivity than pure hafnia is the introduction of oxygen vacancies. These are structural vacancies in the hafnia crystals due to charge compensation of Y^{+3} ions substituting for Hf^{+4} ions. As a result, phonon scattering from the vacancies decreases effective thermal transport.

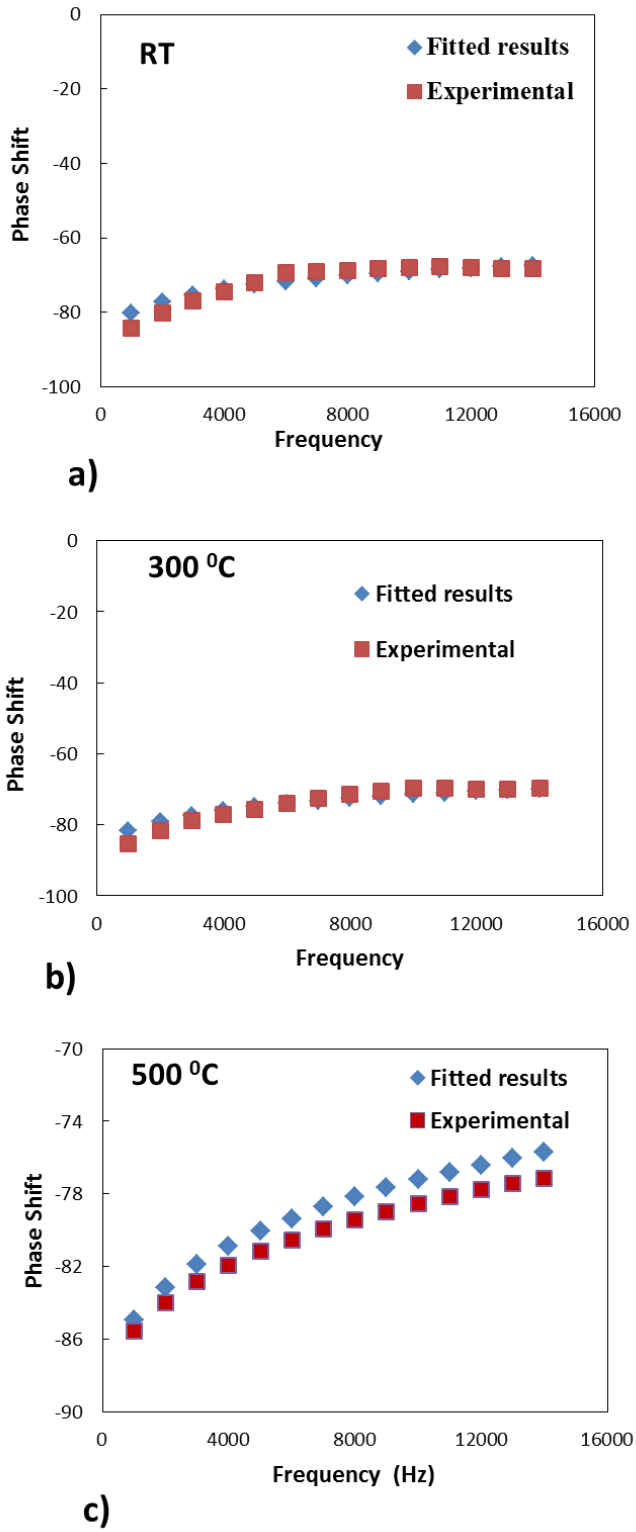

Figure 5.19: Phase shift with respect to modulation frequency for YSH grown at RT (a), 300 ^{0}C (b) and 500 ^{0}C (c).

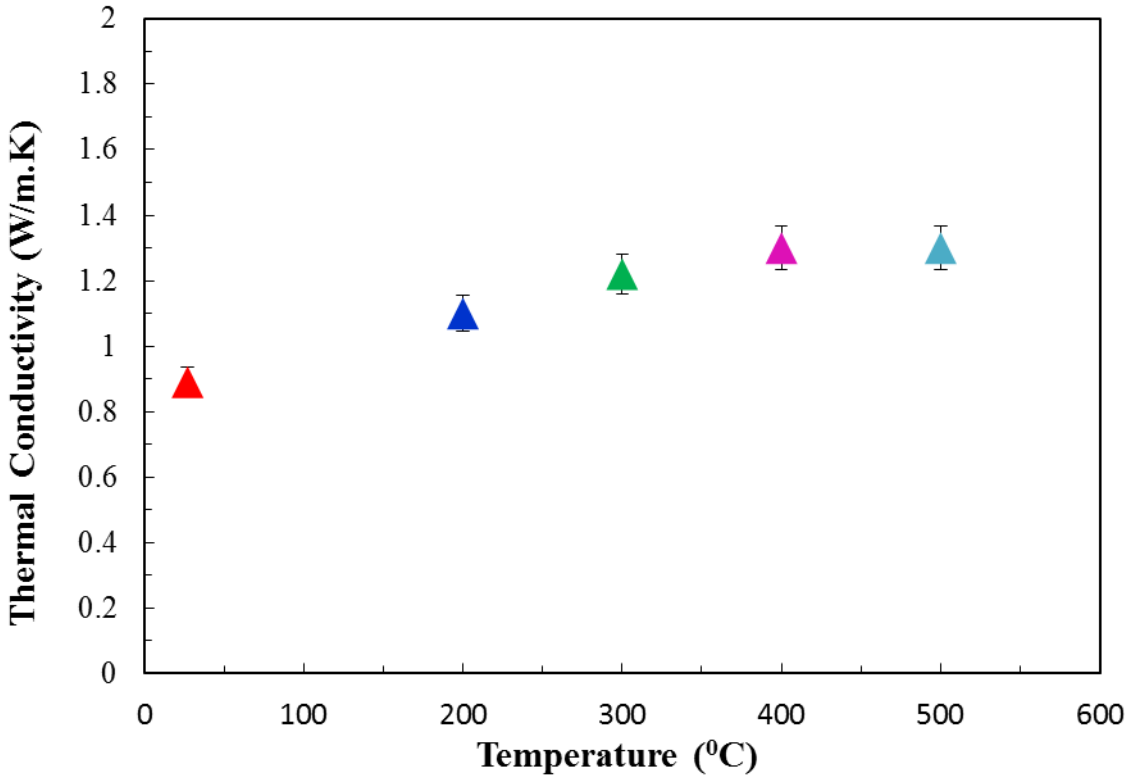

Figure 5.20: Variation of thermal conductivity of YSH coatings with growth temperature.

Thermal conductivity of YSHZ coatings is plotted as a function of composition as shown in Figure 5.21. The compositional dependence of thermal conductivity is evident in the trend shown in Figure 5.21. While thermal conductivity of these YSHZ coatings in general, attains a lower value, the trend seen is an indicative of lower values towards 1:1 ratio of hafnia and zirconia in the coating. However, the thermal conductivity values slightly increases towards the end members where either hafnia or zirconia content is more than the other.

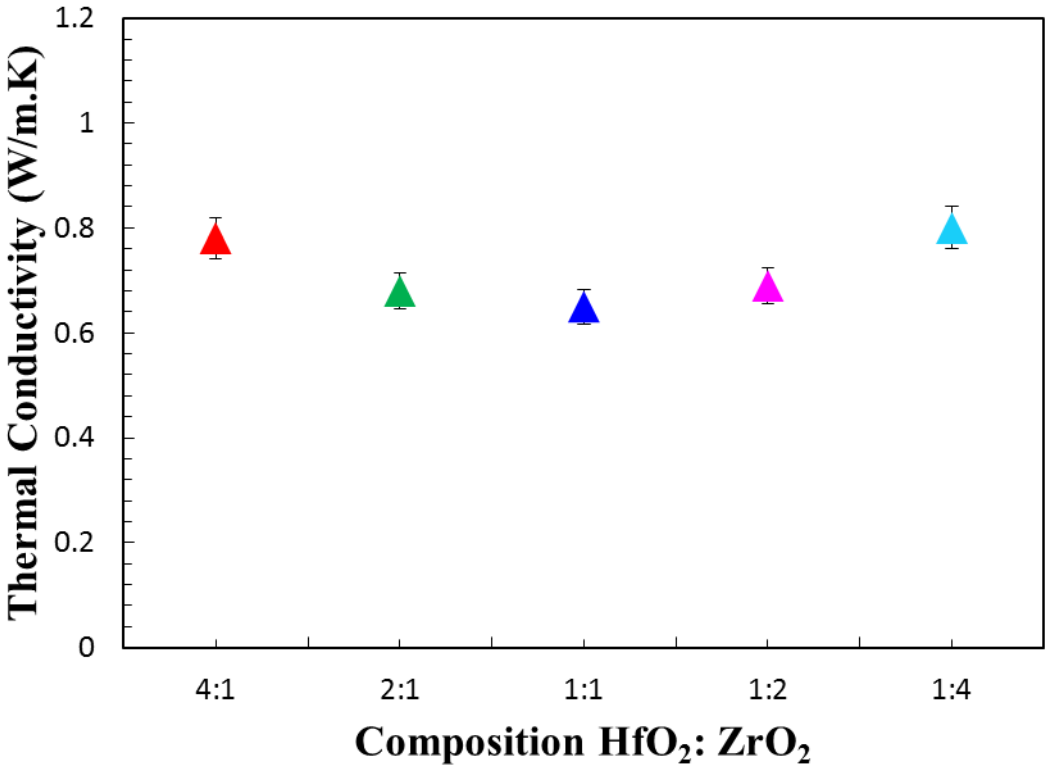

Figure 5.21: Thermal conductivity of YSHZ coatings as function of composition.

5.7 Thermal and Chemical Stability

The enhanced thermal stability of the coatings was found in high temperature XRD measurements. No phase or compositional change was observed in the YSH and YSHZ coatings by exposing to a temperature of 1300 ^{0}C. The stable cubic structure was retained after exposure to 1300 ^{0}C (Figures 5.22 and 5.23). The thermal-induced changes in the chemical composition are probed using the EDS measurements before and after thermal stability experiments (Figures 5.24 and 5.25). EDS indicates that the composition of the coatings is the same before and after thermal stability experiments. Thermo-chemical analysis based on the EDS measurement indicates the coatings' chemical stability to higher temperatures (1300 ^{0}C).

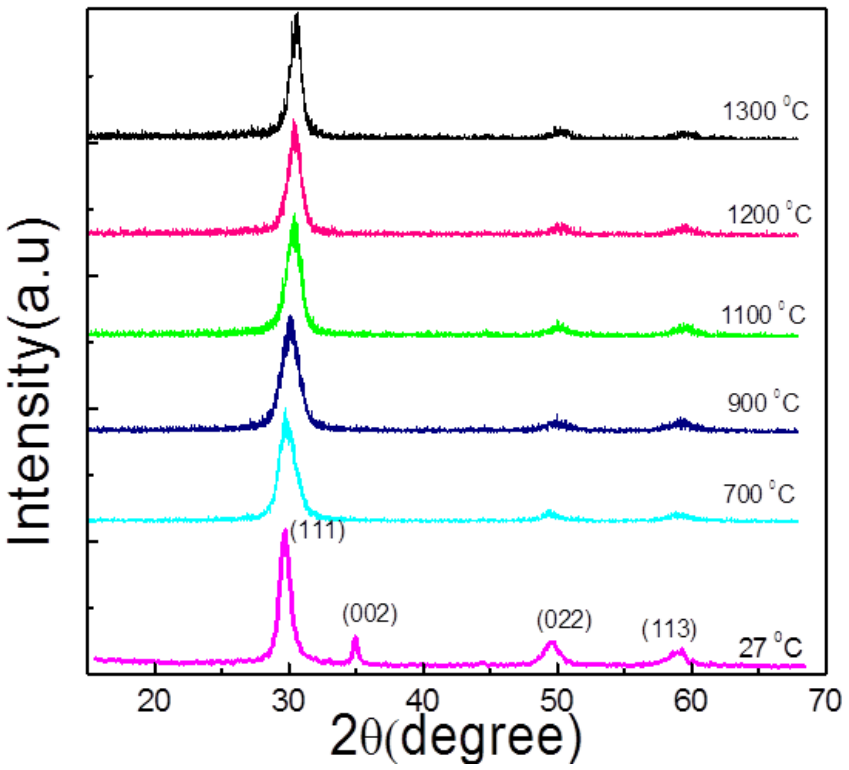

Figure 5.22: High-temperature XRD curves of YSH coatings showing the phase-stability at 1300 ^{0}C

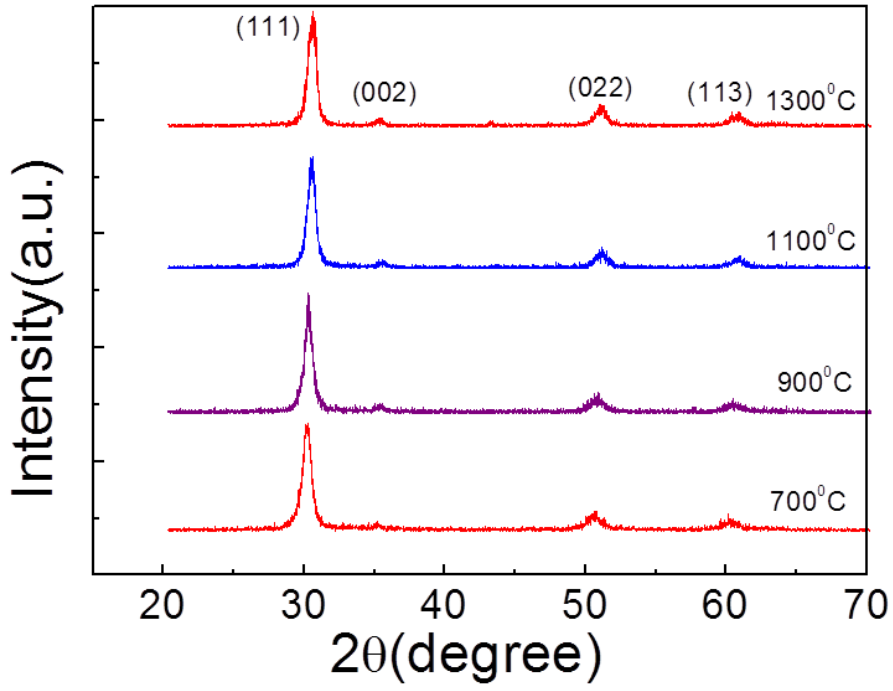

Figure 5.23: High-temperature XRD curves of representative YSHZ (HfO2:ZrO2 = 4:1) coatings showing the phase stability at 1300 ^{0}C

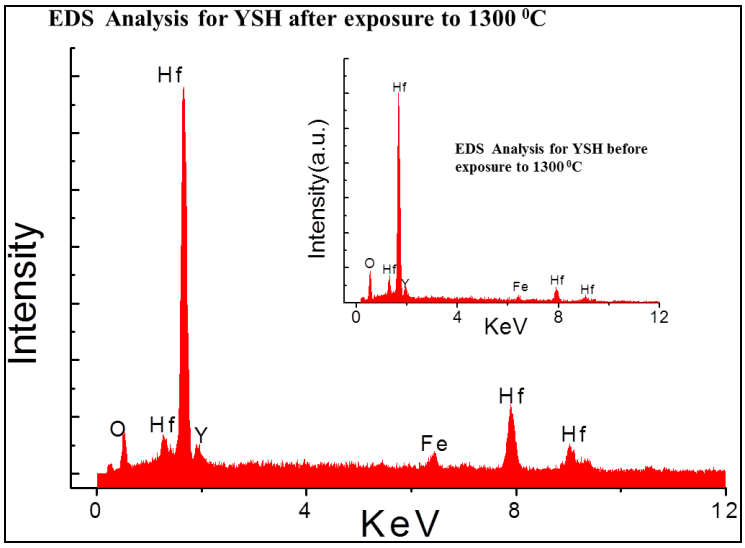

Figure 5.24: EDS curves of YSH coatings before and after thermal treatment at 1300 ^{0}C.

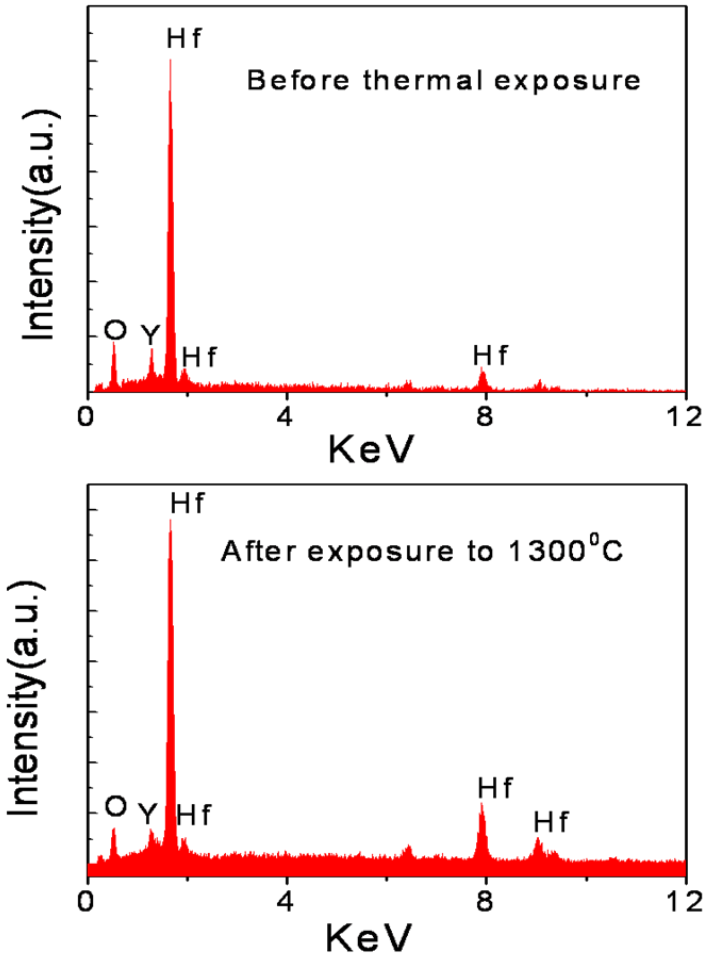

Figure 5.25: EDS curves of representative YSHZ coatings before and after thermal treatment at 1300 ^{0}C

5.8 Mechanical Properties

Figure 5.26 shows the hardness (H), modulus of elasticity (E_s), reduced modulus of elasticity (E_r) and stiffness (S) for YSH and various compositions of YSHZ coatings. Figures5.27 and 5.28 represent the stress versus displacement plot and optical images after nano-indentation respectively for representative samples. It is evident (Figure 5.26) that YSH shows the maximum value in all mechanical strength when compared to all other compositions. The optical images show the damage on the sample surface after nano-indentation (Figure 5.28).

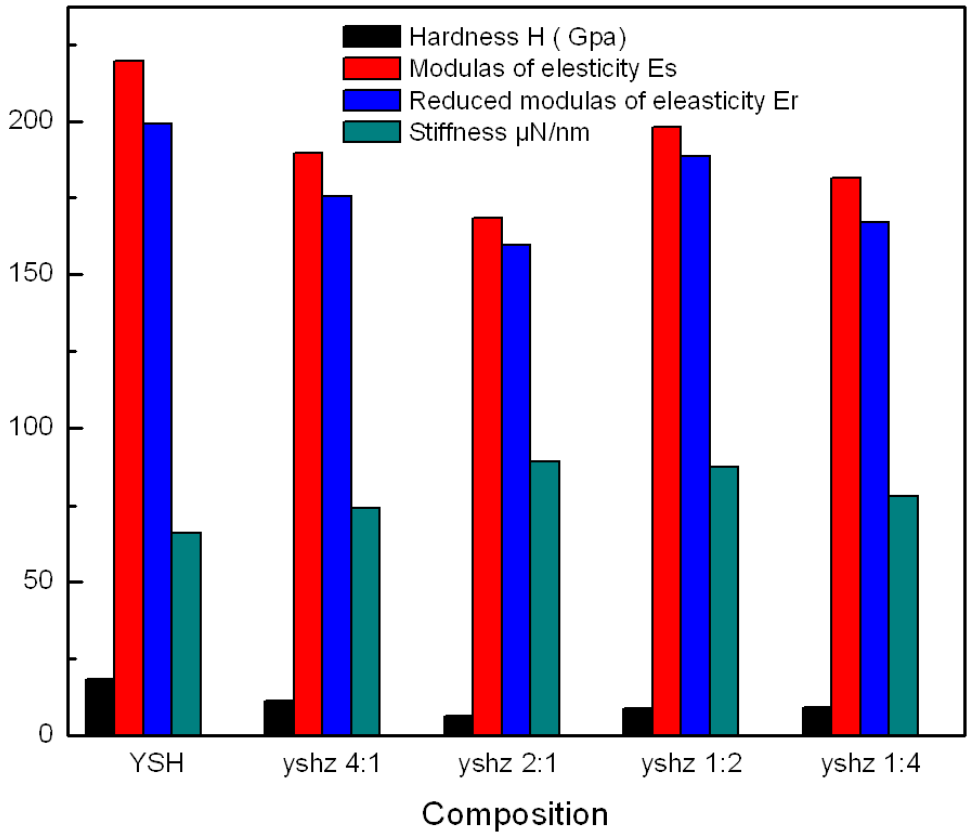

Figure 5.26: Mechanical properties of YSH and YSHZ coatings measured using nano-indentation

One of the most important microstructural parameters that influence the mechanical properties is grain size (41). There is a critical grain size at which the mechanical properties e.g, Young modulus starts decreasing drastically. (41) This critical grain size in pure hafnia is ~2 µm. (41) The grain size of YSH and YSHZ coatings employed for mechanical property evaluation are in the range of ~ 5-20 nm, which is quite low compared to the critical grain size where the mechanical properties degrade in pure hafnia. No drastic change in mechanical properties with the variation of composition in YSHZ may actually be due to the fact the grain size extremely low to induced changes in mechanical characteristics. The interpretation of the mechanical properties could be based on the residual strain energy stemmed from the anisotropy of thermal expansion. If the grains are big enough, micro-cracks are initiated which is responsible for the reduction in mechanical strength. (41) This is not the case in this work as no phase change apart from cubic structure was evident in the operating range of temperature (up to 1300 ^{0}C) which could the origin of significant thermal expansion anisotropy. Since there is no transformation toughening in either YSH or YSHZ coatings, the hardness, Young's modulus and stiffness values are the reflection of the combination of individual material properties of hania, zirconia and yttria. These properties in fully or partially stabilized hafnia or hafnia-zirconia mixed compositions are strongly influenced by the microstructure such as porosity and grain size. As the porosity was not investigated in this work, the quantitative influence of porosity on mechanical properties of YSH and YSHZ is not a matter of discussion here. The high value of hardness and Young's modulus is, perhaps, due to the dense columnar structure which is clearly seen in both YSH and YSHZ. As was reported, the hardness value of fully stabilized hafnia decreases with the content of alloying oxides. (41; 75) This observation is also visible here when zirconia is incorporated in YSH structure; YSHZ exhibits lower hardness values than YSH.

Although the hardness and Young's modulus are very high and close to YSH, there is slight randomness among all the compositions of YSHZ. The randomness is due to the experimental uncertainty resulted due to the columnar structure of both YSH and YSHZ. The mechanical properties were measured using the nano-indentation on the surface of the samples. It is really hard to identify from the top of the surface exactly where the columns are located. If the nano-indenter is placed on the column it will show higher hardness value compared to that obtained if the indenter is placed in between the columns. Figure 5.29 shows the mechanical properties before and after exposure to 1300 ^{0}C used for high temperature XRD. YSH coatings show the similar mechanical properties before after exposure to 1300 ^{0}C indicating the high mechanical stability.

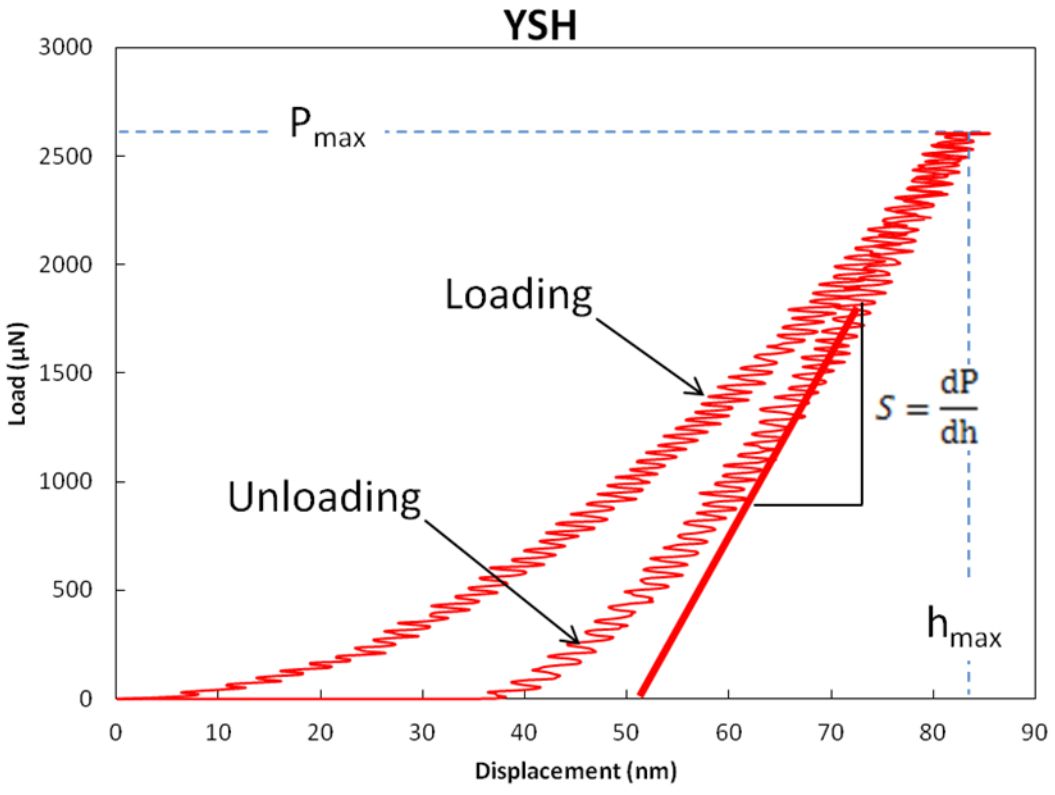

Figure 5.27: Stress versus displacement plot for nano-indentation on YSH coating.

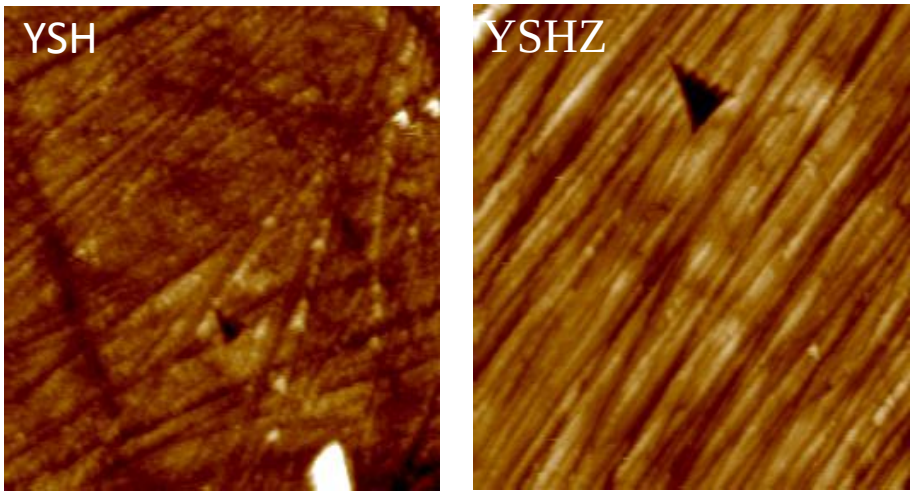

Figure 5.28: Optical images of YSH and YSHZ coatings after nano-indentation

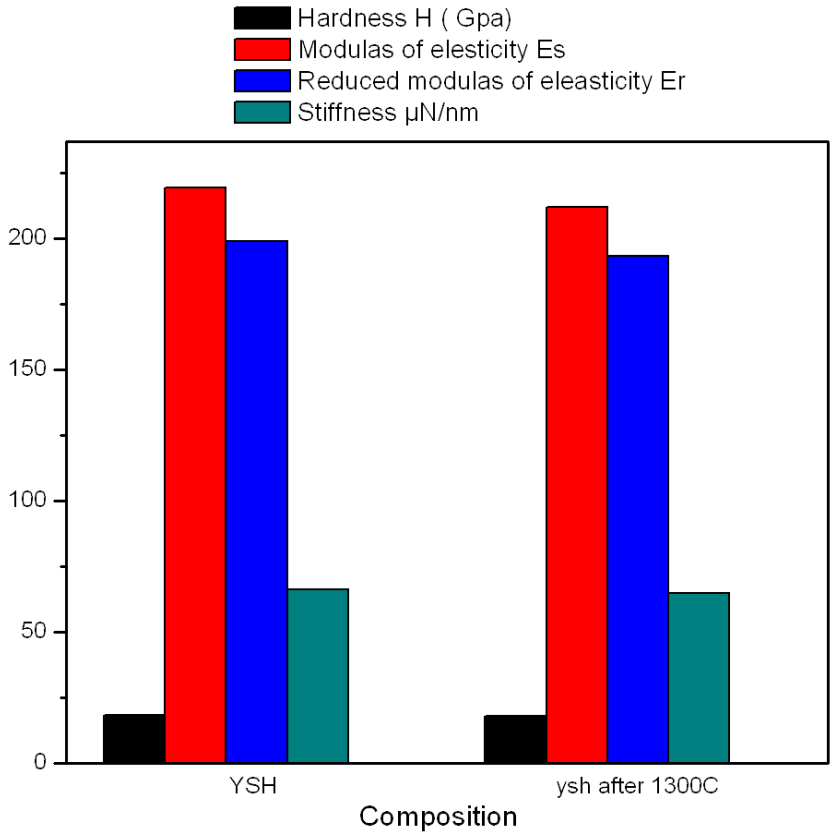

Figure 5.29: Mechanical properties of YSH coatings before and after exposure to 1300 ^{0}C

5.9 Residual Stress

Residual stress analysis was performed using the X-ray diffraction pattern analysis of the coatings as a function tilt angle (ψ). The well-known $\sin^2\psi$ methodology was adopted to calculate the residual stress. (61-62) The variation of d-spacing was measured using the diffraction of Cu-K_α radiation by higher angle planes. X-ray diffraction was carried out at various tilting angle. A linear relation is obtained between the inter-planner spacing and $\sin^2\psi$ values. A plot for YSH grown on Inconel-738 is shown in Figure 5.30. The data presented (Figure 5.30) shows the d-spacing as function of $\sin^2\psi$. Then the residual stress has been calculated using the well-known expression shown in eqn.11. (61) Figure 5.31 shows the residual stresses calculated for YSH and YSHZ coatings. The effect of substrate materials on the residual stress of YSH coatings is also evaluated and presented in Figure 5.31. YSH shows the similar residual stress on both the SS-403 and inconel-738 substrates. The as grown YSH coating shows a compressive residual stress of ~ 2GPa on both the SS-403 and inconel-738 substrates. However, YSHZ shows lower residual stress compared to YSH which is less than 1 GPa. The existing reports as documented in the literature indicates that the residual stress of YSZ coatings ranges from few MPa to close to GPa depending on either processing conditions and coatings' microstructure. (76-81) While residual stress in YSH and YSHZ coatings in the present work is higher compared to traditional YSZ coatings, the behavior may not yield an idealistic behavior or unified model to account for the differences. The obvious reason is that the current set of experiments is designated to understand the stress evolution and behavior at the early stages of growth at the nano-to-submicron-to-micron level or at the interfaces. At such early stages, especially during the first few layers growth of the initial coating, a high level of residual stress

state is expected than normal. Such a behavior is very common in all types PVD growth of coatings. Therefore, in the present case, since the thickness of the coating is not enough to overcome the substrate effect, a higher level of compressive stress is developed during the deposition of the coatings.

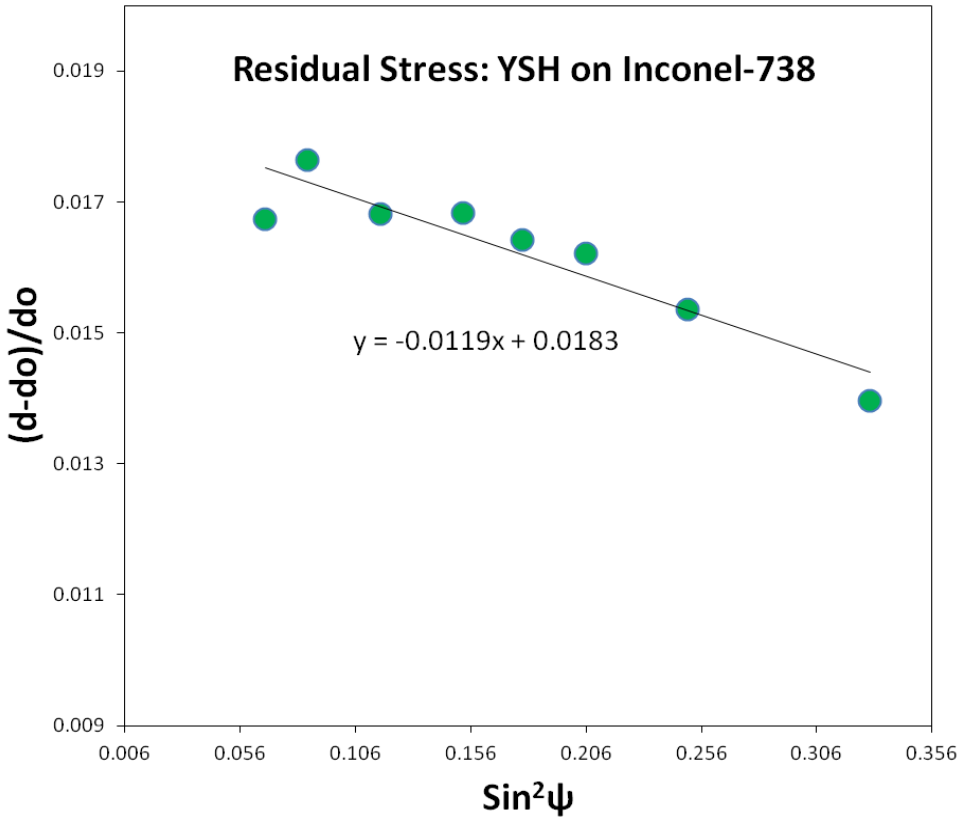

Figure 5.30: d-spacing as a function of $\sin^2\psi$ for YSH sample grown on Inconel-738

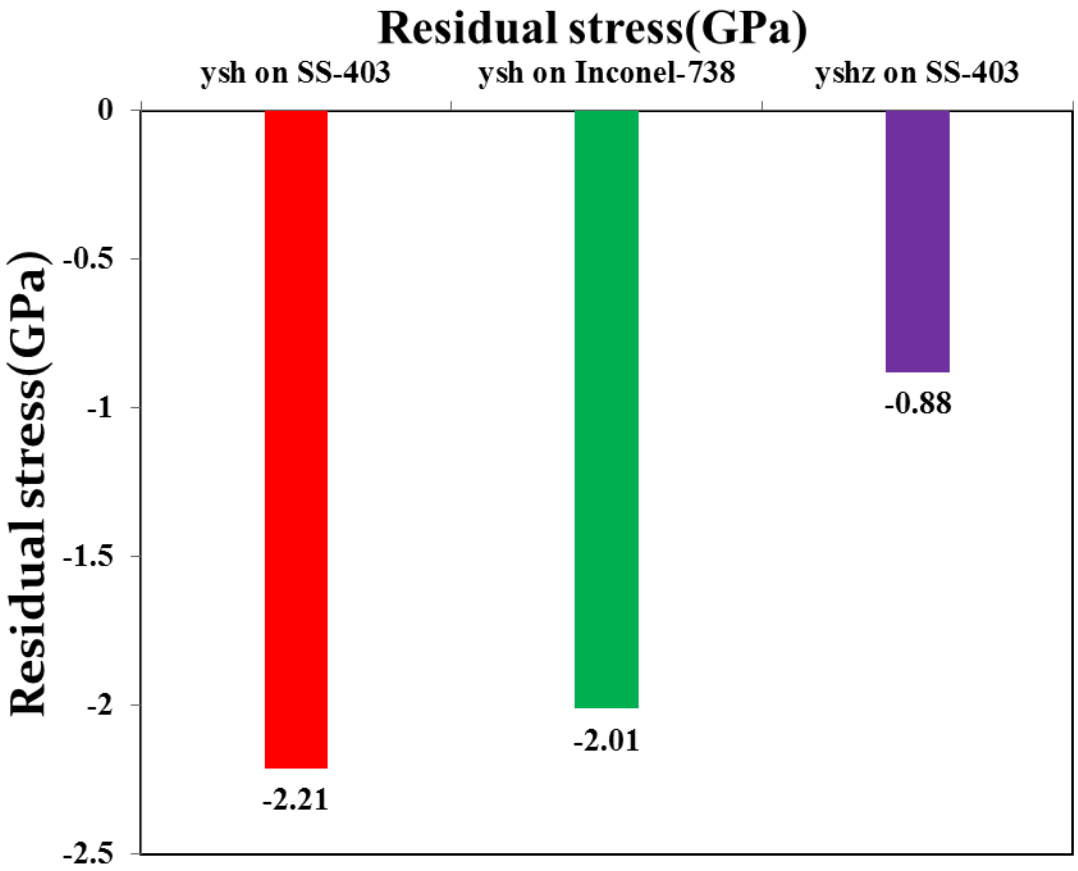

Figure 5.31: Residual stresses calculated for YSH and YSHZ coatings

5.10 Hot Gas Exposure

The hot gas exposure experiment was performed for extended duration (under variable time) at 1100 ^{0}C (the best available temperature without having the coating too close to the flame in the current design) for YSH coatings grown by sputtering. After every span of hot gas exposure, microstructure and morphology were investigated. The details of the operating conditions are as indicated below in Table 5.1.

Table 5.1: Details of hot gas exposure experiments

Conditions	**Composition of the coatings**	
	YSHZ	YSH
Used gases for combustion	CH_4 and air	CH_4 and air
Flow rate of CH_4	19.8 L/min	19.8 L/min
Flow rate of Air	198 L/min	198 L/min
Anticipated composition of the hot gases	CO, CO_2, N_2, O_2 and unburned hydrocarbons	CO, CO_2, N_2, O_2 and unburned hydrocarbons
Temperature of the hot gas	1000 ^{0}C	1000 ^{0}C
Exposure time	1-2 hr	1-2 hr
Angle of impingement	90^0	90^0

Figure 5.32 shows the XRD pattern of YSH coating before and after exposure to hot gases. No significant microstructure change is observed from the XRD patterns. However, the strongest peaks show slight shift in the peak position towards the higher 2θ values with the increase of exposure time to hot gas. The peak shift is indicated by drawing a line through the (111) peaks (Figure 5.32). This peak shift indicates the decrease in interplanar spacing with the increase of exposure time. Little change in orientation is evident after 9 hrs exposure to 1100 ^{0}C.

The coatings show stronger orientation toward (002) direction rather than (111) direction. The material does not show any change from the cubic crystal structure.

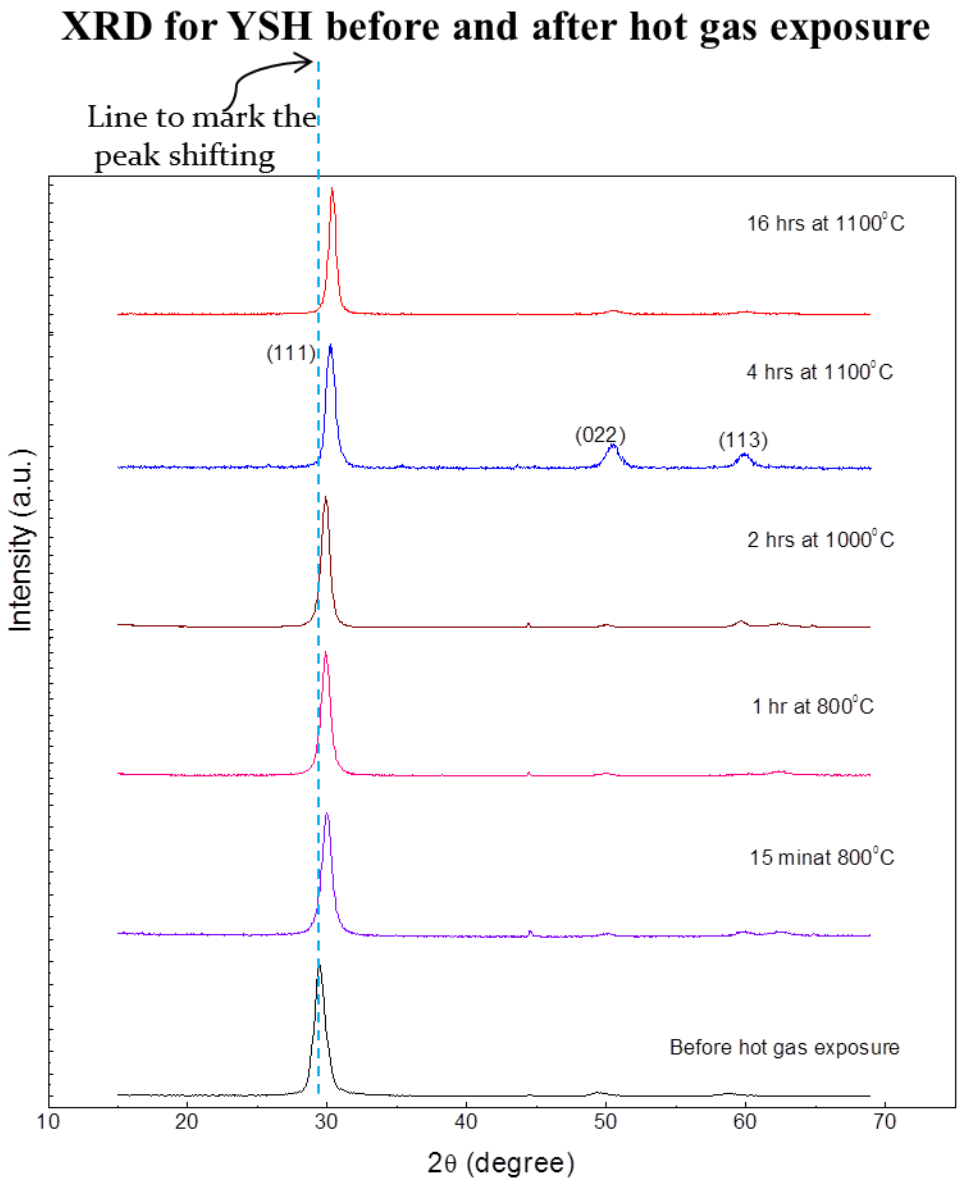

Figure 5.32: XRD patterns of YSH coating before and after exposure to hot gases.

Figure 5.33 shows the surface morphology of YSH coatings after exposure to hot gas. No significant change other than slightly more compactness of the grains is visible from SEM

images when the samples are subjected to hot gases for 9 hrs at 1100 ^{0}C. The morphology after exposure for duration of 16 hrs at 1100 ^{0}C shows slightly different view. It is evident from Figure 5.33(d) that grains are more defined and densely packed together compared to those shown in Figures 5.33(a), 5.33(b) and 5.33(c).

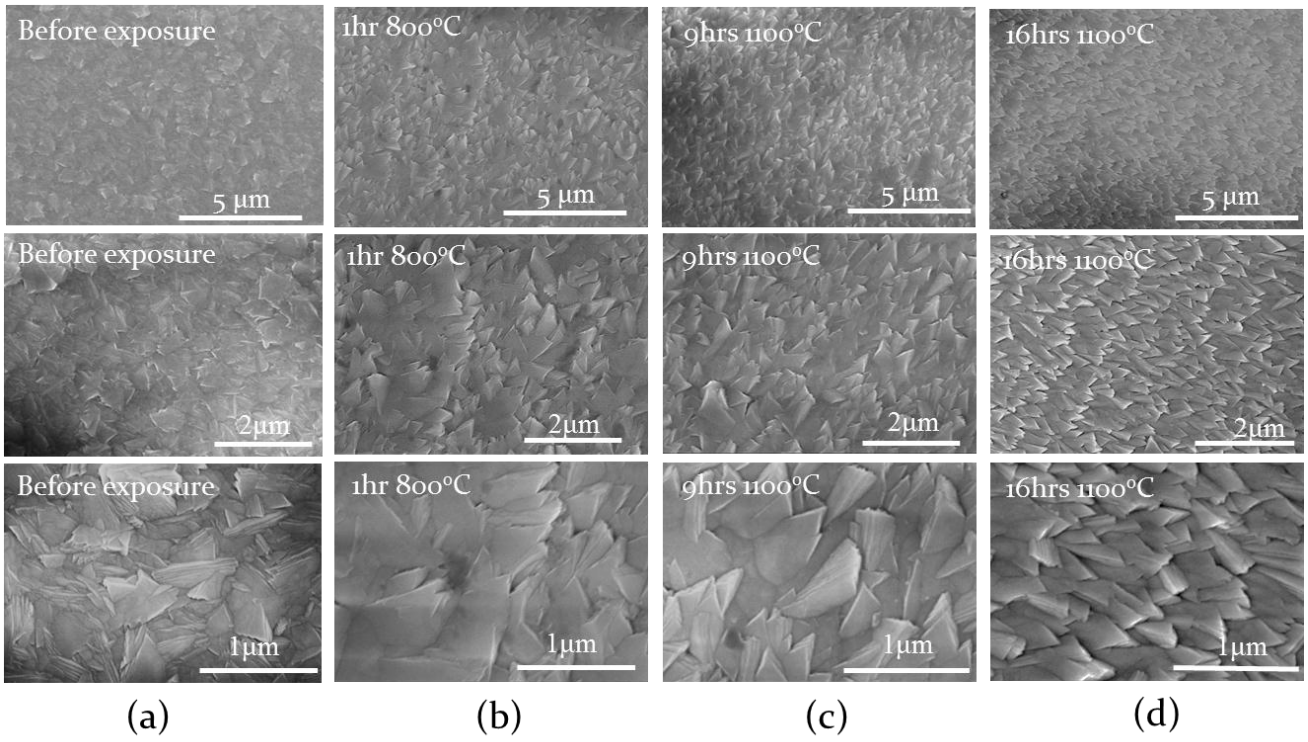

Figure 5.33: SEM images of YSH sample after exposure to hot gases

Residual stress after hot gas exposure:

Analysis of residual stress in the coatings was performed after performing the hot gas exposure experiment for a specific duration of time. Figure 5.34 shows the residual stress for YSH samples before and after exposure to hot gas. It is evident (Figure 5.34) that as grown YSH

coating holds high residual stress within the coating. It is interesting to note that the coating shows a significant relaxation of residual stress through the exposure to hot gas within the short period of time, like 2 hours. However, the coating gains the stress back after exposure to hot gas at higher temperature for longer duration of time. Comparing the residual stress developed in the as grown coating, coating under hot gas for 9 hrs and the coating under hot gas for 16 hrs exhibit more or less similar compressive stress, which is as high as around 2 GPa.

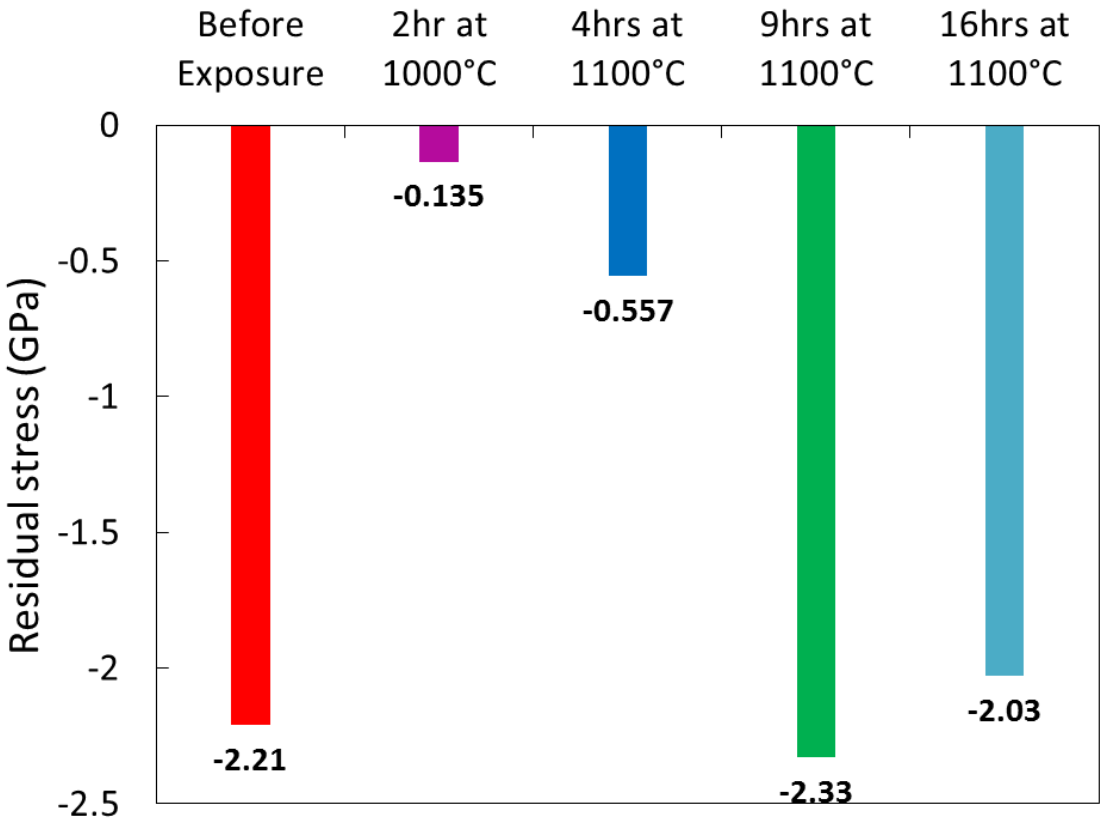

Figure 5.34: Residual stress in YSH coatings before and after exposure to hot gases

5.11 Thermal Oxidation

The results of thermal oxidation measurements indicate that the material exhibits a good

resistance against oxidation at higher temperatures. The weight of the samples increases with the increase of exposure time but the extent of increment is low which is ~0.002 gm/cm^2 after 5 hours and ~0.025 gm/cm^2 after 160 hrs for the YSH samples grown by either sputtering or EBPVD deposition. The samples grown by EBPVD shows little more oxidation compared to that by sputtering. The samples grown on alumina do not show any further oxidation after getting the weight increase of 0.009 gm/cm^2. The samples grown on SS-403 without bond coat indicate the highest amount of weight increase which is due to the oxidation of substrate material. The weight increase against the exposure time is shown in Figure 5.35, a) weight increase per unit area against exposure time and b) total weight increase against exposure time.

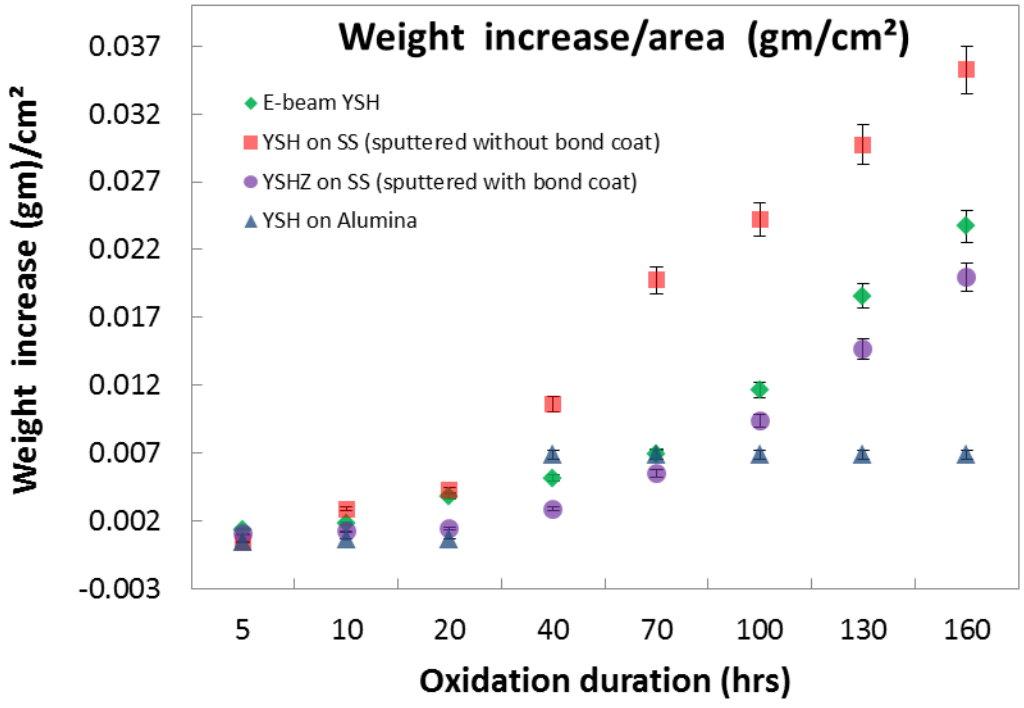

a)

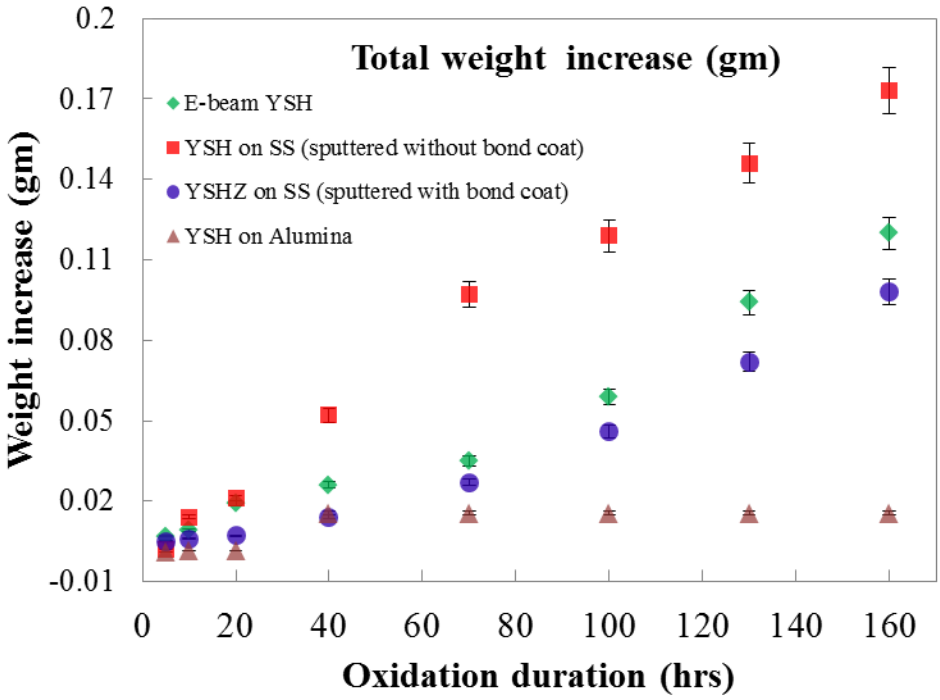

b)

Figure 5.35: The weight increase against the exposure time a) weight increase per unit area against exposure time and b) total weight increase against exposure time

5.12 Interface of Bond Coat and Top Coat

The interface at the bond coat - top coat was investigated using crosssectional SEM and TEM imaging analysis. No interface between bond coat and topcoat was visible when YSH coating was grown on inconel-738. Figure 5.36 shows the crosssectional images of YSH coating on bond coat (NiCoCrAlY) examined by SEM. A careful examination of SEM images shown in Figure 5.36 indicates that the interface morphology in one image is different from another. This is because of the fact that the crosssectional sample was prepared after deposition of the top coat. After the deposition of YSH on Inconel-738, the sample was mounted vertically in the epoxy

polymer. After mounting, the top surface was polished in order to get the smooth surface on one edge. The area where the top coat was polished perfectly looks like plane (top right picture) and the area where the polishing could not touch the topcoat or made little abrasion looks like the picture place in bottom right position of Figure 5.36. The top coat might be delaminated in some areas (eg, bottom left image) because of the uneven abrasion during the polishing. The images are presented for a comparison purpose. Figure 5.37 shows the cross-sectional images of YSH coating on alumina substrate obtained by TEM.

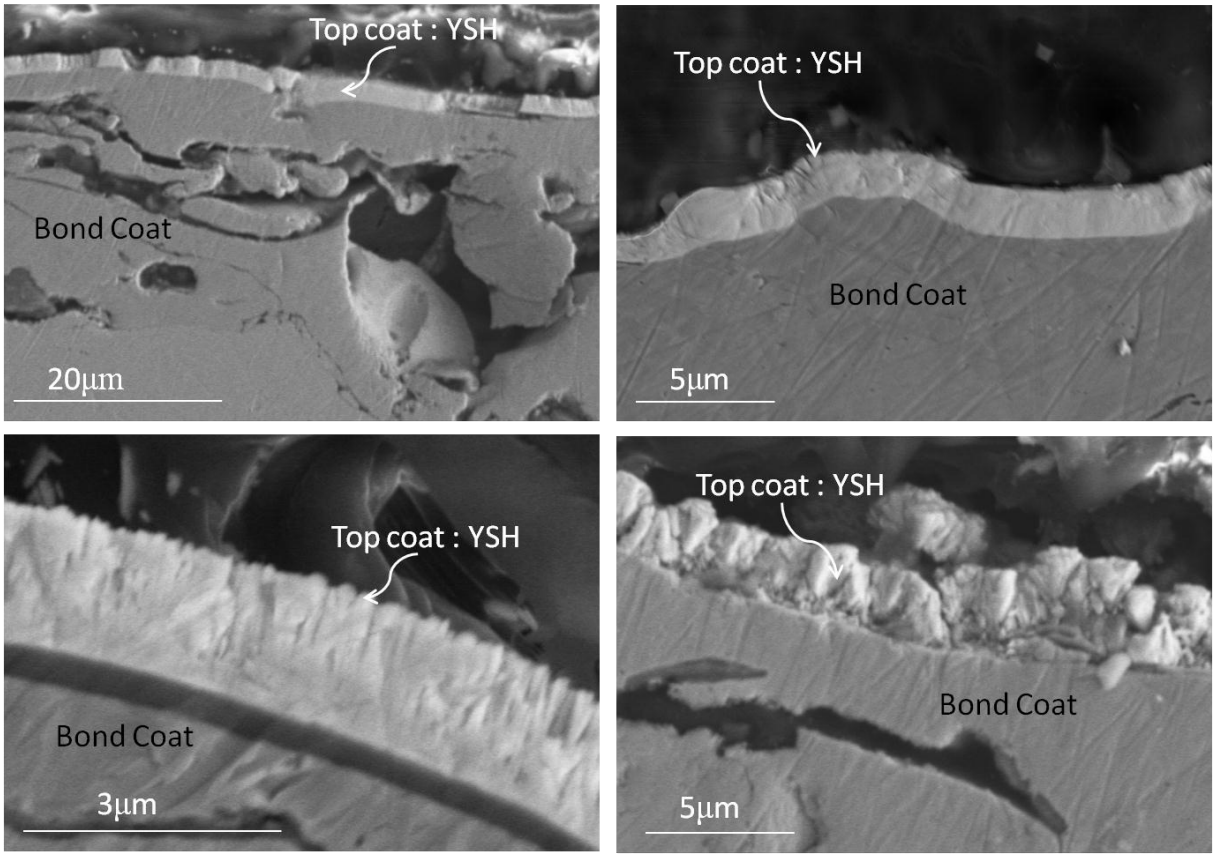

Figure 5.36: Crosssectional images of YSH coatings on bond coat (NiCoCrAlY) obtained by SEM.

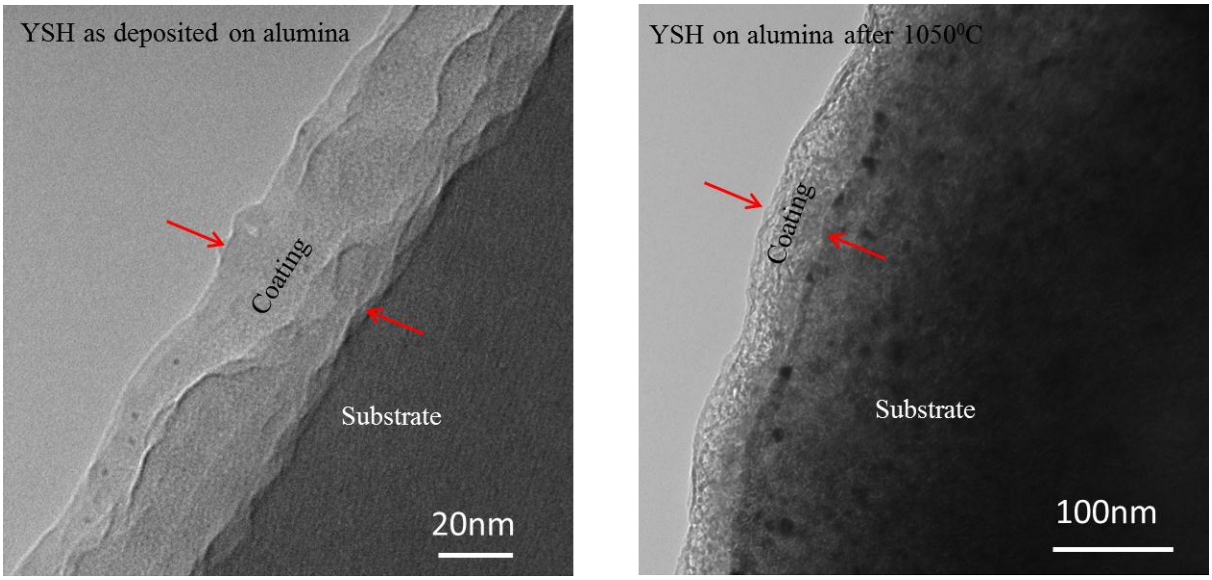

Figure 5.37: Crosssectional images of YSH coating on alumina substrate obtained by TEM

5.13 Crystallography of Coatings Grown by EBPVD

YSH and YSHZ coatings were grown using EBPVD. The crystallographic analysis was made using XRD. Figure 5.38 shows the XRD pattern of YSH and YSHZ coatings grown by EB system. The XRD pattern shows that both the YSH and YSHZ coatings crystallize in cubic structure. YSH coatings grown on either SS-403 or Inconel-738 exhibit the preferred orientation along (111) direction of cubic hafnia. YSHZ coatings with the hafnia four time more than zirconia indicates a strong orientation towards (200) direction of cubic hafnia. On the other hand, when zirconia content is four times more than hafnia the peaks are less intense and the interaction from the bond coat is dominant. This is might be because of insufficient thickness of the coating to avoid the prominent interaction from the bond coat. Since the coatings were grown on bond coat some of the phases from the bond coat are also visible in the XRD pattern as shown in Figure 5.38. These phases have been confirmed by performing the XRD on the bare bond coat

samples. YSH coatings were grown with sufficient thickness to avoid the interaction from bond coat as a result of which no phase from bond coat is visible in XRD pattern of YSH coatings.

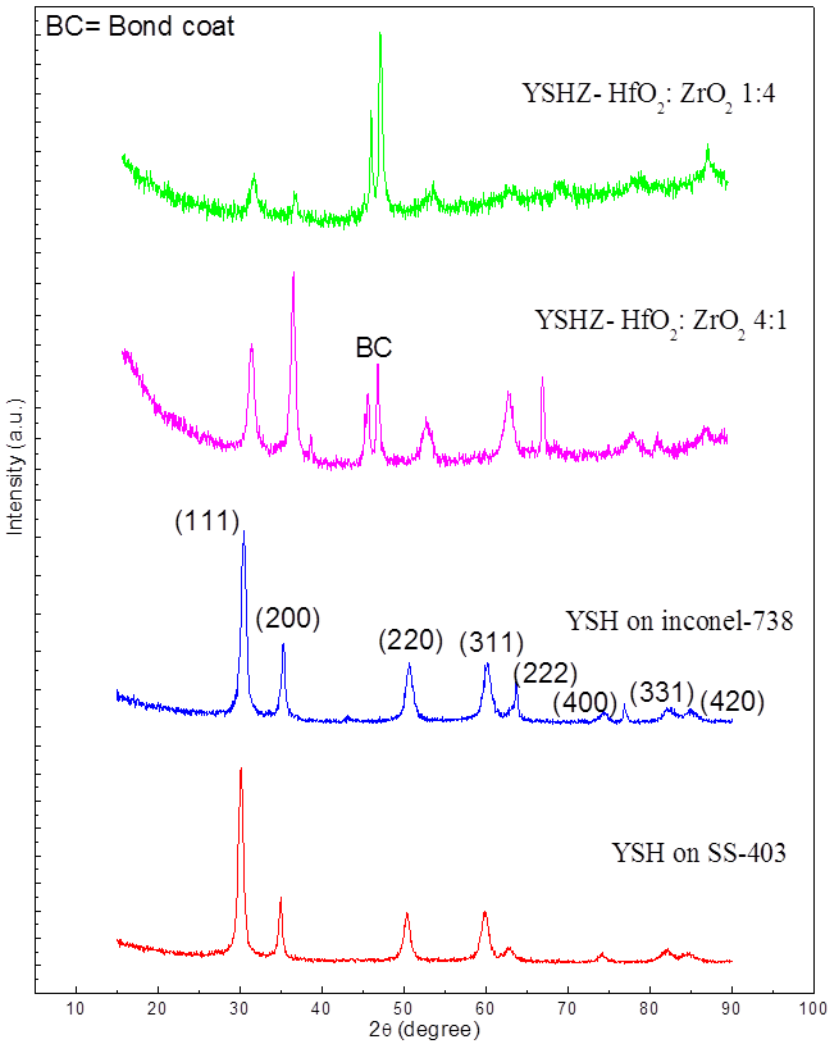

Figure 5.38: XRD pattern of YSH and YSHZ coatings grown by EBPVD system

5.14 Morphology of Coatings Grown by EBPVD

Figure 5.39 shows the SEM images for YSH coatings grown by EBPVD on SS-403 (upper panel) and Inconel-738(lower panel). It is evident from Figure 5.39 that YSH grows vertically and agglomerates in big particles as shown in the left panel of Figure 5.39. Images

were obtained developed at high magnification scanning to see the grain orientation. However, no grain structure was visible on the surface even after annealing at 500 ^{0}C for 6 hrs as shown in the right panel of Figure 5.39.

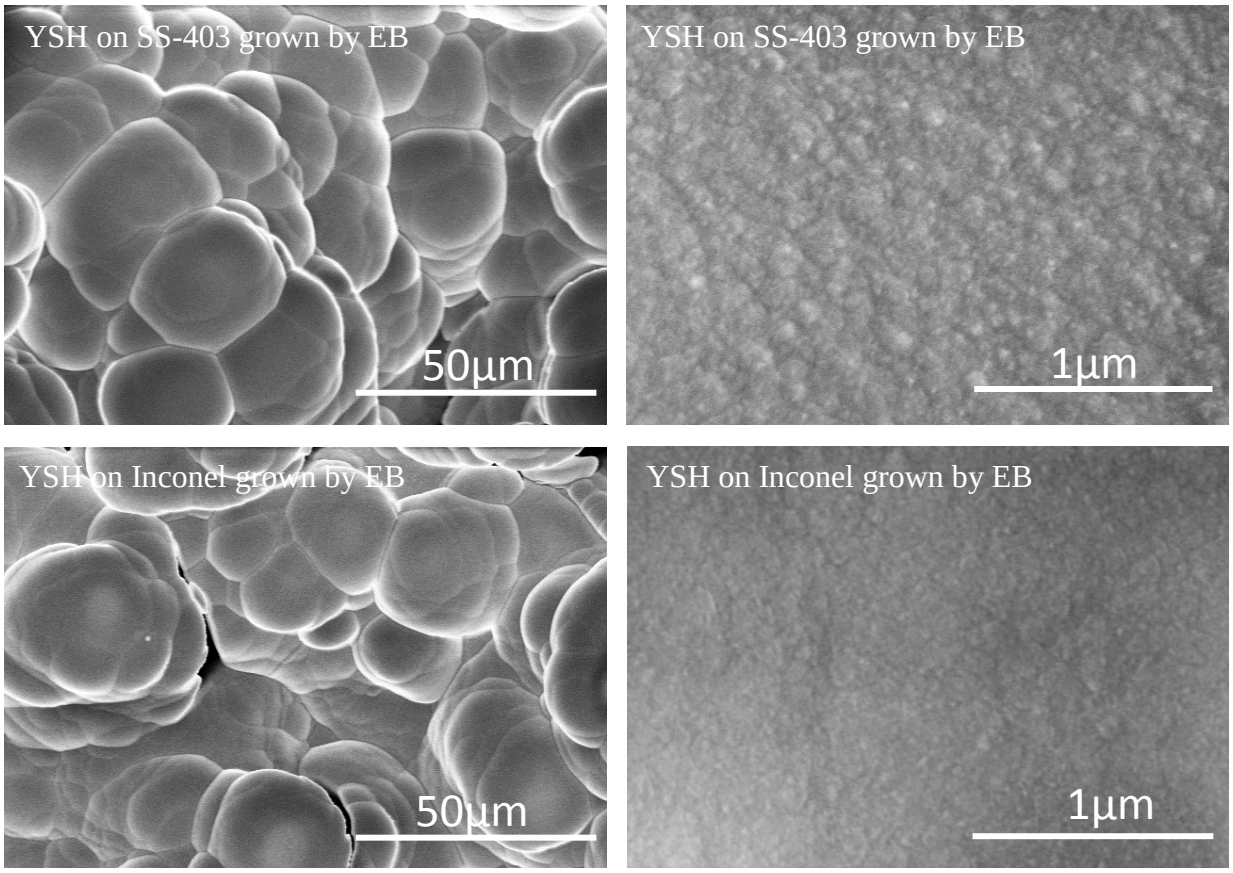

Figure 5.39: Surface morphology of YSH coatings grown by EBPVD

Figure 5.40 shows the SEM images of YSHZ-1 and YSHZ-4 coatings grown by EBPVD. It is evident from Figure 5.40 that both the YSHZ-1 and YSHZ-4 agglomerate in big particles which are condensed in dense structure. The average particle size is slightly higher when hafnia is more than zirconia compared to that when hafnia is less than zirconia as shown in Figure 5.40. It is also evident from the high magnification images (Figure 5.40; right panel) that the small

grains are randomly distributed within the bigger particles. However, the grains are not clearly visible from theses SEM images.

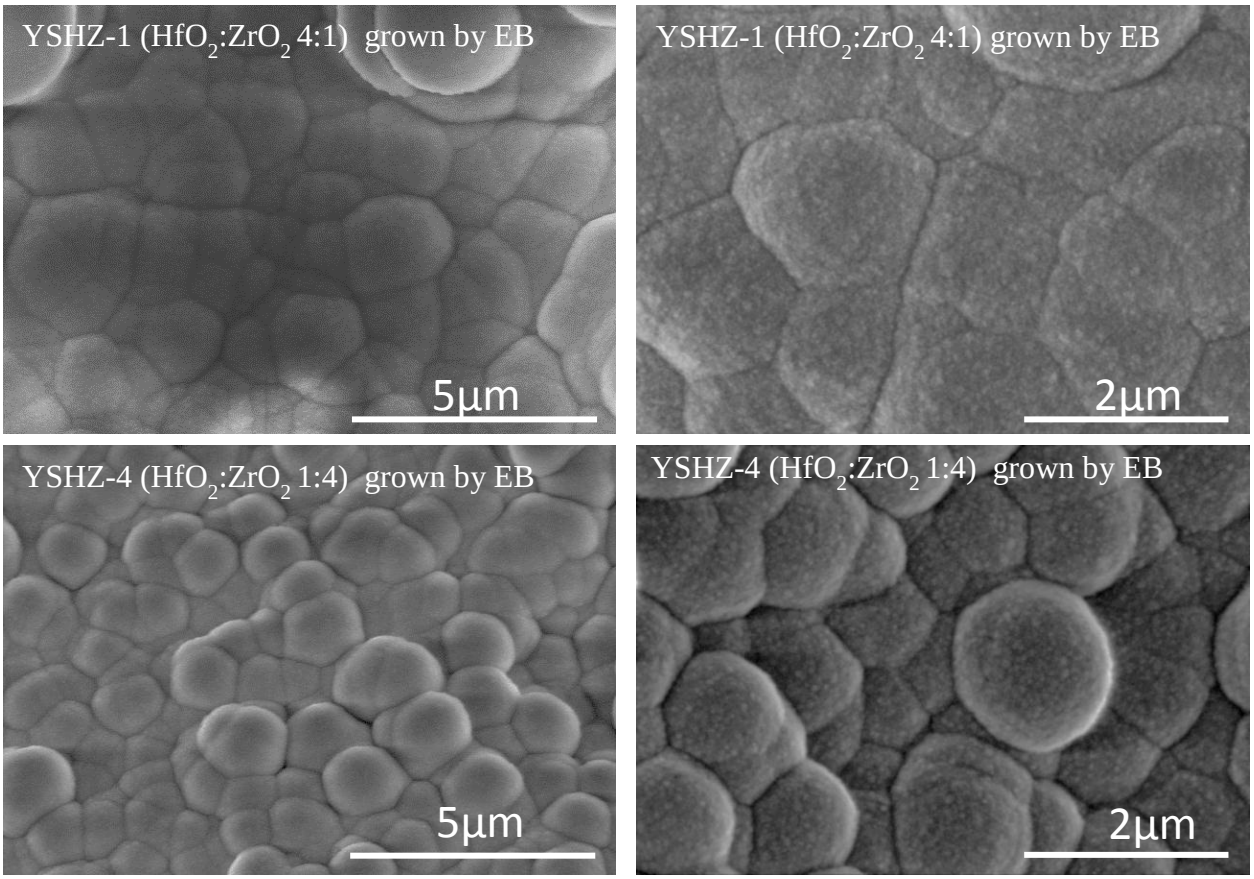

Figure 5.40: Surface morphology of YSHZ-1 and YSHZ-4 coatings grown by EBPVD

Very clear and well developed grains were visible when the samples were annealed at 900 ^{0}C for 15 hrs as shown in Figure 5.41. Because of the high temperature, the grains are looked to be attached to each other.

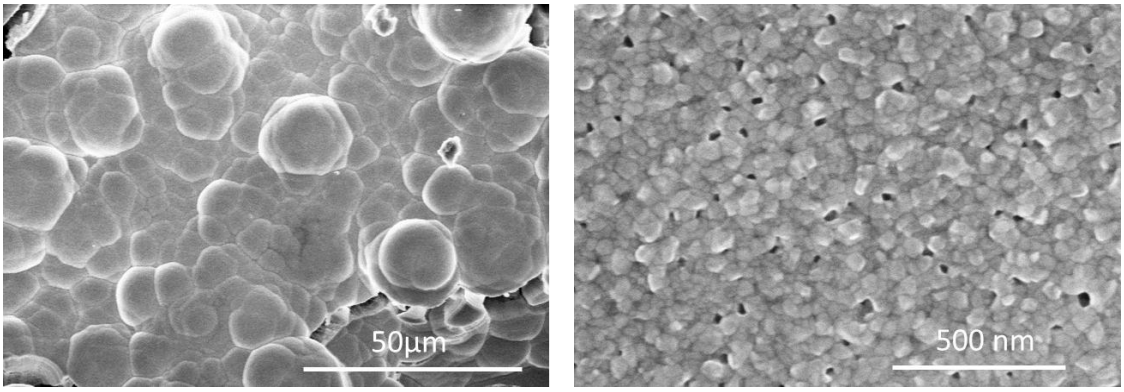

Figure 5.41: Surface morphology of YSH coatings grown by EBPVD after annealing at 900 ^{0}C for 15 hrs

Figure 5.42 shows the cross-sectional SEM images of YSHZ samples grown by EBPVD as a representative sample. The crosssectional image shows the columnar growth of the YSHZ coatings when grown by EBPVD technique. The upper portion of the columns looks wide and stressed compared to the bottom part. Coatings were grown on Si without bond coat in order to get the cross-sectional images. It was evident from the sample surface that the coating was partially delaminated from the substrate was bent upward. That's why the upper portion of the coating looks like stressed.

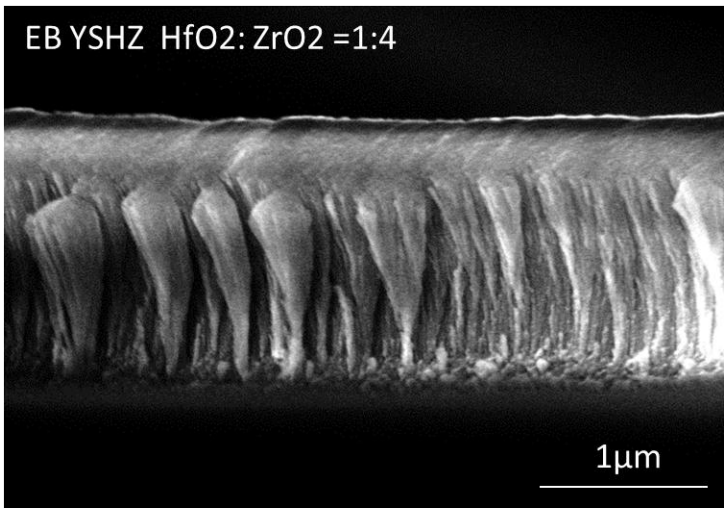

Figure 5.42: The crosssectional SEM images of YSHZ samples grown on Si substrate by EB deposition

Chapter 6: Summary and Conclusions

Yttria stabilized hafnia (YSH) and yttria stabilized hafnia-zirconia (YSHZ) coatings crystallizes in cubic structure when grown by PVD methods. PVD method shows the columnar growth and dense structure of YSH and YSHZ TBCs. Cubic crystal structure retains after exposure of the coatings to a temperature of 1300 ^{0}C. Chemical composition and morphology also were maintained well in the coatings after exposure to 1300 ^{0}C. Mechanical strength is higher in YSH than YSHZ with high residual stress in both type of coatings. YSH coatings exhibit lower thermal conductivity compared to YSZ and HfO_2. Annealing slightly increases the thermal conductivity YSH coatings show high stability in hot gas environment. YSH and YSHZ coatings grown by EB-PVD system crystallize in cubic structure when grown on either on SS-403 or Inconel-738. YSH grows vertically and agglomerates in bigger particles when coatings are grown at room temperature. Very clear and well developed grains are visible when the samples are annealed at 900 ^{0}C for 15hrs.

References

1. S. Bose and J. DeMasi-Marcin, Thermal barrier coating experience in gas turbine engines at Pratt & Whitney, Journal of Thermal Spray Technology, 6, (1), 1997, 99-104.

2. W. P. Parks, E. E. Hoffman, W. Y. Lee and I. G. Wright, Thermal barrier coatings issues in advanced land-based gas turbines, Journal of Thermal Spray Technology, 6(2), 1997, 187-192.

3. W. P. Danesi and M. Semchyshen "The future in superalloys," in The superalloys. ed. C. T. Sims and W. C. Hagel, J. Wiley & Sons, New York, 1972, 565-574.

4. R. L. Jones, Experiences in seeking stabilizers for zirconia having hot corrosion-resistance and high temperature tetragonal (t') stability, Naval Research Laboratory, 1996, NRL/MR/6170-96-7841.

5. S. Bose and J. DeMasi-Marcin, "Thermal barrier coating experience in gas turbine engine at pratt & whitney" in Proceedings of Thermal Barrier Coating Workshop, NASA Conference Publication 3312, NASA Lewis Research Center, Cleveland, OH, 1995, 63-77.

6. N. P. Padture, M. Gell and E. H. Jordan, Thermal barrier coatings for gas-turbine engine applications, Science. 296 (2002) 280-284.

7. P. G. Klemens and M. Gell, Thermal conductivity of thermal barrier coatings, Materials Science and Engineering A, 245(2), 1998, 143–149.

8. S. Paul, Ceramic thermal barrier coatings: porosity, pore architecture and properties, Lambert Academic Publishing GmbH & Co. KG, Saarbrucken, Germany, 2011.

9. K. Matsumoto, Y. Itoh and T. Kameda, EB-PVD process and thermal properties of hafnia-based thermal barrier coating, Science and Technology of Advanced Materials, 4, 2003, 153-158.

10. B. Saeedi, A. Sabour and A. M. Khoddami, Study of microstructure and thermal shock behavior of two types of thermal barrier coatings, Materials and Corrosion, 60 (9), 2009, 695-703.

11. D. R. Clarke and S. R. Phillpot, Thermal barrier coating materials, Materials Today, 8, 2005, 22-29.

12. R. A. Miller, J. L. Smialek and R. G. Garlick, "Phase stability in plasma-sprayed partially stabilized zirconia-yttria" in Advances in Ceramics, Vol. 3, ed. A. H. Heuer and L. W. Hobbs, American Ceramic Society Inc., Ohio, 1981.

13. P. K. Schelling and S. R. Phillpot, Mechanism of thermal transport in zirconia and yttria-stabilized zirconia by molecular-dynamics simulation, Journal of American Ceramic Society, 84 (12), 2001, 2997-3007.

14. A. H. Heuer and L. W. Hobbs, "Science and technology of zirconia" in Advances in Ceramics, Vol. 3, American Ceramic Society, Columbus, OH, 1981, 241-251.

15. D. Zhu and R. A. Miller, Thermal conductivity and sintering behavior of advanced thermal barrier coatings, 26th Annual International Conference on Advanced Ceramics and Composites, 2002, American Ceramics Society, Cocoa Beach, Florida.

16. S. Raghavan, H. Wang, R.B. Dinwiddie, W. D. Porter and M. J. Mayo, The effect of grain size, porosity and yttria content on the thermal conductivity of nanocrystalline zirconia, 39 (8), 1998, 1119–1125.

17. H. Yang, G. Bai, L. J. Thompson and J. A. Eastman, Interfacial thermal resistance in nanocrystalline yttria stabilized zirconia, Acta Materialia 50, 2002, 2309–2317.

18. W. A. Nelson and R. M. Orenstein, TBC experience in land-based gas turbines, Journal of Thermal Spray Technology, 6(2), 1997, 176–180.

19. L. L. Shaw, D. Goberman, R. Ren, M. Gell, S. Jiang, Y. Wang, T. D. Xiao and P. R. Strutt, The dependency of microstructure and properties of nanostructured coatings on plasma spray conditions, Surface and Coatings Technology, 130 (1), 2000, 1–8.

20. M. Gell, E. H. Jordan, Y. H. Sohn, D. Goberman, L. Shaw, and T. D. Xiao, Development and implementation of plasma sprayed nanostructured ceramic coatings, Surface and Coatings Technology, 146-147, 2001, 48-54.

21. R. S. Lima, A. Kucuk and C. C. Berndt, Evaluation of micro hardness and elastic modulus of thermally sprayed nanostructured zirconia coatings, Surface and Coatings Technology, 135, 2001, 166-172.

22. S. Stecura, Optimization of the NiCrAlY/ZrO_2–$Y2O_3$ thermal barrier system. NASA Report No. TM-86905. NASA, Cleveland, OH, 1985.

23. D. Zhu and R. A. Miller, Thermal conductivity and sintering behavior of advanced thermal barrier coatings, NASA Report No. TM—2002-211481, Glenn Research Center, Cleveland, Ohio, 2002.

24. R. Soltani, H. Samadi, E. Garcia and T. W. Coyle, Development of alternative thermal barrier coatings for diesel engines, SAE Technical Paper 2005-01-0650, 2005.

25. M. Gell, The potential for nanostructured materials gas turbine engine, Nanostructured Materials, 6, 1995, 997-1000.

26. M. Gell, Application opportunities for nanostructured materials and coating, Materials Science & Engineering, A204, 1995, 246-251.

27. R. S. Lima, A. Kucuk, and C. C. Berndt, Bimodal distribution of mechanical properties on plasma sprayed nanostructured partially stabilized zirconia, Material Science and Engineering A, 327 (2), 2002, 224-232.

28. R. S. Lima, A. Kucuk, and C. C. Berndt, Integrity of nanostructured partially stabilized zirconia after plasma spray processing, Material Science and Engineering A, 313(1-2), 2001, 75-82.

29. Y. Zeng, S. W. Lee, L. Gao, and C. X. Ding, Atmospheric plasma sprayed coatings of nanostructured zirconia, Journal of the European Ceramic Society, 22, 2002, 347-351.

30. H. Chen, and C. X. Ding, Nanostructured zirconia coating prepared by atmospheric plasma spraying, Surface and Coating Technology, 150, 2002, 31-36.

31. G. Soyez, J. A. Eastman, L. J. Thomson, G. R. Bai, P. M. Baldo, A. W. McCormick, R. J. DiMelfi, A. A. Elmustafa, M. F. Tambwe and D. S. Stone, Grain-size-dependent thermal conductivity of nanocrystalline yttria-stabilized zirconia films grown by metal-organic chemical vapor deposition, Applied Physics Letters, 77, 2000, 1155-1157.

32. L. Zhao, Y. Pei, Yong Liu, D. Berardan and N. Dragoe, InFeZnO4 as promising thermal barrier coatings, Journal of American Ceramic Society, 94(6), 2011, 1664-1666.

33. D. Stöver, G. Pracht, H. Lehmann, M. Dietrich, J. Döring, and R. Vaßen. New material concepts for the next generation of plasma-sprayed thermal barrier coatings, Journal of Thermal Spray Technology, 13(1), 2004, 76–83.

34. W. Ma, D. E. Mack, R. VaXen, and D. Sto¨ver, Perovskite-type strontium zirconate as a new material for thermal barrier coatings, Journal of American Ceramic Society, 91(8), 2008, 2630-2635.

35. X. Q. Cao, R. Vassen and D. Stoever, Ceramic materials for thermal barrier coatings, Journal of the European Ceramic Society 24, 2004, 1–10.

36. M. R. Winter, D. R. Clarke, Thermal conductivity of yttria-stabilized zirconia–hafnia solid solutions, Acta Materialia, 54, 2006, 5051–5059 .

37. G. Suresh, G. Seenivasan, M. V. Krishnaiah, and P. S. Murti, Investigation of the thermal conductivity of selected compounds of lanthanum, samarium and europium, Journal of Alloys and Compounds, 269, 1998, L9–L12.

38. H. Lehmann, D. Pitzer, G. Pracht, R. Vassen and D. Stover, Thermal conductivity and thermal expansion coefficients of the lanthanum rareearth-element zirconate system, Journal of the American Ceramic Society 86(8), 2003, 1338–1344.

39. R. Vaßen, F. Traeger and D. Stöver, New thermal barrier coatings based on pyrochlore/YSZ double-layer systems, International Journal of Applied Ceramic Technology, 2004, 1(4),351-361.

40. H. G. Wang, H.Herman, Thermomechanical properties of plasma-sprayed oxides in the MgO-Al2O3-SiO2 system, Surface Coating Technology, 42, 1990, 203-216.

41. J. Wang, H. P. Li and R. Stevens, Review: Hafnia and hafnia-toughened ceramic, Journal of Materials Science 27, 1992, 5397-5430.

42. J. H. Kim, M. C. Kim, C. G. Park, Evaluation of functionally graded thermal barrier coatings fabricated by detonation gun spray technique, Surface and Coatings Technology, 168, 2003, 275–280.

43. R. Ruh, H. J. Garrett, R. F. Domagala and N. M. Tallen, The svstern zirconia-hafnia, Journal of the American Ceramic Society, 51(1), 1968) 23-28.

44. Y. Sakka, Y. Oishi and Ken Ando, Zr-Hf inter-diffusion in polycrystalline Y203-(Zr + Hf)02, Journal of Materials Science, 17(11), 1982, 3101-3105 .

45. Carbon Dioxide Information Analysis Center, Accessed on 12-20-2012, http://cdiac.ornl.gov.

46. National Oceanic and Atmospheric Administration, Accessed on 10-20-2011, www.noaa.gov.

47. International Energy Outlook 2010 (IEOU) published by the Energy Information Administration (EIA) and the Department of Energy (DOE).

48. K. S. Murphy and N. Shores, Stabilized zirconia thermal barrier coating with hafnia, US patent 0118873 A1, 2003.

49. Sputter deposition, Wikipedia, Accessed on 09-17-2012.
http://en.wikipedia.org/wiki/Sputter_ deposition

50. Sputter deposition, Oxford Vacuum Science, Accessed on 12-20-2012.
http://www.oxford-vacuum.com/background/thin_film/sputtering.htm.

51. Technical Notes - Thin-Film Vacuum Deposition Sources, Kurt J. Lesker, Accessed on 12-15-2012. http://www.lesker.com/newweb/Deposition_Sources/TechNotes_Sputtering.cfm.

52. P. J. Kelly and R.D. Arnell, Magnetron sputtering: a review of recent developments and applications, Vacuum 56, 2000, 159-172.

53. Physical Vapor Deposition – Sputtering, ETA Film Technology Inc., Accessed on 09-17-2012. http://www.etafilm.com.tw/PVD_Sputtering_Deposition.html.

54. Sputtering technology, Angstrom Sciences, Accessed on 12-20-2012. http://www.angstromsciences.com/technology/ sputtering-technology/index.html.

55. Electron beam physical vapor deposition, Wikipedia, Accessed on 09-17-2012. http://en.wikipedia.org/wiki/Electron_beam_physical_vapor_deposition.

56. Fabrication techniques, Accessed on 09-17-2012. http://wwwold.ece.utep.edu/research/webedl/cdte/Fabrication/index.htm.

57. J. Singh and D. E. Wolfe, nanostructured component fabrication by electron beam-physical vapor deposition, Journal of Materials Engineering and Performance, 14 (4), 2005, 448-459.

58. B. D. Cullity, S.R. Stock, Elements of X-Ray Diffraction, 3rd Ed, Prentice-Hall Inc., 2001, USA.

59. D. G. Cahill, Analysis of heat flow in layered structures for time-domain thermoreflectance, Review of Scientific Instruments, 75(12), 2004, 5119-5122.

60. W. C. Oliver and G.M. Pharr, Measurement of hardness and elastic modulus by instrumented indentation: Advances in understanding and refinements to methodology, Journal of Materials Research, 19 (1), 2004, 3-20.

61. V. Teixeiraa, M. Andritschky, W. Fischer, H. P. Buchkremer and D. StoÈver, Analysis of residual stresses in thermal barrier coatings, Journal of Materials Processing Technology 92-93, 1999, 209-216.

62. C. H. Ma, J. H. Huang and H. Chen, Residual stress measurement in textured thin film by grazing-incidence X-ray diffraction, Thin Solid Films, 418, 2002, 73–78.

63. C. K. Lee, E. Cho, H. S. Lee, C. S. Hwang and S. Han, First-principles study on doping and phase stability of HfO2 Physical Review B, 78, 2008, 012102(1-4).

64. E. Rauwel, C. Dubourdieu, B. Holländer, N. Rocha, F. Ducroquet, M.D. Rossell, G. Van Tendeloo and B. Pelissier, Stabilization of the cubic phase of HfO_2 by Y addition in films grown by metal organic chemical vapor deposition, Applied Physics Letters. 89, 2006, 012902(1-3).

65. P. Duwez, F. H. Brown Jr. and F. Odell, The zirconia-yttria system, Journal of the Electrochemical Society, 98(9),1951, 356-362.

66. D. W. Stacy and D. R. Wilder, The yttria-hafnia system, Journal of American Ceramic Society, 58,1975, 285-288.

67. K.I. Portnoi, I.V. Romanovich and E. N. Timofeeva, Inorganic Material, 7, 1971, 783.

68. D. L. Wood, K. Nassau K, T. Y. Kometani and D. L. Nash, Optical properties of cubic hafnia stabilized with yttria, Applied Optics, 29(4), 1990, 604-607.

69. R. Terki, G. Bertrand, H. Aourag, C. Coddet, Cubic-to-tetragonal phase transition of HfO2 from computational study, Materials Letters 62, 2008, 1484–1486.

70. K. Matsumoto, Y. Itoh and Y. Ishiwata, Thermal conductivity and sintering behavior of hafnia-based thermal barrier coating using EB-PVD, Proceedings of International Gas Turbine Congress (IGTC), 2003, Tokyo, Japan, 131(1-6).

71. C. H. Lu, J. M. Raitano, S. Khalid, L. Zhang and S. W. Chan, Cubic phase stabilization in nanoparticles of hafnia-zirconia oxides: Particle-size and annealing environment effects, Journal of Apploed Physics, 103, 2008, 124303(1-7).

72. N. R. Kalidindi, F. S. Manciu and C. V. Ramana, Crystal structure, phase, and electrical conductivity of nanocrystalline W0.95Ti0.05O3 thin films, ACS Applied Materials & Interfaces, 3, 2011, 863–868.

73. V. H. Mudavakkat, M. Noor-A-Alam, K. Kamala Bharathi, S. AlFiafy, K. Dissanayeke, A. Kayani and C.V. Ramana, Structure and AC conductivity of nanocrystalline Yttrium oxide thin films, Thin Solid Films 519, 2011, 7947–7950.

74. A. Rosencwaig and A. Gersho, Theory of the photoacoustic effect with solids, Journal of Applied Physics, 47, 1976, 64–69.

75. C. D. Wirkus, M. F. Berard, Abradability and hardness in rare-earth-oxide stabilized hafnia, Journal of Materials Science 17, 1982 109-114.

76. D. J. Quinn, B. Wardle and S. M. Spearing, Residual stress and microstructure of as-deposited and annealed, sputtered yttria-stabilized zirconia thin films, Journal of Material Research, 23(3), 2008, 609-618. .

77. G. Moskal, L. Swadźba and T. Rzychoń, Measurement of residual stress in plasma-sprayed TBC with a gradient of porosity and chemical composition, Journal of Achievement in Materials and Manufacturing Engineering, 23 (2), 2007, 31-34.

78. S. Widjaja, A. M. Limarga and T. H. Yip, Modeling of residual stresses in a plasma-sprayed zirconia/alumina functionally graded-thermal barrier coating, Thin Solid Films, 434, 2003, 216–227.

79. J. Matejicek, S. Sampath and J. Dubsky, X-ray residual stress measurement in metallic and ceramic plasma sprayed coatings, Journal of Thermal Spray Technology, 7(4), 1998. 489-496 .

80. O. Kesler, J. Matejicek, S. Sampath, S. Suresh, T. Gnaeupel-Herold, P.C. Brand and H.J. Prask, Measurement of residual stress in plasma-sprayed metallic, ceramic and composite coatings, Materials Science and Engineering A257, 1998, 215–224.

81. J. Matejicek, S. sampath, P. C. Brand and H. J. Prask, Quenching, thermal and residual stress in plasma sprayed deposits: NiCrAlY and YSZ coatings, Acta Materialia, 47(2), 1999, 607-617.

Vita

Mohammed Noor-A-Alam completed his bachelor with the grade “First Class” from the Department of Chemical Engineering and Polymer Science at Shahjalal University of Science and Technology (SUST), Bangladesh. Then he joined as a Scientist in Bangladesh Atomic Energy Commission in 2000. He went to Hacettepe University in Turkey as a research fellow of International Atomic Energy Agency (IAEA) and worked with polymeric hydrogels for medical applications. Noor-A-Alam joined as faculty in the Department of Chemical Engineering and Polymer Science at SUST, in 2001. He achieved his masters in Advanced Materials from Chalmers University of Technology, Sweden in 2007. He worked with carbon nanotube reinforced polymer nano-composites for his master’s thesis. He accomplished his PhD (Energy Science & Engineering track) in the Department of mechanical Engineering at The University of Texas at El Paso, USA. His dissertation is focused on “Hafnia-based nanostructured thermal barrier coatings for next generation gas turbine technology”. Noor-A-Alam published 14 articles in scientific journals and presented his work in several national and international conferences. He was awarded several scholarships and awards including Cotton Graduate Scholarship by UTEP, Best Junior Researcher Awards by 2011 TMS Annual Conference, Dorothy M. and Earl S. Hoffman Travel Grant by 2010 AVS conference and Adlerbertska Hospitiefond Scholarship by Chalmers University of Technology. He worked as Research Associate (Oct. 2009 - Aug. 2012) in the Center for Space Exploration Technology Research (cSETR) at UTEP. Noor-A-Alam has been working as an Assistant Instructor in the Department of Mechanical Engineering at UTEP since September, 2012 and teaching the course “Energy System Engineering”.

Mohammed Noor-A-Alam
nooraalam11@gmail.com